Electron specific track fitters and J/ψ resonance studies in ATLAS

Susan Cheatham

BSc (Birmingham)

Particle Physics Group

Department of Physics

March 2010

A thesis submitted to Lancaster University for the degree of

Doctor of Philosophy in the Faculty of Science and Technology

Contents

List of Figures

List of Tables

Electron specific track fitters and J/ψ resonance studies in ATLAS

Susan Cheatham

A thesis submitted for the degree of Doctor of Philosophy, March 2010

Abstract

This thesis discusses the reconstruction of J/ψ to electron pairs based on fully simulated ATLAS Monte Carlo samples. A possible trigger strategy is described, taking advantage of the possible presence of a muon in the final state in $b\bar{b}$ production once one b-hadron decays into J/ψ +X, followed by J/ψ decay into e^+e^-. The tracks belonging to low-energy electrons are reconstructed using a dedicated algorithm, taking into account bremsstrahlung effects. The performance of this algorithm is compared with the other ATLAS track fitters and the potential of using this tracking algorithm to map the Inner Detector material is presented. The improvement in separation of indirect from prompt J/ψ, by separately considering two kinematical configurations, 'cowboys' and 'sailors', is also presented, along with a feasibility study of measuring the ratio of indirect to prompt J/ψ.

Declaration

This thesis is my own work and no portion of the work referred to in this thesis has been submitted in support of an application for another degree or qualification at this or any other institute of learning.

The Author

I was sponsored by Marconi Underwater Systems to study physics at Birmingham University. I graduated in 1990. After travelling for a year in Australia, New Zealand and China I worked for Price Waterhouse IT Consultancy, London, as an Analyst Programmer then FISONS Laboratory Management Systems, Manchester, as an IT Analyst. My love of the outdoors led me to work for Rayleigh International in Chile and World Challenge in Peru and Venezuela leading expeditions for young people. I qualified as a secondary school teacher of science and outdoor activities at Bangor University in 1996 and taught for 9 years. I first visited CERN on a trip for physics teachers with the aim to inspire my students with my greater understanding. However I was so inspired I applied to study for a PhD. I have since enjoyed a fantastic time with Lancaster University, two years of which were based at CERN.

Acknowledgments

Huge thanks go to my supervisor Vato Kartvelishvili, for his guidance and advice throughout my PhD as well as for his many anecdotes.

I would like to dedicate a few words to the whole Lancaster group. Firstly, for giving me the opportunity to study for a PhD, and then for the friendship and support I have received from everyone since. Particular thanks to Rob Henderson for his many 'napkin' explanations and to Eva Bouhova-Thacker for all her help and advice as well as introducing me to 'slabs of deer' in the Geneva restaurants. Thanks also to Alistair, Darren, James, James, Lee, Roger and Ruth.

I wish to thank Wolfgang Liebig for his assistance and patience as I struggled with ATLAS software. I also wish to thank Mauro Donega for his encouragement and chats over coffee.

There are a lot of people that I had the pleasure of meeting during the last few years. 4pm cake and coffee breaks were a particularly significant and memorable part of my time at CERN. So thanks to all the other students and postdocs with whom I shared time with, in particular Dave, Gareth, Johanna, Katharine, Tom, Tom and Uli.

The opportunity to work in such an incredible environment as CERN was a huge privilege. What also made my time at CERN unforgettable was the two clubs I joined whilst I was there. The CERN cycle club, particularly Peter, Sylvia and Henrik, for company on many scenic rides and icecream stops. The St Genis Club Alpin, for stunning ski randonnée trips and patient acceptance of my poor English ski technique.

Thanks to my mum, for all her unquestioning support. Last but not least, thanks to my friends at home in Cumbria, keeping me sane in the last few months of my PhD with some very wet cold mountain bike rides followed by a pint or two in the pub.

I am indebted to the Science and Technology Facilities Council for funding my research, my two-year attachment to CERN, and the various workshops and conferences I attended. Most importantly, this research would not have been possible without the entire ATLAS Collaboration, so thanks to all the engineers and physicists who have played a part in this incredible LHC machine.

Sue Cheatham, March 2010

To my dad.

1

Introduction

On 23rd November 2009, during the early commissioning of the CERN Large Hadron Collider (LHC), two counter-rotating proton bunches were circulated for the first time concurrently in the machine, at the LHC injection energy of 450 GeV per beam. Despite the proton intensity being very low, all LHC experiments reported a number of collision candidates, with great excitement.

On 30th November the LHC became the world's highest energy particle accelerator, having accelerated its twin beams of protons to a collision energy of 2.36 TeV in the early hours of the morning. This exceeded the previous world record of 1.96 TeV, which had been held by the US

Fermi National Accelerator Laboratory's Tevatron collider since 2001. First physics at the LHC is scheduled for the first quarter of 2010, at a collision energy of 7 TeV (3.5 TeV per beam).

ATLAS is one of two general purpose detectors at the LHC in Geneva, Switzerland. The inner part of the detector consists of a tracking system for the measurement of the trajectories of charged particles. The tracking system is structured in layers which measure where the particle trajectories intersect those layers. The physics analyses however are mainly interested in the momentum and direction of the particle at its estimated creation. Determination of particle four-momentum is part of track reconstruction.

The reconstruction of electrons is more problematic than the reconstruction of other charged tracks, since in addition to ionisation energy loss and multiple Coulomb scattering, electrons suffer from large energy losses due to bremsstrahlung. The fraction of energy lost to bremsstrahlung depends on the type and amount of material traversed by the electron. There is a sizable probability for an electron to lose a significant fraction of its energy in the ATLAS inner detector. Although much of the bremsstrahlung radiation will be collected by the electromagnetic calorimeter, the track in the Inner Detector can be seriously affected, resulting in a poorly reconstructed momentum or even in a failure to reconstruct the track altogether. Bremsstrahlung recovery is therefore extremely important in order to achieve the full range of physics goals in ATLAS. Higgs decays $H \to ZZ \to e^+e^-e^+e^-$ and SUSY searches in multi-leptonic states are examples of processes to benefit.

Even at low luminosity ATLAS will quickly start improving on current quarkonia measurements providing world leading results with around 10 pb^{-1} of data. The narrow quarkonia resonances will also be used as tools for alignment and calibration of the trigger and tracking systems. CDF and *DØ* extensively and successfully used quarkonia mass shifts to disentangle various detector effects, but it took many years at the Tevatron to collect sufficient statistics across a range of variables to allow for proper correction and alignment leading to a detailed understanding of various detector effects.

This thesis is concerned with early data studies, focusing on electron tracking and the J/ψ (ee) resonance. I did not carry out one big analysis, but rather a number of smaller studies, relevant to the tracking and performance community. I start in Chapter **??** with a brief overview of the Standard Model, followed by an introduction to the J/ψ particle. Then Chapter **??** gives an introduction to the LHC and a description of the ATLAS experiment explaining the different detector sub-systems, in particular the Inner Detector. The ATLAS detector's ability to reconstruct tracks with high precision is critical both for the calibration of the detector and for the analysis of physics processes. Particles traverse different layers and materials designed to detect them. In Chapter **??** the key factors involved in the passage of particles through matter are described. High energy electrons traversing matter lose energy predominantly by bremsstrahlung. We have developed a fast and efficient method of bremsstrahlung recovery called Dynamic Noise Adjustment (DNA). Chapter **??** introduces the different track fitters implemented in the Inner Detector software. Chapter **??** compares the performance of the different ATLAS track fitters, focusing on electron reconstruction. Mapping the material in ATLAS will be one of the major tasks at the beginning of data taking. The ultimate electron reconstruction performance will only be reached when the material budget in the Inner Detector is well understood. Chapter **??** considers DNA as a potential tool for mapping the material of the Inner Detector. Bremsstrahlung-aware tracking is important for J/ψ reconstruction in e^+e^- mode, which is interesting for both detector studies and physics. Chapter **??** suggests that it is important to consider the kinematics of electron tracks and shows that the separation of prompt from indirect J/ψ is improved by separate consideration of two kinematical configurations, 'cowboys' and 'sailors'. A feasibility study of the measurement of the ratio of indirect to prompt J/ψ is also presented.

1.1 LHC start-up – 10 September 2008

There was huge media coverage leading up to the so-called ‘Big Bang’ day. Journalists from around the world were invited to CERN and into the control rooms to witness first-hand the pressure and excitement on the day. The LHC start-up took place under the full glare of publicity.

Safety concerns regarding the LHC collisions attracted widespread media attention and many newspapers reported doomsday fears. CERN faced a lawsuit filed in Hawaii seeking a court order that would force the US government to intervene and delay the start up of the collider. The legal challenge claimed the LHC might destroy the planet by creating a black hole or a clump of matter known as a strangelet.

Despite all concerns, the first – clockwise – beam completed its first circuit just before 0930 (British Summer Time, BST). Figure **??** illustrates first circulating beam; a yellow spot represents a bunch of a few particles, the two spots show that the bunch has completed a full circuit.

Collimators are installed around the LHC ring to absorb ‘stray’ particles that have spread out, forming a halo around the beam. It is important to absorb this halo to protect the rest of the machine from damage, in particular the superconducting magnets, where any slight heating by such stray particles could cause a magnet quench. A quench is an abnormal termination of magnet operation that occurs when part of the superconducting coil enters the normal (resistive) state.

Figure **??** a) shows the first single beam event in ATLAS. For so-called ‘beam splash’ events the beam in one arm of the LHC was dumped onto closed collimators located 140 m upstream and downstream of ATLAS. The collision leads to a large number of detectable secondary particles longitudinally traversing the detector. Figure **??** b) shows ATLAS event display with various sub-detector specific views. To avoid damaging the Inner Detector, ATLAS was run with pixel and silicon-strip tracking detectors (SCT) barrel off and SCT endcaps, forward calorimeters and forward muon chambers at reduced voltage.

The second – anti-clockwise – beam successfully circled the ring after 1400 (BST). To get

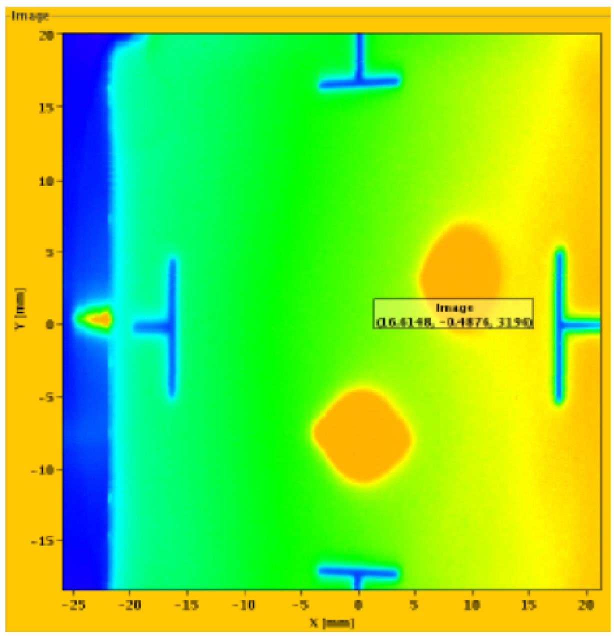

Figure 1.1: *First ciculating beam in ATLAS. 10 September 2008 [**?**]. A yellow spot represents a bunch of a few particles, the two spots show that the bunch has completed a full circuit.*

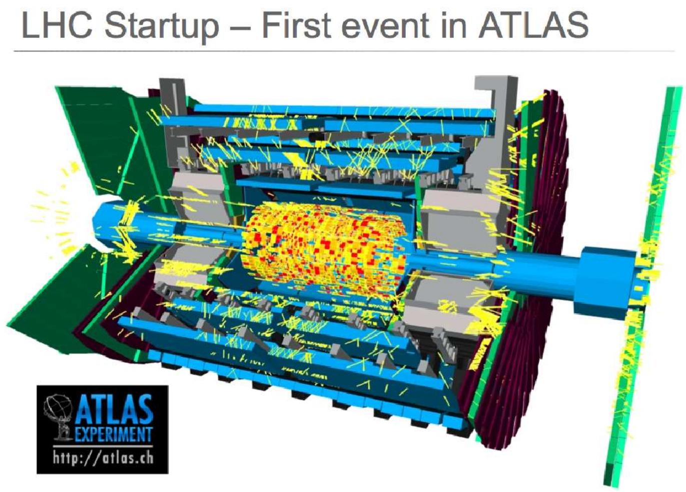

(a) First beam splash event in ATLAS.

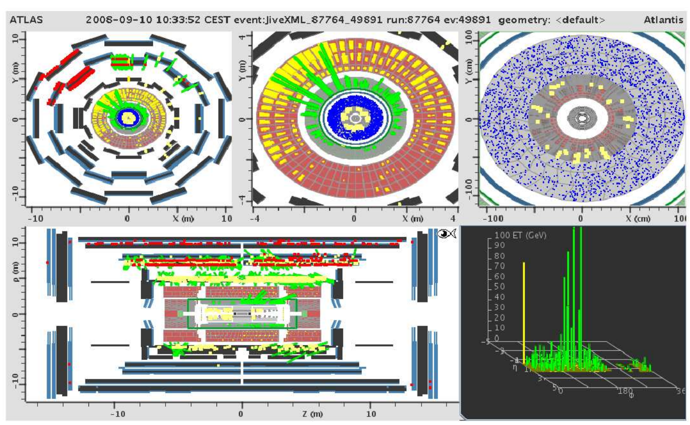

(b) ATLAS event display with various sub-detector specific views.

Figure 1.2: *First single beam event seen by the ATLAS experiment, on 10th September 2008. To avoid risks, LHC decided to open the collimators progressively. Proton collisions with the collimators leads to a large number of secondary particles visible in the sub-detectors [**?**].*

beams around the ring in both directions on the first day exceeded all expectations.

Unfortunately just nine days later an incident occurred. A resistive zone developed in the electrical bus in the region between two super-conducting magnets. An electrical arc developed and punctured the helium enclosure. Helium was then released into the insulation vacuum of the cryostat. Spring-loaded relief valves on the vacuum enclosure opened, relieving the helium into the tunnel but the system was not designed for such high pressure. A shutdown period followed for repair and improvement.

1.2 LHC restart – November 2009

The re-start was a low-key affair, with the media not invited, in contrast to the razzmatazz of the original start-up.

ATLAS was the first detector to have the opportunity to observe collisions. The first 900 GeV candidate collision was observed at 14:22 November 23, 2009, and is shown in Figure **??**.

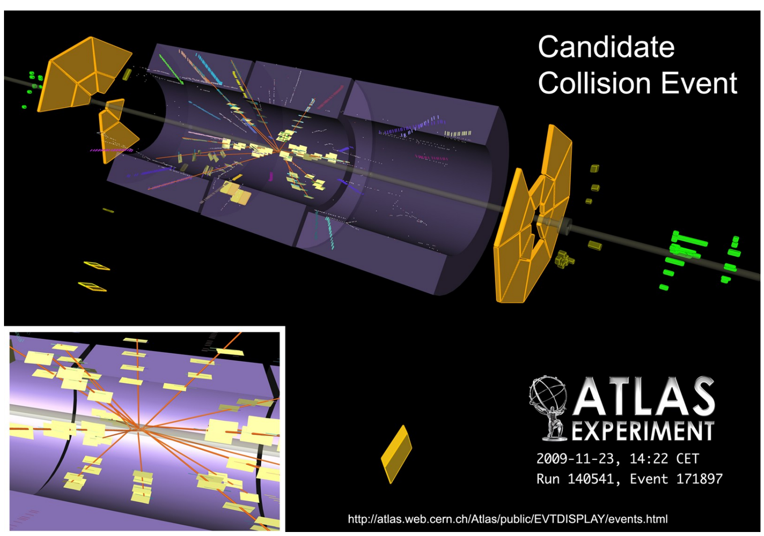

Figure 1.3: *First candidate collision in ATLAS: November 23 2009 [**?**].*

On December 6th the LHC achieved for the first time 900 GeV collisions under stable beam conditions. This allowed ATLAS to fully ramp the high voltage of the inner most pixel and SCT detectors. Two days later the LHC achieved for the first time 2.36 TeV collisions and ATLAS recorded their first events at this record energy.

Stable beams have circulated reliably, a world record collision energy has been set and substantial quantities of data ($\sim 9\mu\text{b}^{-1}$) have been collected. 2009 has been a fantastic year for ATLAS and the LHC and heralds the start of a new era of high energy particle physics.

Unfortunately, all this happened a few months after the end of my studentship and hence no studies in this thesis are based on real data.

'I was born not knowing and have had only a little time to change that here and there'

Richard Feynman

2 Theory

This chapter starts with a brief overview of the Standard Model, followed by an introduction to the J/ψ particle.

One could say that elementary particle physics was born in 1897, with J.J. Thomson's discovery of the electron. Thomson correctly surmised that these electrons were essential constituents of atoms. Rutherford's famous scattering experiment demonstrated that the positive charge and most of the mass of the atom was concentrated in the central nucleus.

Since then, physicists have discovered that nuclei consist of 'smaller' particles: protons and neutrons and then that these consist of even smaller particles: quarks and gluons. Currently there is no evidence that these consist of yet smaller particles and therefore they are called ‘elementary’.

Quarks, gluons and electrons are by far the most common type of particle in ordinary matter, but they are certainly not the only ones that exist. For example, the electron (e) has two partners that have similar properties: the muon (μ) and the tau (τ). Each of these has a corresponding neutrino particle: the electron neutrino (ν_e), the muon neutrino (ν_μ) and the tau neutrino (ν_τ). Neutrinos are produced abundantly in the Sun, together with photons that are responsible for the light that we see.

The atoms that constitute the world around us, in ordinary matter, are made up of just two types or flavours of quarks: the up (u) and down (d) quarks. There are however six flavours, with the frivolous names of charm (c), strange (s), top (t) and bottom (b). The heaviest quark, the top quark, is 175 times heavier than a proton and as such it took until 1995 before particle accelerators had enough energy to produce and discover it.

The quarks and leptons are grouped into generations, as shown in Table **??**. The generations are replicas apart from the fact that the mass is very different from one generation to the next.

$$
\begin{array}{lcccc}
 & & \text{GENERATION} & & \text{CHARGE} \\
 & \text{I} & \text{II} & \text{III} & \\
\text{QUARKS} & \begin{pmatrix} u \\ d \end{pmatrix} & \begin{pmatrix} c \\ s \end{pmatrix} & \begin{pmatrix} t \\ b \end{pmatrix} & \begin{matrix} +\frac{2}{3} \\ -\frac{1}{3} \end{matrix} \\
\text{LEPTONS} & \begin{pmatrix} \nu_e \\ e^- \end{pmatrix} & \begin{pmatrix} \nu_\mu \\ \mu^- \end{pmatrix} & \begin{pmatrix} \nu_\tau \\ \tau^- \end{pmatrix} & \begin{matrix} 0 \\ -1 \end{matrix}
\end{array}
$$

Table 2.1: *Elementary particles as described in the Standard Model of particle physics. Quarks and leptons are known as elementary fermions.*

The world of everyday life is governed by classical mechanics. For objects that travel very fast (comparable to the speed of light), the classical rules are modified by special relativity. For objects that are very small (comparable to the size of atoms), quantum mechanics supersedes classical mechanics. Elementary particles are both small and fast and so require a theory that incorporates both quantum mechanics and relativity: quantum field theory.

In quantum field theory quarks and leptons are described by spinors. Spin $\frac{1}{2}$ $\hbar$ spinors can be used to represent the leptons $l = e, \nu_e, \mu, \nu_\mu, \tau, \nu_\tau$ and quarks $q = d, u, s, c, b, t$, collectively known as fermions. The mediators of the interactions are described by spin 1 $\hbar$ particles and are called gauge bosons.

As far as we know, there are just four fundamental forces in nature:

- Strong: The strong force holds the protons and neutrons together in the nucleus and indeed holds together the quarks in those protons and neutrons. The mediator is the gluon.

- Electromagnetic: The force between charged particles is mediated by the massless photon, γ, and hence has infinite range.

- Weak: This interaction is responsible for some radioactive decays, and for nuclear fusion in the sun. It is mediated by the $W^{\pm}$ and Z bosons. These particles have very large masses, nearly 100 GeV, which severely limits the strength and range of the interaction. Hence the name 'weak'.

- Gravitational: Most people assume that gravity is simply too weak to play a significant role in elementary particle physics at the current level of energies.

In the 1960's and 1970's some bits and pieces of a theory started to emerge, describing elementary particle interactions. The resulting theory is called the Standard Model and is extremely successful [**?**], [**?**] and references therein. The Standard Model encompasses the electromagnetic force, described by Quantum Electro Dynamics (QED), the weak force and the strong nuclear force, described by Quantum Chromo Dynamics (QCD).

The theory of QCD describes the interactions between quarks and gluons. Two characteristic properties of this theory, on the two extremes of the energy range, are ‘confinement’ and ‘asymptotic freedom’. Confinement implies that quarks and gluons cannot be observed in isolation. It would require an infinite amount of energy to pull them apart. Asymptotic freedom is the property that causes interactions between particles to become weaker at shorter distances such that quarks within nucleons can move as free non-interacting particles.

The electromagnetic and weak interactions were unified in a single electroweak theory by Glashow, Weinberg and Salam [**?**]. The photon is massless while the $W^{\pm}$ and Z particles are massive, a breaking of the electro-weak symmetry. The Standard Model postulates the existence of another boson, the Higgs boson, which describes the mechanism of symmetry breaking and interacts with the quarks and leptons such that they acquire mass.

Quarks and leptons all have their own antiparticles. Antiparticles have the same mass but opposite quantum numbers e.g. charge. Lepton interactions are characterised by the conservation of lepton number, where each particle is assigned +1 and antiparticle -1. Weak interactions between quarks from different generations are common. The weak decay of a quark to another quark of a different flavour is governed by a 3x3 mixing matrix named the CKM matrix [**?**], after Cabbibo, Kobayashi and Maskawa [1)].

In QCD the equivalent of electric charge is called colour. Red, blue and green are used to define three possible states. Colour interactions are mediated by gluons. QCD requires eight gluons of the possible nine colour-anticolour combinations (the ninth combination is colourless). All free particles observed in nature at high distances are colourless. The Standard Model predicts that unbound quarks will combine with other unbound quarks to form hadrons: baryons and mesons.

[1)] In 2008, Kobayashi and Maskawa shared one half of the Nobel prize in Physics ‘for the discovery of the origin of the broken symmetry which predicts the existence of at least three families of quarks in nature’[**?**].

Baryons consist of three valence quarks and mesons consist of a quark-antiquark pair. Quarks and gluons cannot exist as free particles in nature, only in colour-neutral bound states.

2.1 The Standard Model

The Standard Model is based on the gauge symmetry group

$$SU(3)_C \otimes SU(2)_L \otimes U(1)_Y$$

which represents the current model of strong and electroweak interactions, where C is the colour charge, L refers to the left handed coupling of the weak isospin doublets, and Y is the weak hypercharge.

QED is an abelian gauge invariant theory based on the $U(1)_Q$ symmetry group, which describes the interaction between electrically charged fermions and the photon. QED is motivated by symmetry principles linked to the conservation of electric charge.

The weak interaction affects all left-handed leptons and quarks. The weak interaction is the only interaction capable of changing flavour. It is also the only interaction which violates parity [2)]. The gauge group of the weak force is $SU(2)$ with 3 generators, matching the 3 gauge bosons, $W^{\pm}$ and Z^0.

The electromagnetic and weak forces are unified into a single gauge field theory, known as electroweak theory. The simplest group structure that allows for a parity-violating weak force and a parity-conserving electromagnetic force is $SU(2)_L \otimes U(1)_Y$. Weak isospin is the gauge symmetry of the weak interaction which connects quark and lepton doublets of left-handed particles in all generations; for example, up and down quarks, top and bottom quarks, electrons and electron

[2)] Parity symmetry leads to the prediction that the mirror image of a reaction occurs at the same rate as the original reaction. In 1956 a group led by Chien-Shiung Wu demonstrated conclusively, studying beta decay of Cobalt-60 nuclei, that weak interactions violate the P symmetry [**?**].

neutrinos. Weak hypercharge, Y, is a conserved quantum number relating the electrical charge and the third component of weak isospin[3)]. The gauge invariance of the electroweak symmetry group is broken locally; we observe in nature that the photon is massless whereas the W and Z gauge bosons are massive.

QCD is based on the $SU(3)_C$ gauge group, which describes the strong interactions of coloured quarks and gluons. Its structure is similar to that of QED except that the gauge group is non-Abelian (3x3 matrices do not commute, whereas numbers do). Since the gluons themselves carry colour (unlike the photon, which is electrically neutral) they couple directly to other gluons, leading to more complex and richer theories.

The Standard Model is described by a Lagrangian which has terms for each individual particle type that describes its kinematics and interactions. We require the Lagrangian to have both a global symmetry such that the Lagrangian remains invariant under the same gauge transformations at every space-time point, and a local symmetry allowing different transformation parameters at different space-time points. Noether's Theorem [**?**] states that every continuous symmetry of nature yields a conservation law, or conversely, every conserved quantity reflects an underlying symmetry. For example, the invariance of electrodynamics under gauge transformations leads to conservation of charge.

The idea that all forces in the Standard Model combine into one force is compelling, a single unified field theory. The strong coupling constant α_s decreases at short distances (very high-energy collisions), a feature of asymptotic freedom. So too does the weak coupling constant α_w, but at a slower rate. Meanwhile the electromagnetic coupling constant, α_e, which is the smallest of the three, increases. The value of the 'Grand Unification' scale where the three couplings are unified to one is not known. Different models make different predictions.

There exists another unification scheme, Supersymmetry. Bosons, the spin-1 force carrying

---

[3)] $Y = 2(Q - T_Z)$, where Q is charge and T_Z the third component of weak isospin.

particles, and fermions, the spin-$\frac{1}{2}$ matter particles, obey different statistics. While the Pauli exclusion principle prevents two fermions from inhabiting the same state, there is no such limitation for bosons. Supersymmetry proposes that a symmetry exists between bosons and fermions; for each fermion there is a boson with the same properties, and visa versa. The partners of the known particles are called superpartners. Supersymmetry doubles the number of particles, at least. Even the minimal supersymmetric Standard Model (MSSM) has about 120 parameters mostly connected to the breaking of supersymmetry. Supersymmetry must be broken spontaneously to give superparticles TeV scale masses. In several models the lightest supersymmetric particle is stable and a good candidate for dark matter which is suggested by cosmological studies.

The ultimate step for quantum field theory is a unified theory, explaining all interactions for all particles. Some believe that the string theory can be a good candidate. The basic idea is that the fundamental objects in the universe are not point-like elementary particles, but instead objects spread out in one dimension called strings. Excitation of the string gives the different particles we see in the universe.

The Standard Model does not tell us how to calculate the quark and lepton masses. They are simply empirical numbers taken from experiment. Indeed there are 19 parameters that have to be measured and then fed into the theory. The Standard Model is clearly not a complete description or the 'final' theory. There are several theories beyond the Standard Model such as SUSY and string theory, as mentioned earlier. The LHC experiments will be able to give hints as to which theories and models need further attention and they may exclude others.

2.2 J/ψ particle

The J/ψ was discovered in late 1974 by two groups: at Brookhaven, under C.C. Ting [**?**] and at Stanford by Burton Richter's group [**?**] (see Figure **??**). The two teams published simultaneously and the events that ensued came to be known as the November Revolution [4].

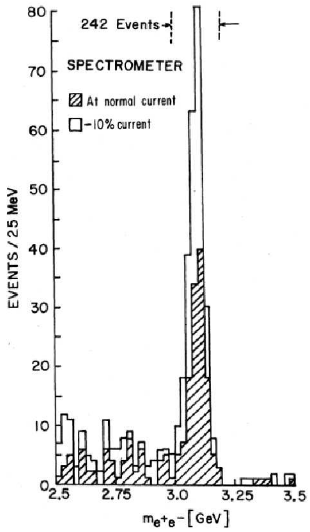

(a) The J discovery in e^+e^- final state at Brookhaven National Laboratory, USA. [?]

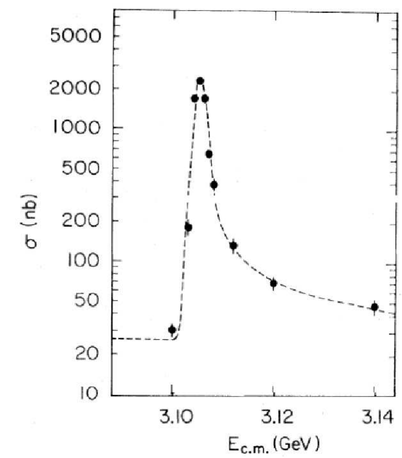

(b) The ψ discovery in multi-hadron final states at Stanford Linear Accelerator, USA. [?]

Figure 2.1: *The discovery of the J/ψ.*

The J/ψ was an extremely heavy meson for its time. What made the particle so unusual was its long lifetime, $\sim 10^{-20}$s, around 1000 times longer than any comparable particle. In the months that followed its discovery, the J/ψ was found to be a bound state of charm quark (a new quark at the time) and its antiquark. Indeed the discovery of the J/ψ implied the existence of all kinds of baryons and mesons, carrying various amounts of charm. The J/ψ itself has hidden charm (if the c is assigned a charm of +1 then the $\bar{c}$ will have a charm of -1) but with the discoveries of the charmed baryons Λ_c^+ and Σ_c^+, charmed mesons D^0 and D^+ and then the charmed strange meson D_s^+, the charm hypothesis was validated and, more importantly, the quark model was confirmed.

The narrow J/ψ resonance at 3.1 GeV was intriguing. It could decay hadronically, but with competitive leptonic modes. Okubo, Zweig, and Iizuka [?] suggested that final states only reached

[4] Ting and Richter shared the Nobel prize in 1976 for their discoveries.

through c quark-antiquark annihilation are suppressed (in other words gluon emission from heavy quarks is suppressed). This 'OZI rule' can be visualised such that if a Feynman diagram can be split by cutting only internal gluon lines the process will be suppressed. In Figure **??** we see that the three-pion diagram can be cut in two by cutting only gluon lines. The OZI rule is related to asymptotic freedom such that in an OZI-suppressed situation the gluons must be highly virtual, since they carry the energy necessary to make the hadrons into which they fragment. But asymptotic freedom says that gluons couple weakly at high momentum transfer (short ranges). In OZI-allowed processes the gluons are typically soft (low energy) and the coupling strong.

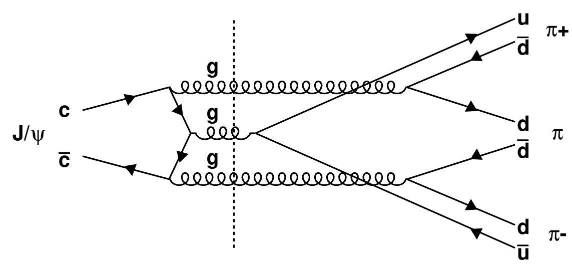

Figure 2.2: *The strong decay mode of the J/ψ is suppressed leading to its characteristic long lifetime. The OZI rule can be visualised such that if the Feynman diagram can be cut in two by slicing only gluon lines (and not cutting any external lines), the process is suppressed.*

The heavy quark pair will annihilate into the smallest number of gluons permissible. A decay via a single gluon is disallowed due to colour conservation. Two gluons are not allowed as this decay would violate C-parity. This means that the lowest order strong decay that can occur is via three gluon decay (which subsequently decay into light quark pairs).

The decay of $J/\psi \rightarrow D^+ + D^-$ or ($J/\psi \rightarrow D^0 + \overline{D}^0$) is kinematically forbidden, since the mass of a pair of D mesons is greater than that of the J/ψ . $J/\psi \rightarrow 3\pi$ is OZI-suppressed, as discussed above. This combination leads to the long 'charmed' life of the J/ψ .

So the hadronic decay modes of the J/ψ are strongly suppressed leading to a narrow decay width. This strong suppression of hadronic decays also means that electromagnetic decays begin to compete. Thus the J/ψ has a significant branching fraction to leptons (see Table **??**).

Mode	Fraction
$J/\psi \rightarrow$ hadrons	$87.7 \pm 0.5\%$
$J/\psi \rightarrow e^+e^-$	$5.94 \pm 0.06\%$
$J/\psi \rightarrow \mu^+\mu^-$	$5.93 \pm 0.06\%$

Table 2.2: *J/ψ decay modes and their fractions [**?**].*

2.2.1 Prompt J/ψ production

At the LHC J/ψ particles are produced by interactions between the partons (quarks and gluons) inside the colliding protons. J/ψ can be 'promptly' produced directly from parton interactions or from the feed-down decay of excited charmonium states ($\chi_c \rightarrow J/\psi\gamma$).

The predicted cross-section for 10 TeV prompt $J/\psi \rightarrow e^+e^-$ production, with electrons of p_T of at least 3 GeV, is 90 nb. At the design luminosity of the LHC this corresponds to about 1000 events per second.

About 30 to 40% of J/ψ are expected to come from decays $\chi_c \rightarrow J/\psi\gamma$. The energies of these emitted photons tend to be quite low due to the small mass splitting between the J/ψ and χ_c states, reducing the available energy in the decay.

J/ψ from χ_c decays will be considered as prompt J/ψ in this thesis.

2.2.2 Indirect J/ψ production

J/ψ may also be produced 'indirectly' via the decay of B-hadrons (formed through the hadronisation of b (or $\overline{b}$) quarks) and are a good signature for the identification and study of various B-Physics processes. A J/ψ is produced from the decay of a B-hadron approximately 1.2% of the time. B-hadrons are characterised by their relatively long lifetimes. Precise tracking permits the decay vertex of these particles to be measured as separate from the primary vertex of the proton-proton collision and thus provides a feature by which indirect J/ψ decays can be distinguished from prompt decays.

$J/\psi \rightarrow \mu\mu$ is by far the cleanest way of triggering and detecting J/ψ. However, my thesis is concentrating on electrons and hence the decay $J/\psi \rightarrow e^+e^-$

One possible source of indirect J/ψ is from B-meson decay as shown in Figure **??**. On the opposite side to the J/ψ, two virtual W bosons are produced, which can then decay leptonically. The muons from such decays can be used to trigger and thus capture the $J/\psi(ee)$ decay event. Using muons enhances the purity of the triggered events, compared with triggering on two electron candidates which is likely to have a huge background.

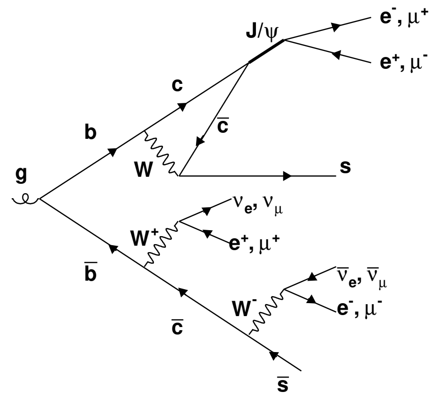

Figure 2.3: *One possible source of indirect J/ψ. The proposed trigger strategy takes advantage of the possible presence of a muon in the final state in $b\overline{b}$ production followed by the decay of one b-quark to J/ψ + X.*

The 'first' of these two W's (in Figure **??**) comes from b decay and is equally likely to decay into quark pairs (ud) or (cs) as into lepton pairs $(e\nu_e), (\mu\nu_\mu), (\tau\nu_\tau)$. With colour considerations there are six channels for quark decay, plus the three channels for leptonic decay. Each channel is roughly equally likely and therefore has a decay fraction $\sim 11\%$. The ‘second’ W boson comes from c decay and is likely to have five possible channels open: (ud) quark pair (three channels due to colour) and the two lighter leptonic channels. Each channel therefore has $\sim 20\%$ probablity. Despite the muon from this process having a higher probability of being produced than from the former W, it has lower momentum on average and so is less likely to trigger the event.

'Expect nothing, live frugally on surprise.'

Alice Walker

3

LHC and the ATLAS detector

The Large Hadron Collider (LHC) is a proton-proton collider designed to operate with a centre of mass energy up to 14 TeV. ATLAS is one of four detectors designed to observe the proton-proton collisions. This chapter gives a brief introduction to the LHC followed by a description of the ATLAS experiment explaining the different detector systems, in particular the Inner Detector. I also describe the magnet system, calorimetry, the trigger system and software tools.

3.1 Large Hadron Collider

The Large Hadron Collider (LHC) is a proton-proton synchrotron collider of 27 km circumference that has recently begun operation at CERN, the European Organisation for Nuclear Research, Geneva. The main LHC ring is fed with a proton beam from a chain of accelerators, beginning with production in a 50 MeV linear accelerator, followed by the 1.4 GeV Proton Synchrotron booster and the 26 GeV Proton Synchrotron, which delivers bunches of 10^{11} protons with 25 ns spacing to the Super Proton Synchrotron where the beams are accelerated to 450 GeV. The proton beams are then finally injected into the LHC for acceleration, focusing and eventually collision.

The LHC is designed to collide 7 TeV protons together with a centre of mass energy of 14 TeV and a design luminosity of 10^{34} cm^{-2}s^{-1}. The maximum achievable beam energy is determined by the strength of the magnetic field in the bending magnets and the requirement that the collider has to fit in the existing tunnel. A high luminosity is needed since many interesting processes, even at the LHC energy, have very small cross-sections of the order of 1 pb or less (1 pb=10^{-36}cm^2). At full luminosity there will be approximately 22 proton-proton collisions per bunch crossing, leaving the experiments to disentangle the effect of multiple proton interactions (pile-up) of the 'hard' interaction processes. Scattering processes at high-energy hadron colliders can be classified as either 'hard' or 'soft'. Quantum Chromodynamics (QCD) is the underlying theory for all such processes. Hard processes involve the quarks and gluons e.g. Higgs boson production, the rates and event properties can be predicted with good precision using perturbation theory. For soft processes, such as the underlying event, the rates and properties are dominated by non-perturbative QCD effects, which are less well understood.

The LHC can also collide beams of heavy ions, in particular lead nuclei, at 5.5 TeV per nucleon pair at a design luminosity of 10^{27} cm^{-2} s^{-1}.

The four main experiments consist of two general purpose detectors ATLAS (A Toroidal LHC ApparatuS) and CMS (Compact Muon Solenoid), a dedicated B-Physics experiment LHCb and a heavy ion experiment ALICE (A Large Ion Collider Experiment). See Figure **??**.

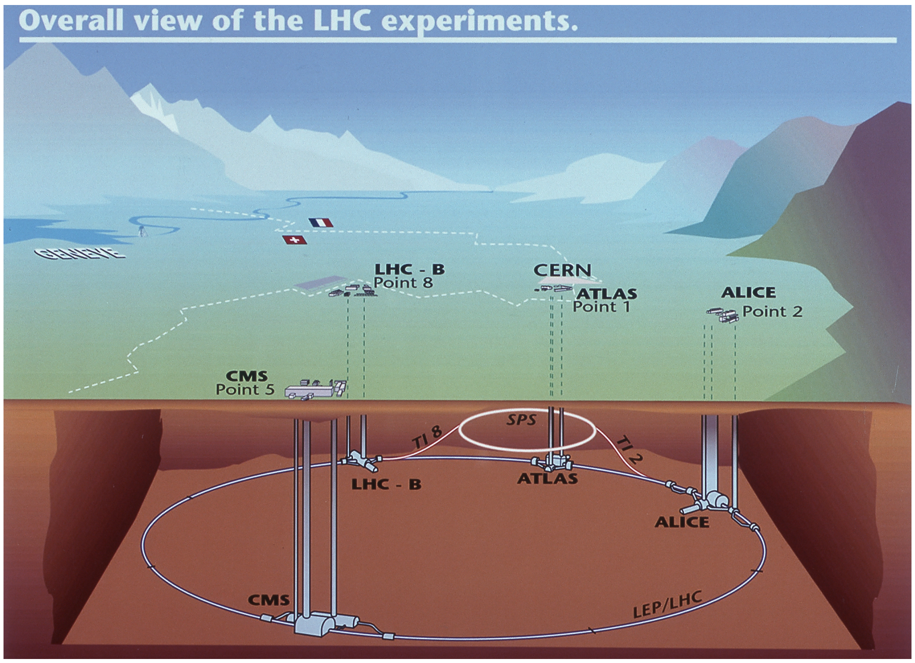

Figure 3.1: *This diagram shows the locations of the four main experiments (ATLAS, CMS, LHCb and ALICE) that will take place at the LHC. Located between 50 m and 150 m underground, huge caverns have been excavated to house the giant detectors. The SPS, the final link in the pre-acceleration chain, and its connection tunnels to the LHC are also shown. From [**?**].*

The LHC will extend the frontiers of particle physics with its unprecedented high energy and luminosity. It will provide a rich physics potential, ranging from more precise measurements of Standard Model parameters to the search for new physics phenomena.

3.2 ATLAS

3.2.1 ATLAS General Overview

The ATLAS detector [?] is designed to study a broad range of physics processes and has been optimised to achieve a number of physics goals, such as:

- Study of electroweak symmetry breaking i.e. discovery of the Higgs boson. The Standard model requires a scalar Higgs boson. The mass is not predicted, so it has to be measured. This requires high resolution electron, muon and gamma detection and excellent vertex resolution for detecting tau lepton and b quark decays.

- Searches for SUSY. The main signature of many SUSY channels is missing transverse energy, so hermeticity is required. Some other signatures include multi-leptonic final states.

- Precision measurements of W and top mass. This needs good knowledge of absolute energy scale of calorimeters.

- New heavy bosons and compositeness. Compositeness will produce high p_T jets, so good hadron calorimetry is needed. The heavy bosons will decay into high p_T leptons, so large bending power is required for charge determination.

- CP violation and B-decays. This requires excellent secondary vertex detection and full reconstruction of final state particles at low transverse momentum.

The ATLAS detector, shown in Figure **??**, consists of four major components: the Inner Detector which measures the momentum of each charged particle, the Calorimeter which measures the energies carried by the particles, the Muon Spectrometer which identifies and measures the muons and the Magnet System that bends the charged particles for momentum measurement. The detector is a cylinder with a total length of 42 m and a radius of 11 m and weighs approximately 7000 tonnes.

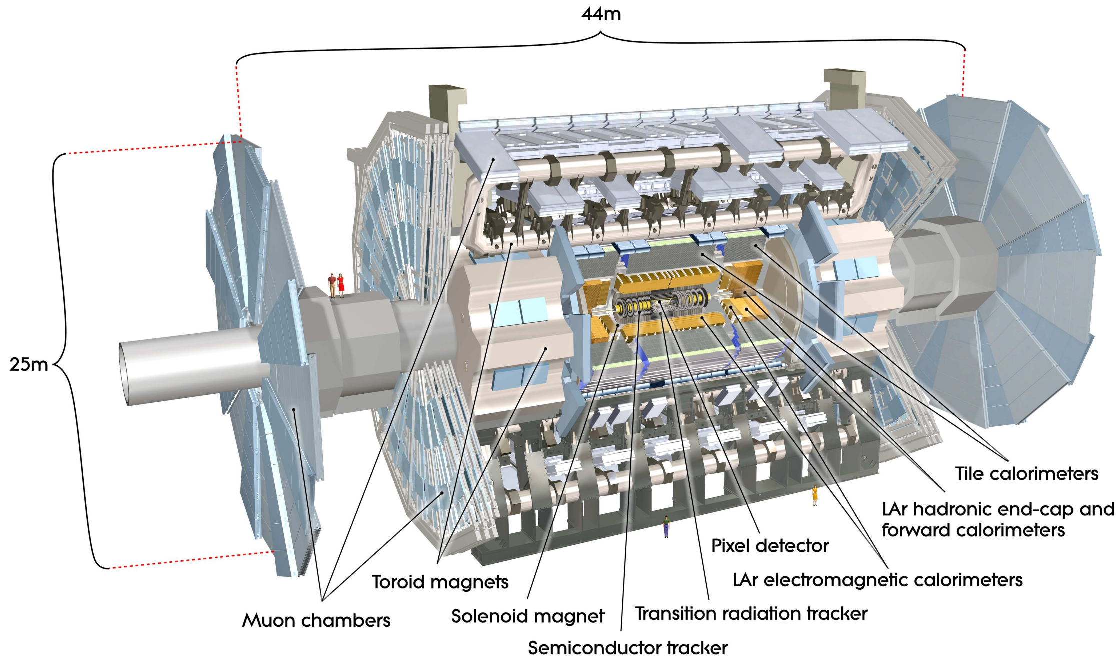

Figure 3.2: *Overall layout of ATLAS Detector (from [**?**]).*

The ATLAS Coordinate System is a right-handed system with the x-axis pointing to the centre of the LHC ring, the z-axis following the beam direction and the y-axis going upwards. The two ends of ATLAS are called the 'A-side' and the 'C-side' ('B' is the central barrel). The 'A'-side is along the positive z-axis and is in the direction of the airport and the Saleve mountain. ATLAS units are defined such that lengths are measured in mm and energies in MeV. Transverse momentum p_T is defined as the momentum perpendicular to the LHC beam axis.

The azimuthal angle, ϕ, which is measured around the beam axis, combined with the pseudo-rapidity,

$$\eta = -\log\ \tan\frac{\theta}{2}$$

(where θ is the angle from the beam pipe, the polar angle) are used to define a position within the detector. The distance ΔR in pseudorapidity azimuthal angle space is given by:

$$\Delta R = \sqrt{\Delta\eta^2 + \Delta\phi^2}$$

The high interaction rate at the LHC creates an enormous challenge for trigger and data acquisition. The trigger system will select about 100 interesting events out of 10^9 taking place every second. Three levels of trigger will reduce the data flow to $\sim$100 Mbytes per second. Huge computing resources will be required to store, reconstruct and analyse the data recorded.

The main design criteria of the ATLAS detector are

- Very good electromagnetic calorimetry for electron and photon identification and measurement, complemented by full-coverage hadronic calorimetry for accurate jet and missing transverse energy measurements.
- High precision muon momentum measurements, with the capability of providing accurate measurements at high luminosity using the external muon spectrometer alone.
- Efficient tracking at high luminosity for momentum measurement of high p_T leptons plus electron and photon identification.
- Large acceptance in pseudorapidity with almost full azimuthal angle coverage everywhere.
- Triggering and measurements of particles at low p_T thresholds, providing high efficiencies for most physics processes.

3.2.2 Inner Detector

The Inner Detector, shown in Figure **??**, combines high resolution detectors at the inner radii with continuous tracking elements at the outer radii, all contained in the Central Solenoid. The highest granularity is achieved around the vertex region using semiconductor pixel detectors followed by the semiconductor tracker (SCT). The outer radius of the Inner Detector is 1.15 m and the total length is 7 m. The acceptance of the Inner Detector is limited to $|\eta| < 2.5$ due to the increasing amount of radiation damage induced in the detector at higher values of $|\eta|$. In the barrel region ($|\eta| \leq 1$) the detectors are arranged in concentric cylinders around the beam axis, while the end-cap detectors are mounted on disks perpendicular to the beam direction. See Figure **??** for a three dimensional cut-away view.

Good momentum resolution is provided by reconstructing the track along its full length. Low mass of the Inner Detector components enables good electromagnetic calorimeter performance.

Since the Inner Detector uses a solenoid magnet, in which the charged particles are deflected in the $x-y$ plane, the Inner Detector is designed to have the highest precision in the transverse plane. The momentum resolution typically achieved with the Inner Detector is

$$\frac{\Delta p_T}{p_T} = 0.04\% \times p_T \oplus 2\%$$

(p_T in GeV) and the impact parameter resolution is 15 μm in the transverse plane.

Pixel Detector

The Pixel detector will contribute between 3 and 6 precision measurements of the charged track coordinates over the full acceptance, determining the impact parameter resolution and the ability of the Inner Detector to reconstruct weakly decaying particles such as B-hadrons and τ leptons. The barrel part of the Pixel detector consists of three cylindrical layers each 80 cm long with radial positions of 50.5 mm, 88.5 mm and 122.5 mm. There are three disks on each side of the forward regions between radii of 9 and 15 cm arranged in 8 sectors, 6 modules per sector. A module is a 16.4 mm $\times$ 60.8 mm wafer with 46,080 pixel elements each 50 $\times$ 300 μm, giving a position resolution of 10 $\times$ 115 μm. A total of 80 million pixels (1456 modules in the barrel and 288

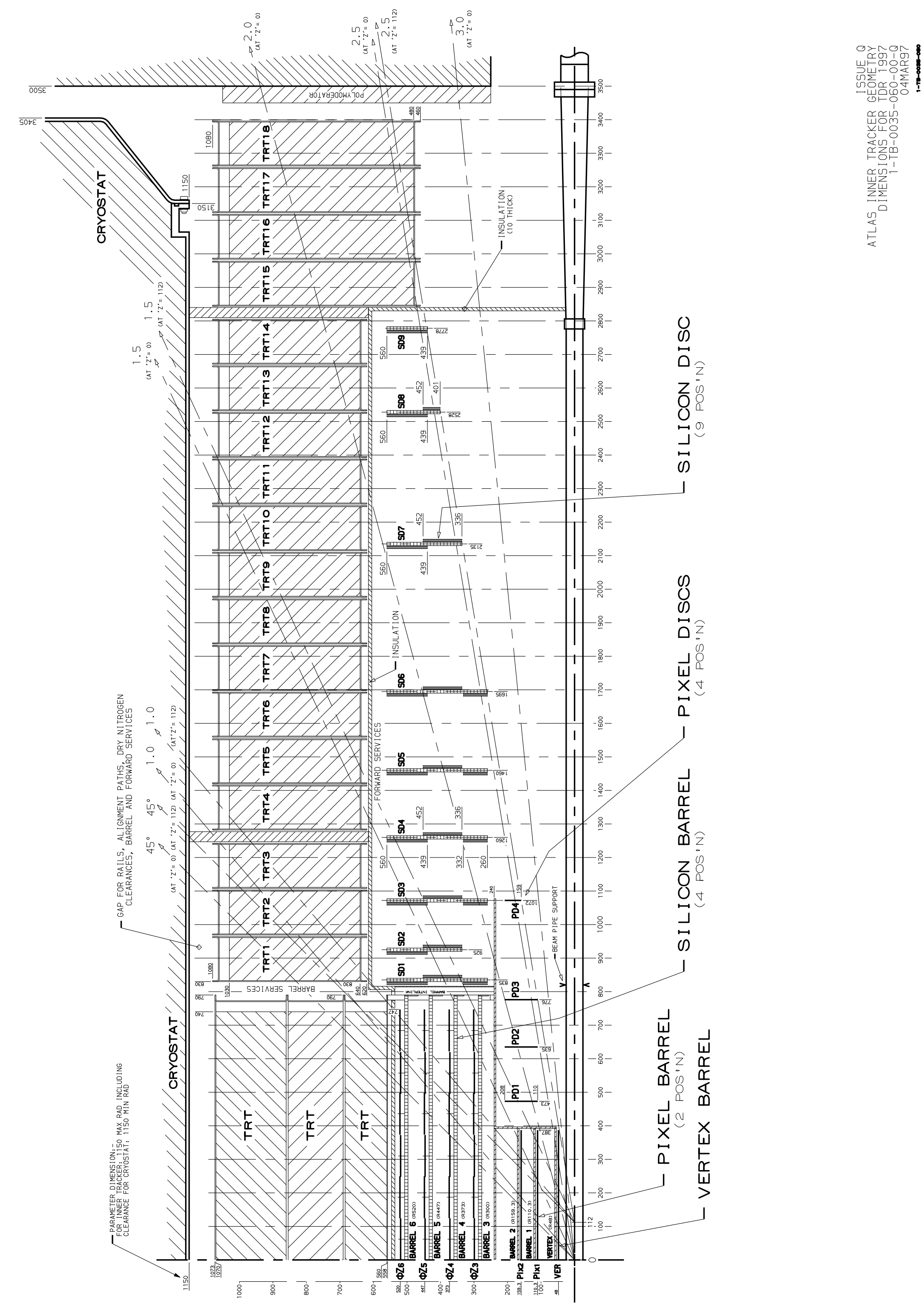

Figure 3.3: *Inner Detector of ATLAS (from [?]).*

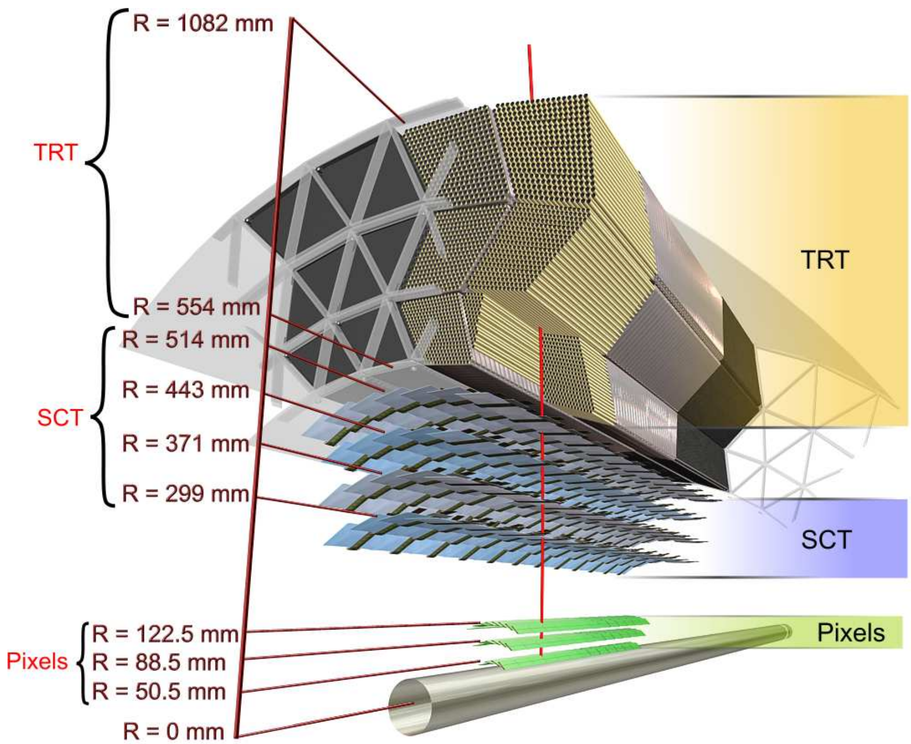

Figure 3.4: *Three dimensional cut-away view of the ATLAS inner detector (from [**?**]). The sensors and structural elements are shown being traversed by a 10 GeV charged track. The track traverses successively the beryllium beam-pipe, the three cylindrical silicon-pixel layers, the four cylindrical double layers of barrel silicon-microstrip sensors (SCT) and approximately 36 axial straws of 4 mm diameter contained in the barrel transition-radiation tracker modules within their support structure.*

modules in the end-caps) cover an area of 1.7 m^2. With a total of 80 million readout channels the Pixel detector contains about 50% of the total readout channels, a design and engineering challenge.

The Pixel detector uses a charge depleted layer of silicon to measure the charge deposition caused by the ionisation of a charged particle traversing the pixel. The Pixel detector measures the charge over threshold of the signal, which gives a measure of the amount of charge deposited in a single pixel. The charge distribution over adjacent pixels determines the hit position.

Crucial to the accurate identification of promptly produced particles and short-lived particles such as B-hadrons is the ability to accurately reconstruct primary and secondary decay vertices and associated particle decay lengths. The innermost barrel layer (called the B-layer) is positioned as close as possible to the beam pipe (which has an outer radius of 3.0 cm). The detector has been constructed to allow replacement of this layer in future since it will suffer heavy radiation damage, degrading its performance.

Semiconductor Tracker (SCT)

The SCT is similar in concept and function to the Pixel detector but with long, narrow strips rather than small pixels, making coverage of a larger area practical. It is composed of four double layers of silicon strips designed to provide between four and eight precision measurements per track in the intermediate radial range, contributing to the measurement of momentum, impact parameter and vertex position. The position resolution of an SCT module is $17 \times 580\ \mu$m. A small stereo angle between the strips in different layers is used to obtain a position measurement along the strip length, giving a point resolution in ϕ of $< 23\ \mu$m. The SCT is critical for basic tracking in the plane perpendicular to the beam, since it measures over a much larger area than the Pixel detector and with roughly equal (albeit one dimensional) accuracy. Each silicon detector is 6.36×6.40 cm^2.

A barrel module consists of two silicon sensors on each side forming a 128 mm long unit. A key component of each module is the hybrid (as shown in Figure **??**) which consists of a kapton polymide base with copper conductors. Polymide materials are lightweight, flexible and resistant to heat and chemicals. The modules receive power through 'pigtails' which are low mass cables, made of aluminum on kapton. Aluminium is used as a conductor due to the requirement to have minimum scattering. Indeed Aluminum has four times better conductivity than copper at the same scattering length. Each barrel module is built around a baseboard designed to have the lowest possible mass, to be mechanically rigid and to have good thermal performance. This is achieved by using graphite sheets and beryllium oxide (BeO) facing plates.

The barrel modules are mounted on carbon-fibre cylinders at radii of 30.0 cm (SCT1), 37.3 cm (SCT2), 44.7 cm (SCT3) and 52.0 cm (SCT4), i.e. four layers roughly equally spaced at 70 mm apart. The four barrel layers are tiled with 12 barrel modules along their length, the identical modules lining up in z. See Figure **??**.

The end-cap modules are very similar in construction but use tapered strips.

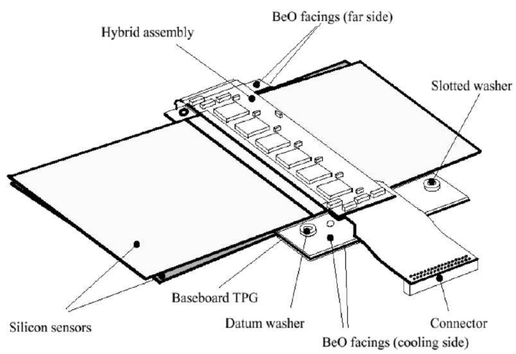

(a) A 3-D view of an ATLAS SCT barrel module. A Semiconductor Tracker module is a single unit consisting of 2 detectors and associated on-detector readout electronics. Each detector is made from 2 Silicon Wafers joined end to end and glued to a baseboard made from beryllia (BeO). Two single sided sensors are glued back to back with pyrolytic graphite (TPG) which increases thermal conductivity and so prevents hot spots.

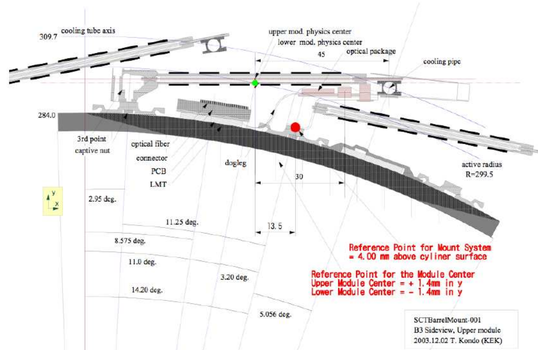

(b) The layout of modules mounted on a barrel is illustrated. The overlap between modules is shown.

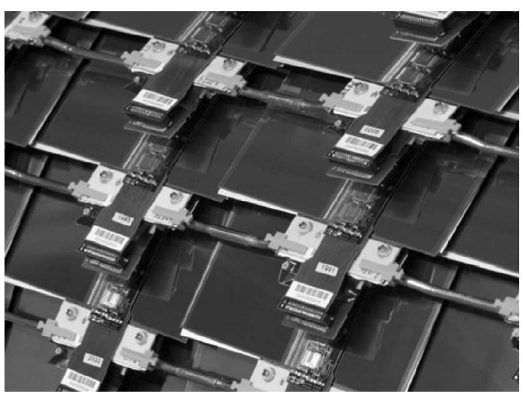

(c) The layout of modules mounted on a barrel is illustrated. The visible features include the overlap of the silicon of neighbouring modules, the stereo angle of the lower silicon sensors within a module and the hybrid assemby.

(d) The four SCT cylinders in the barrel region have radii between 299 mm and 514 mm and a full length of 1492 mm. Their surfaces are tiled with SCT barrel modules.

Figure 3.5: *ATLAS Semiconductor Tracker (from [?]).*

Transition Radiation Tracker (TRT)

The outer tracker of the Inner Detector is a combined straw tracker and transition radiation detector. The barrel part contains 52 544 axial straws, parallel to the beam direction, $\sim$150 cm in length at radii between 56 cm and 107 cm. The end-caps contain a total of 319 488 radial straws, located in planes perpendicular to the beam direction, at radii between 64 cm and 103 cm (inner end-caps) and 48 cm and 103 cm (outer end-caps). The total number of channels is 420 000 occupying a volume of 16.2 m^2. The 70 layers within the TRT provides on average 36 two-dimensional measurement points with 0.170 mm resolution for charged particle tracks. The resolution is much coarser than the silicon pixel and SCT detectors but this is a necessary sacrifice for covering a larger volume and having a different, complementary design.

The basic detection element is a 4 mm diameter carbon fibre reinforced kapton straw tube with a 30 μm diameter gold plated tungsten-rhenium (W-Re) wire. The straws are filled with a xenon gas mixture (70% Xe, 20% CF_4, 10% CO_2) thus adding electron identification capability (electron/pion separation) to the tracking capability. Alternating materials with very different refraction indices causes charged particles to produce transition radiation and leave much stronger signals in each straw. Xenon allows detection of transition radiation, CF_4 increases the charge drift speed, providing higher spatial resolution, and the CO_2 stabilises the gas mixture.

The distance of the trajectory from the wire can be determined by a drift time measurement. The ions created by a charged particle in a gas reach a constant speed when drifting to the wire. Thus there is a linear relation between measured drift time and drift radius. Electrons are more likely to generate transition radiation than photons. So electrons result in higher charge deposition being seen in the detector, giving so called 'High Threshold' (HT) hits. Also, the more ionising the particle, the longer the signal is over a certain threshold, 'Time-Over-Threshold' (ToT). Since electrons ionise more than pions, a longer ToT signifies an electron. With the ratio of HT hits and the ToT, the TRT provides capabilities to separate pions and electrons [**?**].

Inner Detector material budget

The ATLAS detector faces greater problems than previous experiments due to the large amount of material within the tracking detectors, resulting in electrons and photons traversing more radiation lengths of material before reaching the calorimeters. This increases the likelihood of electrons losing significant amounts of energy to bremsstrahlung radiation and photons converting within the Inner Detector.

Ideally, a detector would be able to measure the tracks of charged particles without interacting with the particle itself. However the required fine detector granularity allowing for accurate track reconstruction comes at a price in the form of material density. Figure **??** gives a breakdown of the material budget of the Inner Detector in terms of radiation length as a function of pseudorapidity. The probability of multiple scattering or bremsstrahlung in the Inner Detector is high and affects both the measurements of the track momentum and energy.

The high rates expected at the LHC make it impossible to transmit signals from the detector to electronics outside of the tracking volume. The electronics are therefore integrated into the active volume itself, which, along with the associated cabling, cooling systems and support structures, inevitably leads to increased material in the Inner Detector.

In the case of photons produced in the Inner Detector, around 40% convert into an electron-positron pair before reaching the calorimeters. This can cause significant tails in their reconstructed invariant mass distributions. Photon conversions can however be used for material mapping studies, such that they can be used to provide an 'X-ray' image of the Inner Detector (shown in Figure **??**).

3.2.3 Magnet System

ATLAS features four large superconducting magnets. The magnetic system is 22 m in diameter and 26 m in length, providing the magnetic field over a volume of approximately 12 000 m^3.

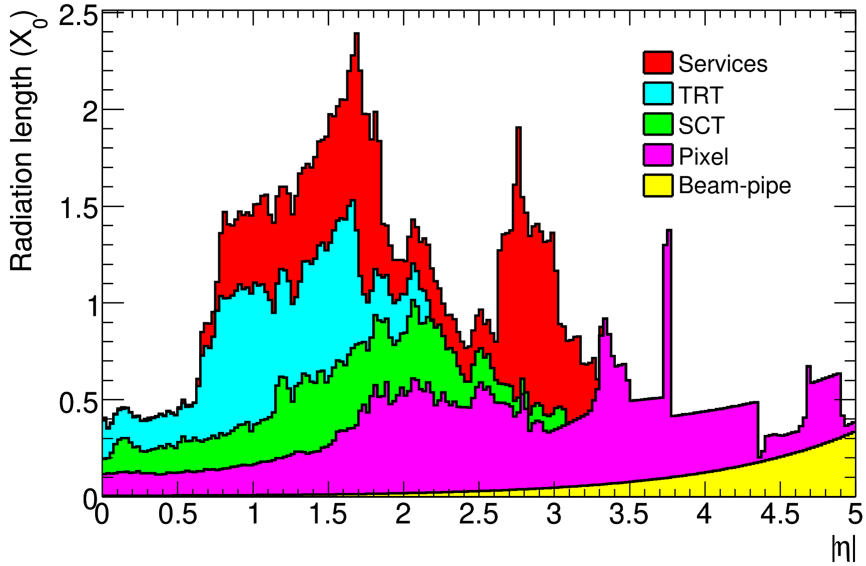

Figure 3.6: *Material distribution within the Inner Detector in radiation lengths, X_0, as a function of absolute pseudorapidity, averaged over azimuthal angle (from [**?**]).*

The magnet system consists of

- a central solenoid aligned on the beam axis providing a 2 T axial magnetic field for the Inner Detector.
- a barrel toroid and two end-cap toroids which produce a toroidal magnetic field for the muon detectors, ∼0.5 T in the central region and ∼1 T in the end-cap regions.

The design requirement for the central solenoid was for an extremely light-weight structure, to keep the material thickness in front of the calorimeter as low as possible. This has been achieved and the solenoid assembly contributes only about ∼0.66 radiation lengths at normal incidence.

The ATLAS solenoid is 5.3 m long, compared with the 6.7 m length of the tracking volume of the Inner Detector. Consequently the field deviates from uniformity. Maps of the magnetic field are shown in Figure **??**. The maximum magnetic field in ATLAS will be about 2.09 T. This is enhanced

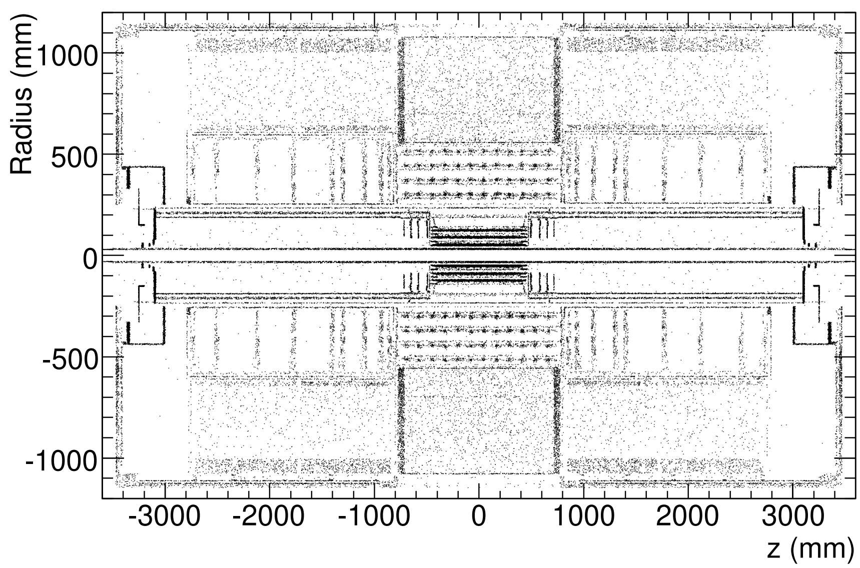

Figure 3.7: *An 'X-ray' image of the Inner Detector produced from detector simulation of photon conversions as a function of z and radius. It is possible to see the distribution of material in various structures of the Inner Detector (from [**?**]).*

by the iron in the Hadronic Calorimeter. It can be seen that the axial magnetic field component,B_z, falls to about 1.0 T at the end of the solenoid and 0.5 T at the end of the Inner Detector. The radial magnetic field component, B_R, becomes important for $|z| > 2$ m. The main effect of the non-uniformity is the need for more complex tracking algorithms which are consequently slower.

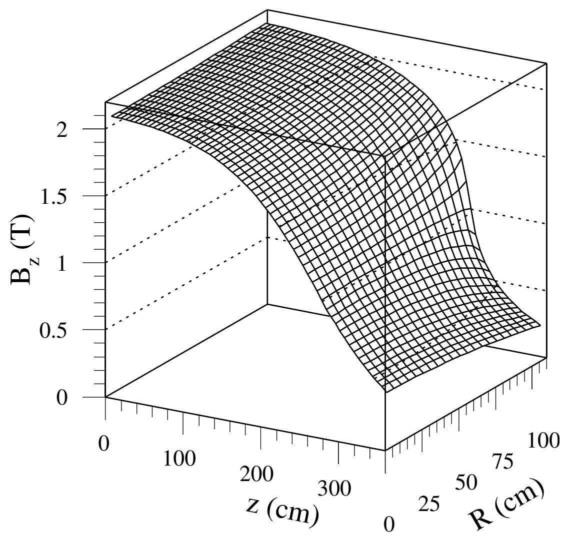

(a) Magnetic field map: B_z as a function of z and R

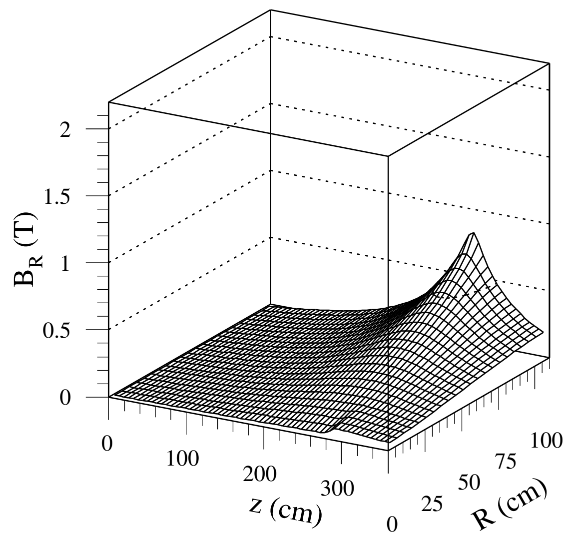

(b) Magnetic field map: B_R as a function of z and R

Figure 3.8: *The ATLAS solenoid is 5.3 m long, compared with the 6.7 m length of the tracking volume of the Inner Detector. Consequently the field deviates from uniformity and more complex tracking algorithms are required (from [**?**]).*

The barrel toroid, shown in the classic ATLAS photograph (Figure **??**), consists of eight coils encased in individual racetrack-shaped, stainless-steel vacuum vessels. The overall barrel toroid system is 25.3 m in length, with an inner diameter of 9.4 m and an outer diameter of 20.1 m. The cool down of the 360-tonne cold mass to 4.6 K takes five weeks.

The end-cap toroids generate the magnetic field required for optimising the bending power in the end-cap regions of the muon spectrometer system. They can slide along central rails, which facilitates opening the detector for access and maintenance. Each end-cap toroid consists of a

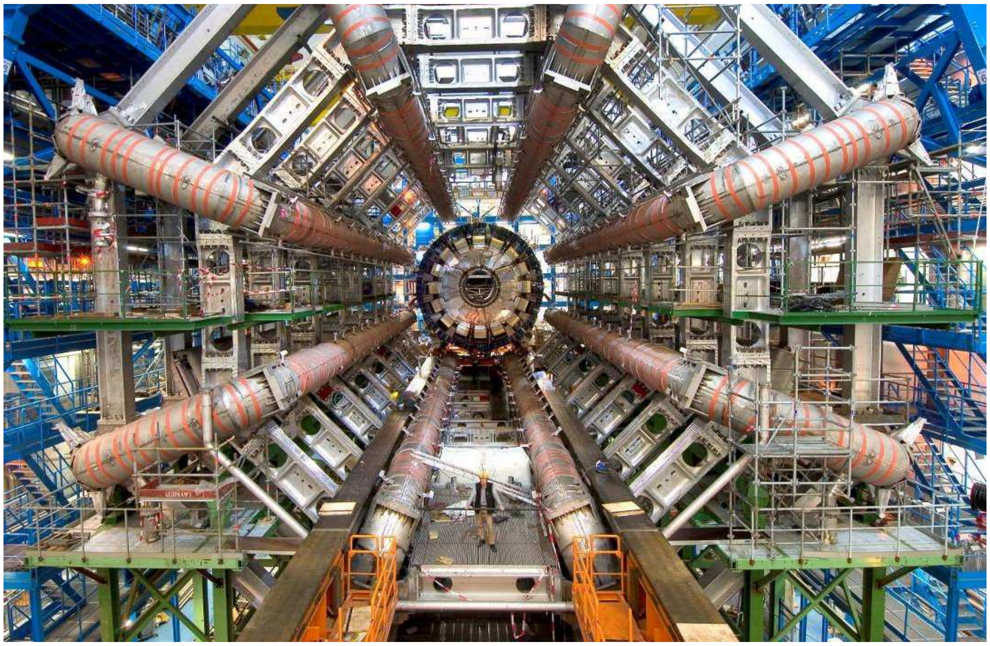

Figure 3.9: *ATLAS Barrel toroid as installed in the underground cavern (from [**?**]).*

single cold mass built up of eight flat, square coil units and eight keystone wedges, bolted and glued together into a rigid structure with a mass of 240 tonnes.

3.2.4 Calorimetry

Calorimeters are required to measure the energy and direction of photons, electrons, isolated hadrons and jets as well as missing transverse energy.

The precision electromagnetic calorimeters are lead-liquid argon detectors with accordion shaped absorbers and electrodes. The outer hadronic calorimeters consist of scintillator tiles interspersed with steel absorbers, to alternately start and measure hadronic showers.

ElectroMagnetic Calorimeters

The electromagnetic calorimeter (Figure **??**) uses dense 'absorbers' made from lead to cause particle showers, which are interleaved with liquid-argon layers that cause electron ionisation registered on copper electrodes. Liquid argon was chosen as the active detector medium due to its linear behaviour and intrinsic radiation hardness.

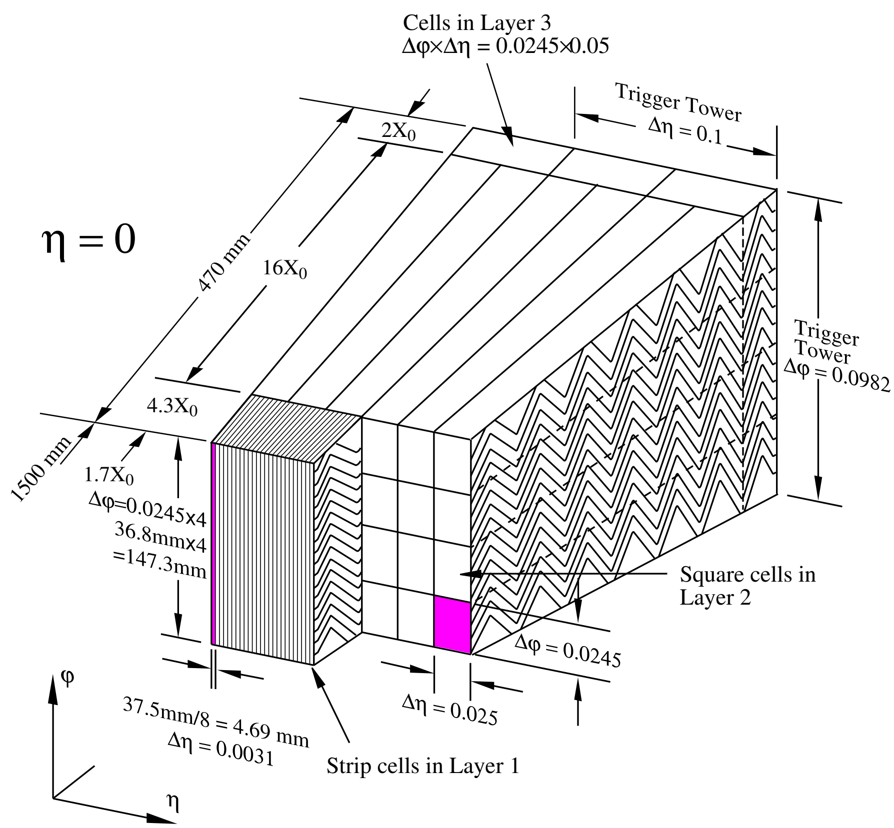

Figure 3.10: *The electromagnetic calorimeter is a sampling calorimeter using liquid argon as active material and lead as absorber, covering the pseudorapidity region $|\eta| < 3.2$. The absorber and the electrodes used to collect the ionization charge are longitudinally folded in an accordion shape to obtain a crack-less detector in ϕ. In the central region $|\eta| < 2.5$, suited for precision measurements, the calorimeter is longitudinally divided into three layers (called 'strip', 'middle' and 'back') each highly segmented in $\eta \times \phi$ (from [**?**]).*

The accordion geometry of the absorber plates provides a full coverage of ϕ without any cracks. The wave amplitude and folding angle is carefully designed such that it varies resulting in a very uniform performance in linearity and resolution as a function of ϕ.

The barrel calorimeter is complemented with a liquid-argon presampler detector, placed in front of its inner surface. The presampler is used to obtain a measurement of the particle energy before the particle crosses material at the entrance to the main calorimeter, and allows correction for the energy loss upstream of the calorimeter.

The total thickness of the electromagnetic calorimeter is more than 24 radiation lengths in the barrel and more than 26 radiation lengths in the endcaps. The liquid-argon calorimeter has an energy resolution (E in GeV) of

$$\frac{\Delta E}{E} = \frac{10\%}{\sqrt{E}} \oplus 0.7\%$$

and a resolution of the polar direction of a particle shower of

$$\Delta\theta = \frac{50 \text{ mrad}}{\sqrt{E}}$$

Hadronic Calorimeters

The hadronic calorimeter surrounds the electromagnetic calorimeter and covers the range $|\eta| < 4.9$. The hadronic calorimeter must provide good containment of hadronic showers and reduce punch through into the muon system to a minimum. At $|\eta| = 0$ the total thickness is 11 interaction lengths. This, coupled with the large η coverage, should allow for good measurements of missing transverse energy.

The barrel hadronic calorimeter, at $|\eta| < 1.6$, uses steel absorber tiles, interleaved with plastic scintillator tiles, to alternately start and measure hadronic showers. The endcap hadronic calorimeter receives a much higher dose of radiation than the barrel and therefore uses the radiation-hard liquid argon technology with copper absorbers in a parallel plate geometry.

The forward calorimeter (FCal) covers the region $3.1 < |\eta| < 4.9$, where the radiation levels are especially high. The calorimetry here is of a high-density liquid argon design constructed from copper and tungsten so as to limit the width and depth of showering, reduce the leakage from the FCal into neighbouring calorimeters and decrease radiation background in the muon spectrometer. In the forward region the energy resolution is

$$\frac{\Delta E}{E} = \frac{100\%}{\sqrt{E}} \oplus 10\%$$

3.2.5 Muon System

High momentum final state muons are among the most promising and robust signatures of physics at the LHC. The ATLAS muon system serves a double purpose: as a trigger to select events containing muons above certain energies and as a precision muon spectrometer.

A choice was made for a large air toroid magnet to achieve a stand-alone muon system at high luminosities. The key features are:

- Good transverse momentum resolution with performance goal of 10 % for 1 TeV tracks.
- A pseudorapidity coverage of $|\eta| < 2.7$ for momentum measurements and $|\eta| < 2.4$ for trigger items.
- Excellent charge identification.

The muon spectrometer forms the outer part of the ATLAS detector. Precision-tracking chambers in the barrel region are located between and on the eight coils of the superconducting barrel toroid magnet, while the end-cap chambers are in front and behind the two end-cap toroid magnets.

The chambers in the barrel are arranged in three concentric cylindrical shells around the beam axis at radii of approximately 5, 7.5 and 10 m (see Figure **??**). In the two end-cap regions, muon chambers form large wheels located at distances $|z| \sim 7.4$, 10.8, 14 and 21.5 m from the interaction

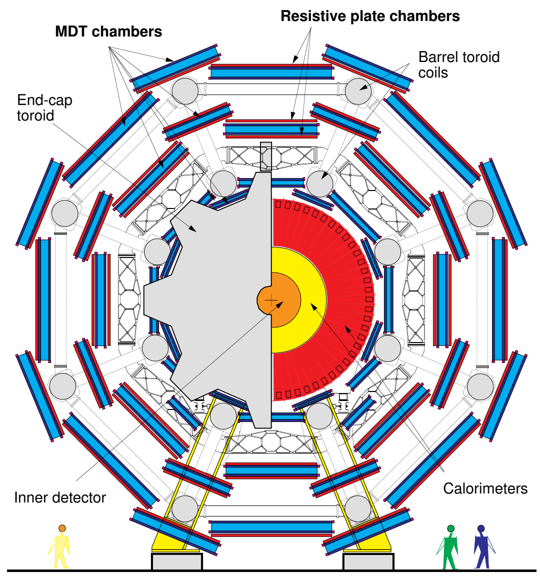

Figure 3.11: *Cross-section of the barrel muon system perpendicular to the beam axis (non-bending plane), showing three concentric cylindrical layers of eight large and eight small chambers. The outer diameter is about 20 m (from [**?**]).*

point. In the centre of the detector ($|\eta|$=0) a gap in chamber coverage has been left open for services. Additional gaps in the acceptance occur in sectors 12 and 14 due to the detector support structure (feet).

The precision momentum measurement is performed by the Monitored Drift Tube (MDT) chambers, which combine high measurement accuracy, predictability of mechanical deformations and simplicity of construction. They cover a pseudorapidity range $|\eta| < 2.7$ (except in the innermost end-cap layer where their coverage is $|\eta| < 2.0$). These chambers consist of three to eight layers of drift tubes, operated at an absolute pressure of 3 bar, achieving an average resolution of 80 μm per tube or 35 μm per chamber.

In the forward region Cathode-Strip Chambers are used in the innermost tracking layer due to their higher rate capability and time resolution. The Cathode-Strip Chambers are multiwire proportional chambers with orthogonal cathode planes. The resolution of a chamber is $\sim$40 μm in the bending η plane and 5 mm in the transverse ϕ plane.

The precision-tracking chambers are complemented by a system of fast trigger chambers capable of passing track information within a few tens of nanoseconds after the passage of the particle. Resistive Plate Chambers (RPC) are used in the barrel and Thin Gap Chambers (TGC) in the end-caps (Figure **??**). The trigger chambers measure both coordinates of the track, one in the bending plane and one in the non-bending plane. The MDT and trigger chamber hits are matched in the bending plane. When correlated close-by muon tracks occur the ambiguity in η and ϕ will be resolved by matching the muon track candidates with tracks from the Inner Detector.

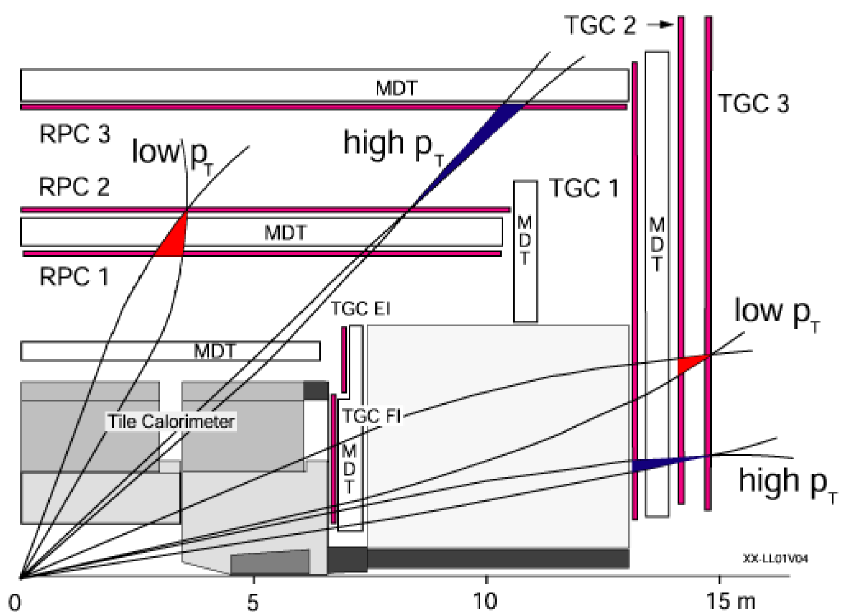

Figure 3.12: *Muons are identified using the so-called Trigger chambers, resistive-plate chambers (RPC) in the barrel, and thin-gap chambers (TGC) in the endcaps (from [**?**]).*

The Inner Detector has excellent pattern recognition properties, with an efficiency of above 99% for finding muons with p_T =20 GeV, even in the presence of the pile-up expected at design luminosity And efficiency of ∼90% can be obtained for tracks with $p_T > 1$ GeV, with cuts which ensure that the fraction of fake tracks anywhere in the acceptance remains below $\sim$0.5 % [**?**].

3.2.6 Trigger and Data Acquisition

The high interaction rate at the LHC creates an enormous challenge for trigger and data-acquisition. The trigger system will select about 100 interesting events out of 10^9 every second. The task of the trigger/Data Acquisition (DAQ) system is to select interesting physics and to move the data for those events from the detector to permanent storage for offline analysis. The system is based on three levels of online event selection, summarised in Figure **??**. Each trigger level refines the decisions made at the previous level and applies additional selection criteria if necessary. The ATLAS trigger needs to reduce the incoming interaction rate of 1 GHz to a final $\sim$200 Hz equivalent to $\sim$200 Mbytes of data per second. Huge computing resources will be required to store, reconstruct and analyse the data recorded.

Level-1 (LVL1) Trigger

The LVL1 trigger system consists of the calorimeter trigger, muon trigger, central trigger processor (CTP) and the timing, trigger and control (TTC) system. It makes an initial selection based on reduced granularity data from a subset of detectors. The calorimeter trigger uses all of the electromagnetic and hadronic calorimeters but with reduced granularity searching for electromagnetic clusters, jets and large missing and total transverse energy. The data from the subdetectors is passed to the hardware processors which summarise the event. The features are then passed to the central trigger processor which makes the overall decision to accept or reject the event. The Level-1 trigger reduces the rate to 75–100 kHz, which is then passed to the Level-2 software-based trigger system.

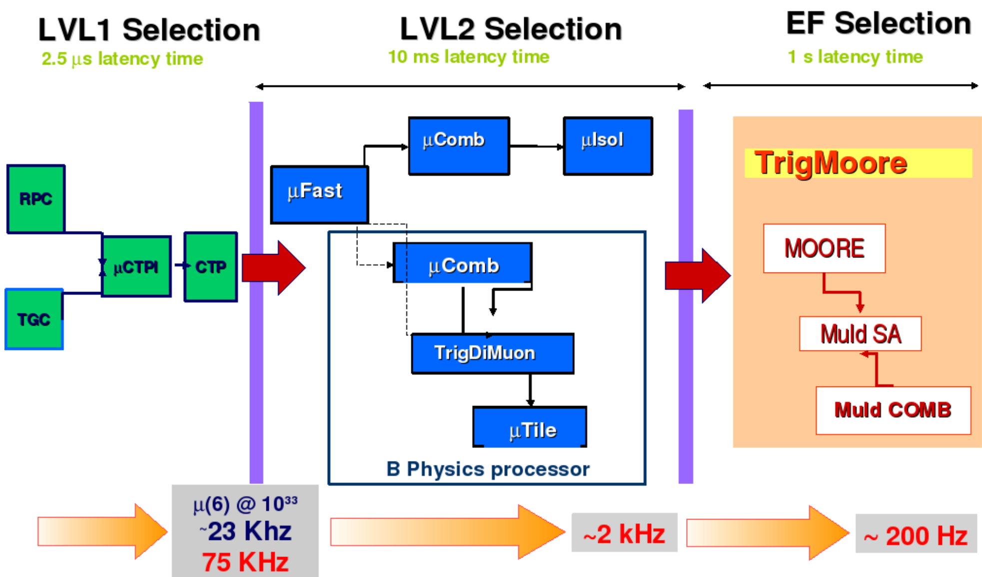

Figure 3.13: *LVL1 muon trigger sends the information from the barrel resistive-plate chambers (RPC) and the endcap thin-gap chambers (TGC) to the Central Trigger Processor (CTP). The LVL2 muon trigger is entirely software based with a time budget of 10 ms per event. MuFast uses information from the muon spectrometer to estimate the position in* η *and* ϕ *and transverse momentum of the LVL1 candidates. MuComb combines the muon track reconstructed in the muon spectrometer with a corresponding track in the Inner Detector to refine estimates. MuIso implements a calorimetric isolation algorithm taking information from electromagnetic and hadronic calorimeters. The Event Filter is entirely software based with a time budget of* $\sim$*1s per event, allowing more precise measurements and further fake rejection.*

Level-2 (LVL2) Trigger

The Level-2 trigger reduces the event rate to around 2 kHz. The full event granularity is available within a Region of Interest (RoI), essentially a geometrical region of the ATLAS detector identified by the Level-1 trigger as containing the relevant physics information. Only event data in regions around η and $\phi(\Delta\eta \times \Delta\phi = 0.75 \times 0.75)$ flagged by Level-1 (with electromagnetic, tau, jet or muon candidates) is retrieved from the read-out buffers (ROB). The advantage of buffering the data until a Level-2 decision is made is that only 1-4 % of the data volume is unpacked and analysed, saving time especially in the data preparation and reconstruction algorithms (feature-extraction algorithms). The only exception from this scheme are B-physics candidates, where the entire event needs to be read-out, known as Full Scan (FS). If the event is accepted, the Level-2 output is appended to the event and full event building is done.

Event Filter (EF)

The EF is responsible for the last stage of the trigger, reducing the data to about 200 Mbytes/s equivalent to event rate of 200 Hz. As far as possible, offline code will be used at this stage, with access to the full event data, geometry and calibration constants. However, compared to the offline reconstruction, which reconstructs the entire event, at the EF only partial reconstruction within the Level-2 RoI's is done. Upon the trigger accept the EF output is appended to the event, and the event is written to mass storage. Level-2 and EF together are called High-Level Trigger (HLT).

Trigger menu

A flexible trigger menu is used in ATLAS to allow different types of data to be selected for further analysis. Items on the trigger menu have to be optimised based on expected rates of the physics events to be recorded. Prescales are added if the event rate is too high for that trigger item.

The trigger I propose using is the EF_MU4_Je5e3_FS. It requires one muon with p_T greater than 4 GeV and two electromagnetic clusters in the Level-1 trigger. That muon is to be confirmed in the Level-2 trigger, by using data from precision chambers and reconstruction of tracks in full acceptance of SCT and pixels. At event filter level the event is selected by requirement of two electrons (with p_T of at least 5 and 3 GeV), a reconstructed J/ψ (ee) mass between 1.5 and 3.8 GeV, $\Delta\eta$ and $\Delta\phi$ of track pair less than 1.

3.3 Software Tools

3.3.1 ATLAS software

The ATLAS software is implemented in the Athena [**?**] framework. A whole software release is identified by a group of three integers separated by dots e.g. 14.2.1, where the first number is the major release, the second indicates developer realeases, and the third indicates minor changes.

3.3.2 ATLAS data

There are several stages of processing data:

RDO: Raw Data Objects are the output from the Event Filter. Each event is ∼1.6 MB in size. Raw data is in ‘bytestream’, reflecting the way the data arrives from the detector.

ESD: Event Summary Data is the output from the reconstruction process. It is in object orientated format with an event size of ∼500 kB. The ESD retains some information about individual hits inside subdetectors. The aim of the ESD is to make access to the Raw data unnecessary for most physicists except for some calibration and re-reconstruction.

AOD: Analysis Object Data is derived from ESD and is ∼100 kB per event. It is designed for physics analysis.

DPD: Derived Physics Dataset is a file that contains information on events, selected for a specific study. It is skimmed (events removed), slimmed (details removed from objects), and thinned (unnecessary objects removed). dESDs and dAODs take their name from their derived data format.

The size of data objects stated above are aspirational. All formats are currently larger, for early data taking.

The ATLAS Metadata Interfaces, AMI [**?**], framework provides a web interface that can be used by physicists as a starting point for searching available datasets and getting detailed information about them using their physics metadata attributes.

3.3.3 Full Chain Simulation

Simulated or Monte Carlo (MC) data can be used to test our understanding of current models as well as making predictions. Clearly without data from real collisions MC allows us to prepare the software and analyses. The steps to simulate and reconstruct events are essentially:

Event generation: The first step is to produce simulated events. The simulation needs to model proton-proton collisions and the gluons, gauge bosons and quarks that are produced, as well as their hadronisation into longer lived particles. The physics processes involved are described in event generators, such as Pythia [**?**]. However only about 1% of collisions at LHC are expected to produce a $b\bar{b}$ pair and only a fraction of these will hadronise into the particular particle of interest. Therefore many B-Physics studies use a specialised interface to Pythia called PythiaB [**?**]. Pythia generates a partonic event. PythiaB then checks if the event contains a $b\bar{b}$ quark, clones the event a number of times and then allows the events to hadronise freely (according to forcings set by user). In this manner big CPU savings are made in the generation process. Dataset numbers alongside the process name are assigned to uniquely identify MC data.

The underlying event is an important element of the hadronic environment within all physics at the LHC. Parton distribution functions (PDFs) are carefully modeled to take into account the flavour structure of previous interactions and not only the overall energy momentum constraints. For 2008 MC, Pythia [**?**] uses CTEQ6 [**?**]. For 2009 MC tuning see [**?**].

Detector Simulation: The next step is to model the events as they pass through the detector. The interactions of the generated particles with the detector are performed by GEANT4 [**?**]. A detailed description of the ATLAS geometry and material distribution is used. The GEANT4 algorithms transport the particles through the magnetic field and simulate material interactions such as multiple scatterings, bremsstrahlung, energy loss and photon conversions. Some long-lived particles like kaons are also decayed by GEANT4. After these effects have been taken into account GEANT4 converts the trajectories of the charged particles into 'Hits', or energy deposits, in the subdetectors. Different models of the ATLAS geometry can be used at this stage. These models can be used to analyse the effects of so-called detector misalignment and its impact on detector performance.

Digitisation: The response of the detector to these 'Hits' is simulated. The output format of digitisation is equivalent to the real data, when it arrives, which will be in the form of 'bytestream'. The detector response is converted into RDOs so that reconstruction can take place.

Reconstruction: Various algorithms are used to reconstruct the event. This includes pattern recognition, track fitting, energy measurement and particle identification as well as reconstruction of high level physics objects such as tracks, electrons and muons which are stored in ESD format. ESDs are then converted to a more compact format for physics analyses.

Re-reconstruction: Since reconstruction and calibrations will continually improve, even after reprocessing, it may be necessary to re-reconstruct and recalibrate a fraction of events. Re-reconstruction also permits a different track fitter to be applied to a chosen dataset. By default, track fitting is done with pion particle hypothesis. This does not allow the track to account for bremsstrahlung for electrons, which, due the amount of material in the Inner Detector, is an all too common occurrence. Track Refitting can either be carried out by full re-reconstruction of the RDO (or ESD) or by using the egamma refit tool [**?**] on identified electron tracks in AOD. Currently track refitting on AOD can be done with two bremsstrahlung-aware track fitters, Gaussian Sum

Fitter and Aggressive Dynamic Noise Adjustment (see Chapter **??** for description of the different track fitters).

3.3.4 The Grid

One year of data taking at the LHC results in $\sim$40 Petabytes (40 million of Gigabytes) of data, produced by the four experiments. The data will be analysed by physicists worldwide. For the LHC, storage and processing requirements exceed by far the capacities available at any single site and hence a new approach has been chosen, the LHC Computing Grid. This computing grid provides the infrastructure for the storage of the data and the necessary computing power for reconstruction, physics analyses and simulations.

The computing model requires that a physicist sends their code to the data, which is stored remotely on the Grid. The main interface that handles the sending of code to the Grid is Ganga [**?**]. Pathena is an alternative client tool which uses only the Panda [**?**] backend. The user defines the datasets, code to run and software release to be used. If all goes well the code is run and the results (ntuples and logfiles) are returned to the user.

The data distribution follows a so-called tier-structure:

Tier 0: This is CERN where the raw data is produced. The data will be archived and distributed to Tier 1 sites.

Tier 1: ATLAS will have about 10 Tier 1 sites around the world. Each Tier 1 site will have access to around 1/10th of the RDOs as well as 1/5th of the ESDs and AODs. Any ESD or AOD will be available from at least two Tier 1 sites.

Tier 2: These are regional facilities. They will provide analysis capacity and be used to host DPDs.

Tier 3: These are university clusters or individual scientists' computers.

Several tests of the Grid infrastructure (data challenges) have been preformed during the last years to ensure the full functionality of the Grid with the start of the data taking.

3.4 Electron Reconstruction and Identification

3.4.1 Reconstruction

There are three algorithms, often referred to as 'authors', for electron reconstruction [**?**]:

- Calorimeter seeded: This algorithm is seeded by a cluster reconstructed in the electromagnetic calorimeter ($p_T > 3$ GeV). This is tuned for high p_T electrons.
- Softe: Starts from an Inner Detector track, with high threshold TRT hits and $p_T > 2$ GeV, then looks for cluster match. This is tuned for low p_T electrons ($p_T < 5$ GeV).
- Forward: For $|\eta| > 2.5$. No track matching is required for forward electrons due to the limited coverage of the tracking system i.e. no Inner Detector information.

I have studied the efficiency of the calorimeter seeded and softe algorithms, producing Figure **??** for 15 GeV single electrons [1)]. The softe algorithm makes a big impact at low p_T. Efficiency in p_T rises from ∼40% at 2 GeV to ∼90%. Efficiency of electron reconstruction is ∼80% in the barrel region and reduces to ∼50% in the endcaps.

Collections of physics particles are stored in different containers. Candidate electrons are stored in the Electron Container. The electron object has an associated p_T built from perigee parameters along with energy from calorimetry and a track p_T calculated from tracking information.

3.4.2 Identification

Electron identification is based on the use of variables which are intended to distinguish between the electron and background e.g. pions and jets.

[1)] in Athena release 14.2.0

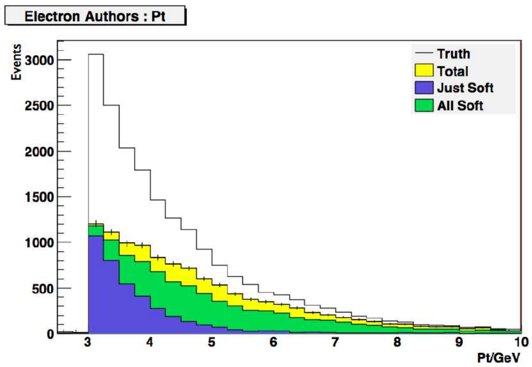

(a) Total numbers of electron candidates reconstructed wrt p_T.

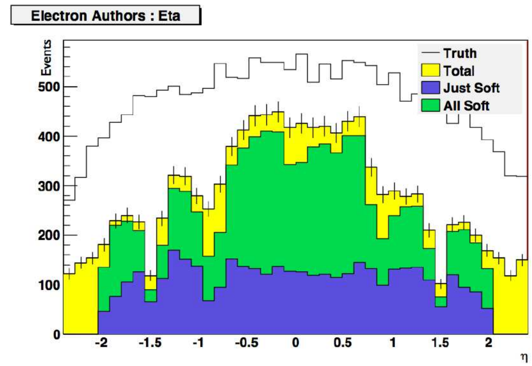

(b) Total numbers of electron candidates reconstructed wrt η.

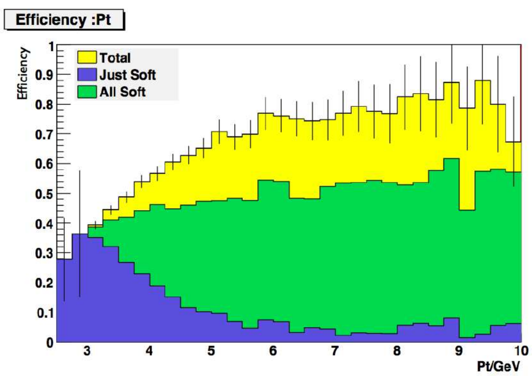

(c) Electron reconstruction efficiency wrt Pt

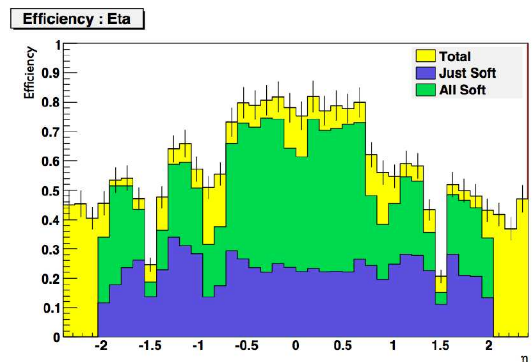

(d) Electron reconstruction efficiency wrt η

Figure 3.14: *Efficiency of electron reconstruction shown for electrons from prompt J/ψ. An electron candidate may be found with the calo seeded (cluster based) and softe (track based) algorithm. The electron candidates found only with the softe algorithm are labelled 'Just Soft' and shown in blue. The electron candidates found with both algorithms, the overlap, are labelled 'All Soft'. The total number of electron candidates identified are labelled 'Total'. Thus the electrons found only with the calo seeded algorithm are shown in yellow. It is noticeable that softe algorithm makes a big impact at low p_T. Efficiency in p_T rises from ∼40% at 2 GeV to ∼90% at 10 GeV. Efficiency of electron reconstruction is largest in the barrel region and reduces to ∼50% in the endcaps.*

There is a set of electron quality criteria used as the default method used in electron identification. See Table **??** [**?**].For all electron candidates the candidate has to pass a series of cuts based on the shower shape properties in different compartments of the calorimeter as well as variables combining Inner Detector and Calorimetry information. Calorimeter information only is used for Loose cuts. Medium cuts include tracking information, resulting in increased jet rejection. The Tight electron requirements are explicitly optimised to exploit the full potential of the ATLAS electron identification with the purpose of specifically rejecting charged hadrons and electrons from photon conversions. Charged hadrons are rejected by using E/p and the fraction of high-threshold hits in the TRT. Background electrons from photon conversions are rejected by requiring the presence of a hit on the track in the pixel vertexing layer and rejecting candidates with a matching conversion vertex.

Loose cuts:	
cluster η range	$\eta < 2.47$
Lateral width of EM shower (to reject pions with wide showers)	$< 0.0125 - 0.0160$m
Medium cuts:	
Total EM shower width	1.40 - 4.10
Number of hits in pixel layers	> 0
Number of hits in pixel and SCT	> 8
Tight cuts:	
Number of hits on B layer	> 0
$\Delta\eta$ between cluster and track	< 0.005
$\Delta\phi$ between cluster and track	< 0.02
Ratio of cluster energy to track momentum	$0.7 - 0.8 < E/p < 2.5 - 5.0$
Total number of TRT hits	15
Ratio of number of high-threshold hits to the total number of TRT hits	$> 0.08 - 0.155$

Table 3.1: Summary of electron quality criteria. Loose, Medium and Tight cuts. From [**?**].

The data sample collected by ATLAS at 900 GeV at the end of 2009 has yielded 879 electron candidates with transverse energy greater than 2.5 GeV before identification cuts [**?**].

'You can't stamp an identification number on an electron, or paint a spot on it —if you've seen one, you've seen them all...an electron is an electron is an electron.'

David Griffiths. Introduction to Elementary Particles.

4

Passage of Particles Through Matter

My main sources for this chapter were the Particle Data Group [**?**]; Griffiths, 'Introduction to Elementary Particles' [**?**]; Wikipedia [**?**] and Perkins, 'Introduction to High Energy Physics' [**?**]. May I refer the reader to these references for a fuller description of this subject.

The track reconstruction of modern high energy physics experiments is a very complex task. The ATLAS detector's ability to reconstruct tracks with high precision is critical both for the calibration of the detector and for the analysis of physics processes. Understanding the passage of particles through matter is clearly fundamental to achieving high performance of the tracking algorithms as the particles traverse the different layers and materials designed to detect them.

The relatively large amount of material within the 7 000-tonne ATLAS detector generates considerable disturbances to the particle tracks through interactions with detector material.

The energy loss of heavy particles in the energy range of final state particles originating from high energy collision experiments is dominated almost entirely by ionisation loss. For electrons, the energy loss is slightly different since they suffer much larger losses by bremsstrahlung.

In this chapter I will describe the key processes that are involved as particles traverse detector material and the units used for material descriptions.

4.1 Ionisation and atomic excitation

Ionisation and atomic excitation dominate energy loss in matter for all moderately relativistic charged particles, other than electrons. The mean rate of energy loss (or stopping power) can be approximated using the Bethe-Bloch equation [**?**],

$$-\frac{dE}{dx} = Kz^2 \frac{Z}{A} \frac{1}{\beta^2} \left[\frac{1}{2} ln \frac{2m_e c^2 \beta^2 \gamma^2 T_{max}}{I^2} - \beta^2 - \frac{\delta(\beta\gamma)}{2} \right] \tag{4.1}$$

where β and γ follow from the velocity of the particle: $\beta = v/c$, $\gamma = 1/\sqrt{1-\beta^2}$ and m_e is the mass of the electron, 0.510 MeV. T_{max} is the maximum kinetic energy which can be transferred to a free electron in a single collision and the other variables are defined in Table **??**. To find the energy loss per unit of thickness, dE/dx needs to be multiplied by the density of the traversed medium. Figure **??** illustrates the function as computed for muons in copper.

In high-energy physics dE/dx in a given material is essentially a function only of β. For track reconstruction, the energy losses are small. dE/dx is also a function of the ratio of the particle mass to the particle momentum and thus ionisation loss can play an important role in particle identification, in momentum range less than ∼1 GeV. Figure **??** shows the dependence of dE/dx on

Symbol	Definition	Units
E	Incident particle energy γMc^2	MeV
T	Kinetic energy	MeV
K/A	$4\pi N_A r_e^2 m_e c^2/A$	0.307075 $\mathrm{MeVg^{-1}cm^2}$ for A=1$\mathrm{gmol^{-1}}$
ze	Charge of incident particle	
Z	Atomic number of absorber	
A	Atomic mass of absorber	
I	Mean excitation energy	eV (Nota bene!)
$\delta(\beta\gamma)$	Density effect correction to ionisation loss	

Table 4.1: *Summary of variables in Bethe-Bloch equation.*

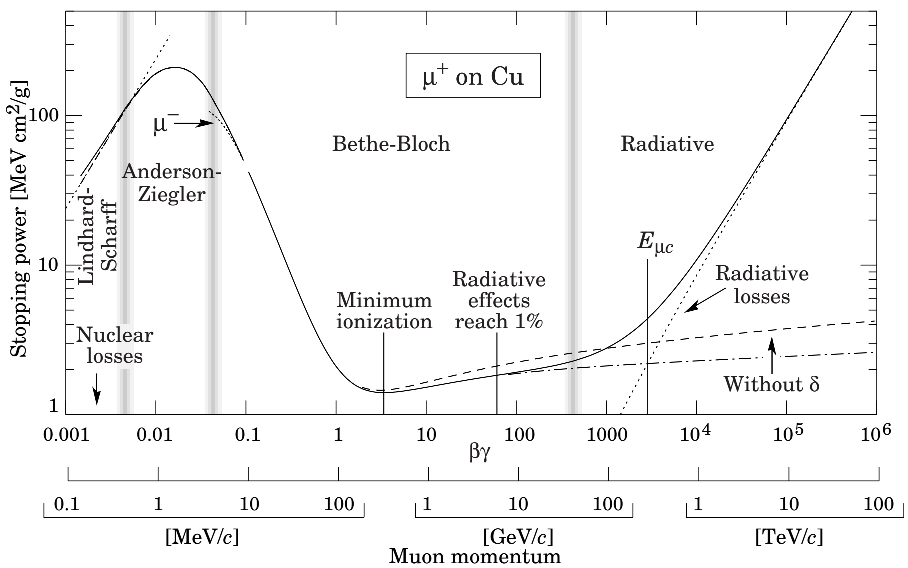

Figure 4.1: *Stopping power ($=-dE/dx$) for positive muons in copper as a function of $\beta\gamma = p/Mc$, where M is the mass of the particle with momentum p. Solid curves indicate the total stopping power. Vertical bands indicate boundaries between different approximations.* [**?**]

the track momentum and charge. Protons and kaons are easily identifiable at low momentum for the higher energy deposit.

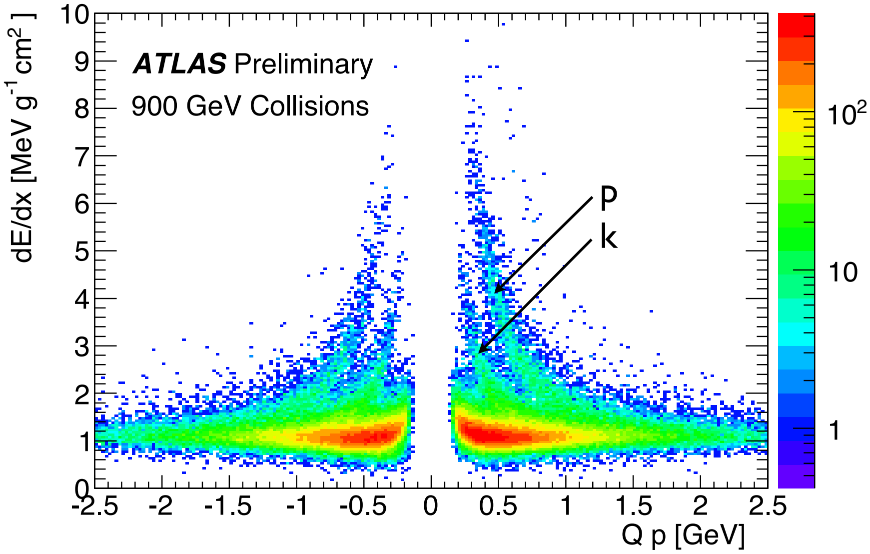

Figure 4.2: *This plot shows the dependence of the dE/dx on the track momentum and charge. Band structures for different particle types are seen. Bands for protons and kaons are identifiable at low momentum for the higher energy deposit. Tracks are selected to have at least three barrel pixel hits. The plot is based on about 180k tracks, i.e. about 10% of the collision data. [**?**]*

4.1.1 Landau Distribution and most probable Energy Loss

The Bethe-Bloch formula only describes the expected mean energy loss of charged particles due to ionisation. In reality, ionisation loss is a stochastic process that leads to asymmetric fluctuations around a most probable value.

The distribution of energy loss in a thin absorber is better described by Landau theory. This description is characterised by a narrow peak with a long tail for positive values. The tail comes from the small number of individual collisions, each with a small probability of transferring comparatively large amounts of energy [**?**]. For very thick absorbers the distribution is less skewed but never approaches a Gaussian.

The Landau distribution is used in ATLAS tracking for the calculation of the most probable energy loss of heavy particles.

4.2 Multiple Coulomb scattering

A charged particle traversing a medium is deflected by many small-angle scatters. The Coulomb scattering distribution is roughly Gaussian for small deflection angles.

Multiple scattering is however only approximately Gaussian. Occasional large angle single scattering processes disturb the Gaussian distribution and add large non-Gaussian tails. As a rule of thumb, the assumption of a Gaussian character is valid to about 98% [**?**].

Clearly the number of radiation lengths seen by a particle traversing the detector should be minimised to prevent loss of tracking performance due to multiple scattering. Two tracking detector technologies with minimal material are drift chambers and silicon. Both are used in the Inner Detector.

From the tracking point of view, multiple coulomb scattering is by far the dominant contribution to the directional deflection of a particle traversing material [**?**].

4.3 Electron interactions in matter

At low energies electrons and positrons primarily lose energy by ionisation, although other processes contribute, as shown in Figure **??**. Bremsstrahlung losses rise nearly linearly and dominate above a few tens of MeV in most materials.

The critical energy, E_c, is the energy at which the loss rates due to bremsstrahlung and ionisation

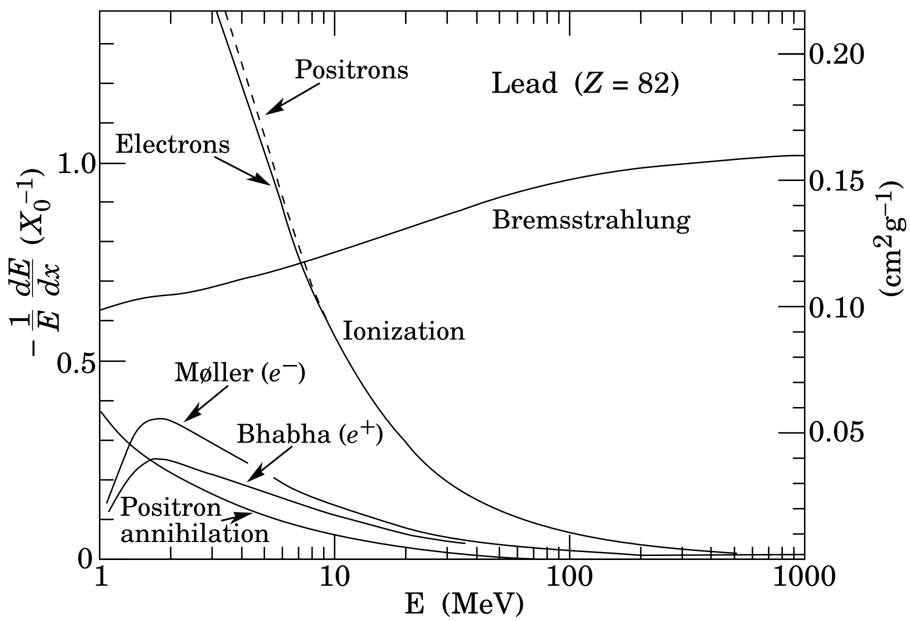

Figure 4.3: *Fractional energy loss per radiation length in lead as a function of electron or positron energy [**?**]. Møller scattering is the name given to electron-electron scattering and Bhabha scattering is the electron-positron scattering process. Positron annihilation can occur when positrons pass through matter annihilating with an electron, to create photons.*

are equal. The critical energy for electrons in copper is about 20 MeV. It is however strongly dependent on the absorbing material and ranges from 9.5 MeV in Pb, 51 MeV in Al to 109 MeV in polystyrene [**?**]. In the energy regime of ATLAS electrons predominantly lose energy in matter by bremsstrahlung.

4.3.1 Bremsstrahlung

Bremsstrahlung is electromagnetic radiation produced by the deceleration of a charged particle. The key features of bremsstrahlung are that the electron retains its direction of propagation (in terms of η) and a fraction z of its energy with probability density f(z).

An accurate model of fractional energy remaining after bremsstrahlung is given by the Bethe-Heitler [**?**] distribution:

$$f(z) = \frac{(-\ln(z))^{c-1}}{\Gamma(c)} \qquad c = \frac{t}{\ln 2} \tag{4.2}$$

where t is the amount of material traversed in radiation lengths.

The Bethe-Heitler distribution, Figure **??**, shows that bremsstrahlung depends upon the amount of material, is singular at $z = 1$, is highly asymmetric and has a long tail at small z.

The term bremsstrahlung comes from the German for ‘breaking radiation’. When traversing a medium, the nuclear electric field (of the atomic nuclei of the medium) decelerates the electrons and the energy change appears in the form of a photon. The interaction of the electron with the nuclear electric field is necessary to satisfy energy-momentum conservation and thus allow the reaction to proceed.

The Feynman diagram for bremsstrahlung, illustrated in Figure **??** has three vertices, one for the emission of a real photon and the other two for the virtual photon exchanged with the atomic nucleus. The nucleus has charge number Z and contributes a factor Z^2 to the cross-section for the process. There is a factor α from each vertex, so the cross-section is proportional to $Z^2\alpha^3$. The

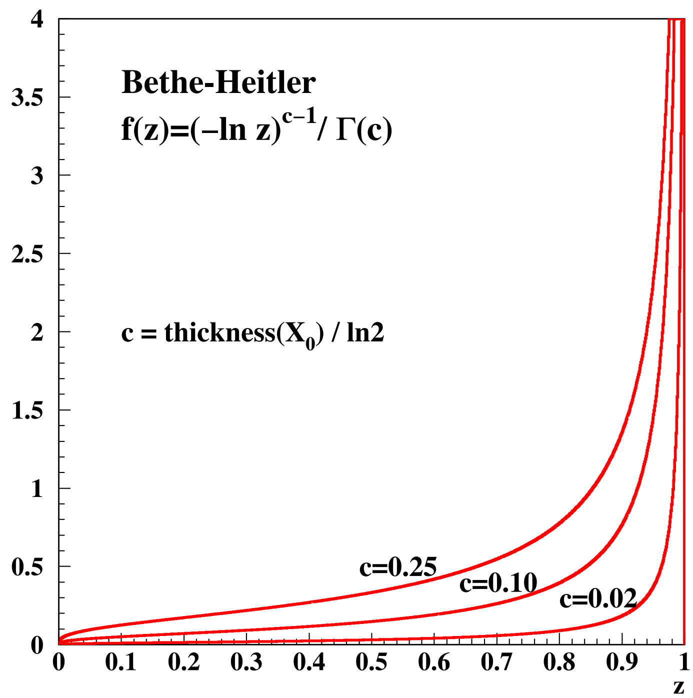

Figure 4.4: *Variation of the Bethe-Heitler distribution with material thickness, where z is the fraction of energy retained by the electron (taken from reference [*?*]). The distributions are highly asymmetric with long tails at small z.*

cross-section, σ, is

$$\sigma \propto \frac{Z^2\alpha^3}{m_e^2}$$

At high energies muons can undergo bremsstrahlung, behaving like electrons. However since a muon is 200 times heavier than an electron, its bremsstrahlung cross-section is 40 000 times smaller.

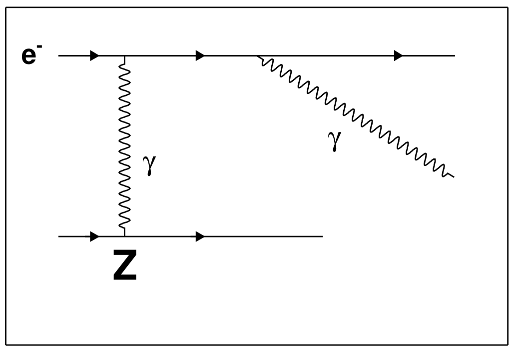

Figure 4.5: *A Feynman diagram illustrating electron bremsstrahlung in the field of a nucleus of atomic number Z.*

The process of bremsstrahlung may be visualised in the photon exchange picture. A charged particle is at all times surrounded by a cloud of virtual photons. If the particle is abruptly accelerated to one side then a photon in the cloud may become detached and carry on along the particle's path, to appear as a forward going real photon.

If a particle undergoes bremsstrahlung the track of the particle will have a smaller radius of curvature after that point. A tracking algorithm not taking bremsstrahlung into account will obtain a track fit which underestimates the particle momentum. The large amount of material in the Inner Detector implies significant bremsstrahlung will take place affecting the reconstruction of electron tracks, leading to reduced signal resolution for a wide variety of processes. Figure **??** shows the energy loss of 10 GeV and 25 GeV electrons due to bremsstrahlung within the ATLAS inner detector [**?**]. The increase in material at high $|\eta|$ in the silicon detector results in a greater average energy loss for the electrons. The fraction of energy lost is not a strong function of the electron energy.

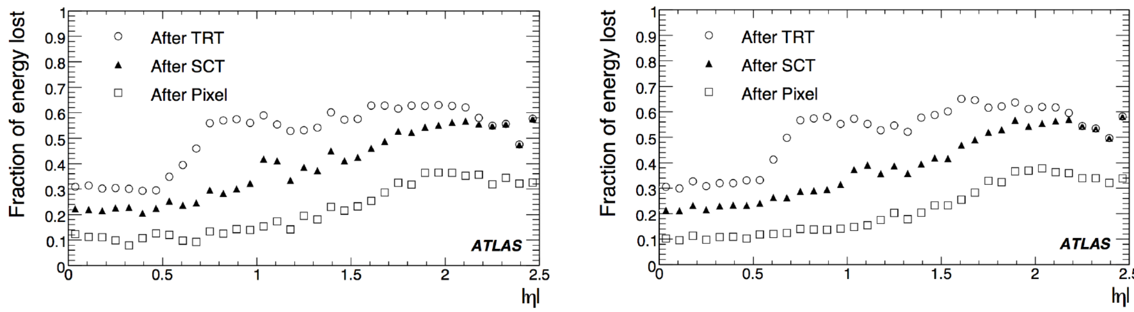

(a) P_T=10 GeV single electrons (b) P_T=25 GeV single electrons

Figure 4.6: *The average energy loss of electrons due to bremsstrahlung within the ATLAS inner detector [?]. The increase in material at high pseudorapidity in the silicon detector results in a greater average energy loss for the electrons. The fraction of energy lost is not a strong function of the electron energy.*

In some cases pion tracks behave in a similar way to bremming electrons and cause a major background for electron reconstruction algorithms. Many pions are present in jets coming from the interaction point and an average LHC event will be dominated by pions. Most of these pions do not decay in flight before they reach the muon spectrometer. However they can suffer elastic and inelastic scattering in the Inner Detector. In most cases the pion kinematics are different to electron bremsstrahlung, for example, scattering can take place in any direction.

4.4 Photon interactions in matter

The photons which are relevant to physics measurements in ATLAS will have energies in excess of 1 GeV [?]. At photon energies above 1 GeV, the interaction of the photons with the tracker will be completely dominated by e^+e^- pair production in the presence of material, otherwise known as photon conversion.

Some fraction of the photon conversions will be highly asymmetric [**?**], and either the electron or the positron may be produced with a very low energy. If this energy falls below the threshold required to produce a reconstructable track, then the converted photon will be seen to have only one track, and will be difficult to distinguish from a single electron or positron.

Overall, as many as 60% of the photons will convert into an electron-positron pair before reaching the face of the ATLAS calorimeter [**?**]. This number varies greatly with pseudorapidity. The probability is lowest in the most central region $|\eta| < 0.5$, where the amount of tracker material is at its minimum.

4.5 Units

4.5.1 Radiation length

Radiation length is the average thickness of a medium that reduces the mean energy of an electron by a factor e. It may also be considered as 7/9 of the mean free path for pair production by a high-energy photon.

Material with higher atomic number have shorter radiation length. Hence it is desirable to have high atomic number (low X_0) material in the electromagnetic calorimeter to cause bremsstrahlung or pair production, but as little material as possible in front of the calorimeter.

4.5.2 Interaction length

For strongly interacting particles the presence of the stronger nuclear interaction makes nuclear interaction length a more relevant characterisation of the material.

Nuclear interaction length is the mean path length required to reduce the energy of relativistic charged particles by the factor 1/e, or 0.368, as they pass through matter.

Materials with high atomic number have an interaction length that is a lot longer than their radiation length. See Table **??** for some examples of radiation and interaction lengths.

Element	Atomic number, Z	Radiation length, X_0 (gcm^{-2})	Interaction length, λ (gcm^{-2})
C	6	43	86
Si	14	24	106
Pb	82	6.3	193

Table 4.2: *Radiation length and interaction lengths for carbon, silicon and lead [**?**]. Materials with high atomic number have small radiation length but large interaction length.*

'..since all our measurements and observations are nothing more than approximations to the truth, the same must be true of all calculations resting upon them, and the highest aim of all computations made concerning concrete phenomena must be to approximate, as nearly as practicable, to the truth.'

C.F.Gauss

5

Tracking in ATLAS

This chapter considers track reconstruction in the ATLAS inner detector, introducing the various track fitters, their strengths and weaknesses.

5.1 Track Fitter Overview

While many high energy experiments use track fitting software that is based solely on one technique, the ATLAS offline reconstruction has a variety of track fitters available.

Two generic track fitters, that can be used as the default track fitter, are Global Chi Squared

(GXF) and Kalman Fitter (KF). GXF and KF are mathematically equivalent, yet different approaches.

The KF approach to track fitting is a progressive method in the sense that the track measurements are added to the track one at a time. GXF, however, combines all measurements into one big calculation to minimize the χ^2. KF is quick but might be steered off course by bad measurements, especially early in the fitting process. GXF is less sensitive to bad measurements, or outliers, but more costly in terms of computing, particularly for tracks containing many measurements.

One of the advantages of GXF over the KF is that it explicitly calculates the scattering angles, which can be used to study the material distributions along the tracks. On the other hand, GXF typically needs to invert much larger matrices than the KF, which makes it desirable to limit the number of track parameters. It therefore also runs slower than KF.

Two methods are used in ATLAS to account for bremsstrahlung losses in electron tracks, Gaussian Sum Filter (GSF) and Dynamic Noise Adjustment (DNA). GSF approximates the Bethe-Heitler distribution (Figure **??**) by a mixture of several Gaussians, to take into account the asymmetry and the low-energy of the distribution. DNA is a quick and efficient method during Kalman filtering that maps the Bethe-Heitler distribution onto a Gaussian distribution such that bremsstrahlung can be treated as a source of Gaussian noise.

GSF deals quite successfully with bremsstrahlung effects but takes one to two orders of magnitude longer to perform the track fit calculation than DNA. GSF is intended solely to be used on already identified electrons.

DNA can be run in three different modes. It can be run in a conservative setting, so that it minimises disturbance of non-electron tracks and can then be run as a default track fitter on all tracks, adding approximately a 10% overhead to the default KF fit. DNA can also be run aggressively on identified electrons and then has very similar performance results to GSF. DNA can also be run in an aggressive setting on all tracks to maximise performance on electrons, not having to rely on an initial reconstruction by another track fitter.

5.2 Tracking Overview

A large number of charged particles will be produced in the proton-proton collisions os the LHC, resulting in a large number of hits in the ATLAS inner detector. The track reconstruction software has to distinguish the hits from different charged particles and determine trajectories that best match the various measurements. The ATLAS inner detector combines high-resolution detectors at the inner radii with continuous tracking elements at the outer radii, all contained within the Central Solenoid.

A track can span the entire detector and have measurements on many different surfaces. Typically in the barrel region ($|\eta| \lesssim 1$), for each track the Pixel detector contributes three and the SCT fours space points. Thus high granularity is achieved around the vertex region. At larger radii typically 36 tracking points are provided by the Transition Radiation Tracker (TRT), providing measurement of the curvature of the track.

A track candidate is a of group measurements that has a high probability of being a result of a single particle. Creating a track candidate is the start of track reconstruction. The main track reconstruction strategy is ‘inside out’ and starts by finding a track candidate from the Pixel and SCT information and then extending the trajectory into the TRT to reconstruct a full inner detector track.

A track is a collection of measurements that represents the passage of a probable charged particle through the inner detector. The task of track fitting is to compute the best possible estimate of the track parameters of that track.

Any measurement will be corrupted to some degree by noise, biases and device inaccuracies. Therefore a means of extracting valuable information from a noisy signal is provided by a ‘filter’. The filter is a data processing algorithm, inherently incorporating discrete measurement samples rather than continuous inputs. Filtering deals with the analysis of (linear) dynamic systems.

Track fitting deals with the estimation of track parameters. The extrapolation of track parameters and their associated covariance matrices, to arbitrarily oriented surfaces of different types, inside a non-uniform magnetic field, is a fundamental element of any tracking software. It has to take multiple scattering and energy loss effects along the propagated trajectories into account. A good performance in respect of computing time consumption is crucial, due to hit and track multiplicity in high luminosity events and the small time window of the ATLAS high level trigger. Therefore stable and fast algorithms are required for the transport of the track parameters and their associated covariance matrices to different surfaces in the detector. These algorithms try to efficiently recreate as many particle tracks as possible whilst trying to minimise the possibility of producing fake tracks. The amount of information about the particles' paths is limited and so track reconstruction is typically an exercise of maximising information using statistical techniques.

The reconstruction of electrons is more problematic than the reconstruction of other charged tracks, since in addition to ionisation energy loss and multiple Coulomb scattering, electrons suffer from large energy losses due to bremsstrahlung. As electrons traverse the Inner Detector energy is lost. The fraction of energy lost on average by electrons as a function of $|\eta|$ is shown in Figure **??** [**?**]. Although much of the bremsstrahlung radiation will be collected by the electromagnetic calorimeter, the track in the Inner Detector can be seriously affected, resulting in a poorly reconstructed momentum or even in a failure to reconstruct the track altogether.

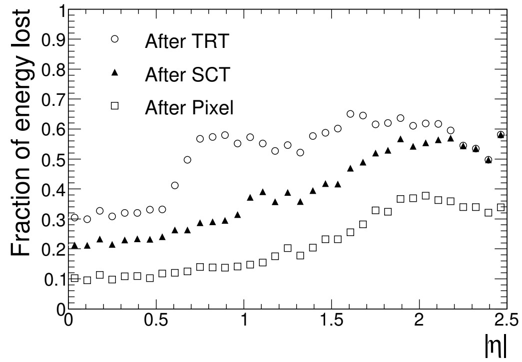

Figure 5.1: *Average fraction of energy lost by electrons with p_T=25 GeV as a function of $|\eta|$, when exiting the pixel, the SCT and the inner-detector tracking volumes [**?**].*

5.3 Tracking

5.3.1 Track Parameterisation

A track in ATLAS is parameterised at the point of closest approach, or 'perigee', to the z-axis (beam-pipe) using five perigee parameters, shown in Figure **??**:

- q/p is the charge over momentum magnitude,
- ϕ_0 is the azimuth angle of the momentum at the point of closest approach, measured in the range $(-\pi, \pi)$,
- θ_0 is the polar angle measured in the range $(0,\pi)$,
- z_0, the longitudinal impact parameter, is the z value at the point of closest approach,
- d_0, the transverse impact parameter, is the signed distance of the closest approach of the helix to the z-axis, defined to be positive when the direction of the track is clockwise with respect to the origin.

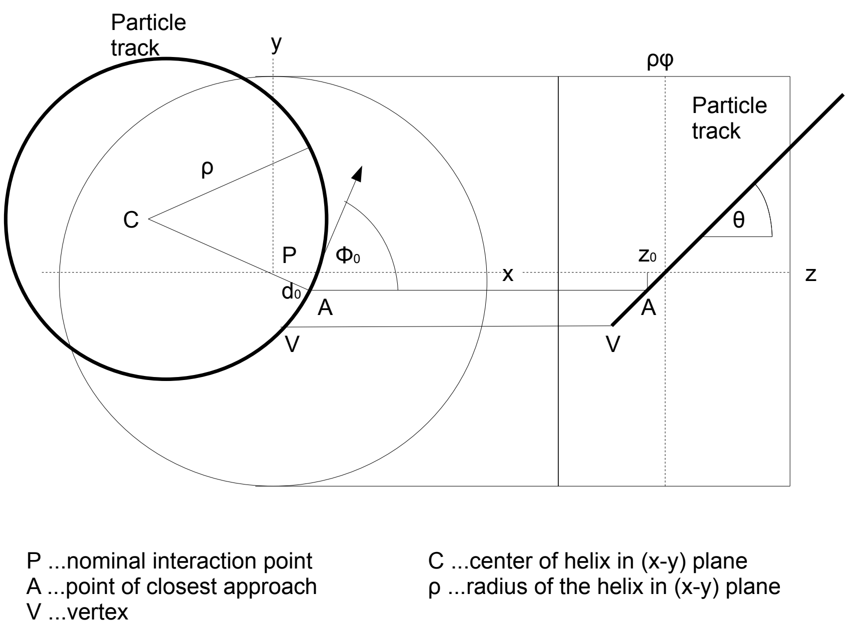

Figure 5.2: *Diagram showing the five perigee parameters, split into three transverse parameters ($x-y$ plane) and two longitudinal parameters ($r-z$ view) [**?**].*

These track parameters can then be propagated to different positions within the ATLAS detector by using the field map of the ATLAS magnetic field. Apart from the perigee parameters, a reconstructed track object can also contain a set of track parameters at various positions along the trajectory. These track parameters can be defined at any layer and can contain additional information about interactions of the particle with material in the Inner Detector.

5.3.2 Track Reconstruction

At the beginning of track reconstruction stands a pattern recognition procedure, which groups measurements belonging to a track candidate. Many track candidates are formed that do not belong to a true particle trajectory. Thus track fitting must not only provide a best estimation of track parameters but also estimate the quality of the fit.

During the past few years, a new framework for the ATLAS track reconstruction software has been developed, called New Tracking [**?**]. The aim of this framework is to make the reconstruction software more flexible and maintainable, by delegating each reconstruction step to a dedicated software module. The modules communicate through a common Event Data Model (EDM).

The Inner Detector New Tracking currently covers two sequences, the main inside-out track reconstruction and a complementary outside-in tracking.

Inside-out sequence

The main track reconstruction strategy is the 'inside-out' sequence, which starts by finding a track candidate in the pixel and SCT and then extends the trajectories of successfully fitted tracks to the TRT to reconstruct a full Inner Detector track.

Pattern recognition

The measurements in the pixel and SCT detectors form 'space points'. Each space-point represents a 3D precision point which is formed either from a cluster of silicon pixels or from the intersection of the front and back silicon strips in an SCT module. The pattern recognition starts by finding track seeds that consist of all three silicon (pixel) space-points and have p_T greater than 500 MeV. The track seeds provide sufficient directional information to associate additional silicon (SCT) hits to the track segment (see Ambiguity Solving, below). A track candidate is formed if a minimum of 7 silicon hits are obtained, out of a potential 14 hits, since not all hits are required to make a track.

Ambiguity solving

Many of the track candidates contain fake tracks or share hits with other track segments. The ambiguity solving is done by scoring the tracks in a reward/penalty schema to achieve the best track collection. In general, each hit leads to a higher score. 'Holes', where a track passes through a detector without producing a hit, lower the track score. Hits that are shared between tracks are assigned to the track with the highest score and removed from the other track.

TRT extension

If a track has survived the ambiguity solving an extension into the TRT is searched for and evaluated. The fitted silicon track parameters are used to define a road through the TRT. Any TRT measurements within 10 mm of this road are assigned to the silicon track. Again a scoring mechanism is used, with weights corresponding mainly to the distance of the hit from the trajectory prediction in an attempt to indicate the likeliness to represent the true hit.

Back-tracking

The track reconstruction sequence is complemented by an ‘outside-in’ strategy. This then starts from unassigned TRT segments and looks for matching hits in the SCT and pixels. This strategy is particularly important for electrons where a large bremsstrahlung may have occurred and the road building may have been guided in the wrong direction.

Smoothing

Full track information is updated with the average of the forward and backward track fitting values.

Estimation of track states

For a given set of measurements associated to a track candidate the track parameters on a chosen reference surface need to be estimated i.e. a so-called track fit is performed. The purpose of the track fit is to find an unbiased estimation of the true track parameters for a given set of measurements.

Outliers

Outliers are hits which are considered not to belong to the track and which could bend the fit away from the real trajectory.

Material Effects

Material interactions can be integrated in two ways; as point-like corrections to the track trajectory in detectors that have a discrete material distribution – such as the Silicon layers of the Inner Detector – or by incorporating the material interactions as continuous corrections during the propagation process itself.

Two kinds of track fitters are used:

- Global fitters using a Least Squares Method
- Local fitters using recursive filters

Both methods have optimal properties for Gaussian errors. It is easier to introduce material effects like multiple scattering into recursive fitters.

5.4 Track Fitting

5.4.1 Global Track Fitters

Global χ^2 Fitter (GXF)

The Global χ^2 Fit [**?**] obtains the best estimate for the track parameters by minimising the following χ^2 function:

$$\chi^2 = \sum_{i=1}^{N_{meas}} \frac{{\Delta_i}^2}{\sigma_i^2} + \sum_{scat} \left(\frac{\theta_{scat}^2}{\sigma_{scat}^2} + \frac{(\sin\theta_{loc})^2 \phi_{scat}^2}{\sigma_{scat}^2} \right) \tag{5.1}$$

The first sum runs over all the 'real' measurements, where Δ_i is the residual, the distance between the measured and predicted value of the hit position, and σ_i the error on the measurement.

The second sum runs over all the scattering planes in the fit i.e. the number of material layers along the track. Additional fit parameters, the scattering angles, the difference in angle between the incoming and outgoing track, ϕ_{scat} and θ_{scat}, allow for possible change of track direction.

θ_{loc} is the angle between the track and the z -axis at the scattering plane, the factor $\sin\theta_{loc}$ is needed because ϕ_{scat} is defined in the $x-y$ plane i.e. it is a projection of the actual scattering angle (ATLAS coordinate system defined in **??**).

The fit reduces the momentum of the track after traversing a material layer by an amount equal to the average energy loss corresponding to that material traversed.

The GXF approach is one of the best methods to merge the full system information, but involves the inversion of a matrix of order $N \times M$, where N is the number of fit parameters and M the number of measurements plus the number of scattering angles used. The CPU time required for such matrix inversion scales with M^2.

Currently GXF attempts to align only the silicon part of the Inner Detector however the number of fit parameters can be very large, up to around 15[1)] silicon material layers for an Inner Detector track, leading to a total of about 35 (5 parameters x 7 spacepoints) fit parameters. Fortunately, fast matrix inversion algorithms exist such that the execution speed of the track fit is still competitive. In practice, the algorithm requires about twice as much CPU time as the Kalman Fitter [**?**].

The GXF is currently the default ATLAS track fitter and as such has gained alot of experience with real data and shown itself to be robust.

5.4.2 Recursive Track Fitting

In contrast to global filters recursive fitters add the measurements successively to the track. They do not require all previous data to be kept in storage and reprocessed every time a new measurement is taken. This improves the practicality of the fitter implementation. Material effects, like energy loss, can also be easily considered in a recursive track fit.

Kalman Fitter (KF)

The Kalman filtering technique for track fitting is implemented in ATLAS, as proposed by Frühwirth et al. in 1987 [**?**]. It provides a forward filtering method, a backward smoothing and an outlier logic to improve the fit quality.

The Kalman Fitter was originally used for space-craft trajectories and hence traditionally its evolution in time is discussed. In terms of tracking, then track evolution is considered in terms of detector layers, k.

The Kalman filtering technique is a widely used method for track fitting. The optimal track

[1)] 3 pixel, 2x4 SCT plus others from SCT module overlap parameters are determined through an iterative process of stepping from one measurement to the next. At each measurement surface the local track parameters are described by the track state vector and the covariance matrix of the state vector.

The Kalman filter proceeds by performing three distinct operations, illustrated in Figure **??**;

The ATLAS track parameters are defined in section **??**. However in this explanation let us simplify the situation and represent the track parameters as y.

1. ***Filtering: The estimation of the 'present' state vector based upon all 'past' measurements.***

   The extrapolation propagates the track parameters, y_{k-1}, and the matrix of their uncertainties, C_{k-1}, to the next surface, k. $\overline{y}_k$ is then the first estimate of y at layer k.

$$\overline{y}_k = y_{k-1} \tag{5.2}$$

$$\overline{C}_k = C_{k-1} + Q_{k-1} \tag{5.3}$$

   The first estimate of the covariance matrix, $\overline{C}_k$ includes the process noise, Q_{k-1}, which includes multiple scattering and may incorporate such effects as bremsstrahlung.

   This corresponds to the state at surface 'A' in Figure **??**.

2. ***Prediction: estimation of the state vector at a 'future' time, as shown by 'prediction B' in Figure ??.***

   The Kalman gain, K, is used to weight the measurements, giving more importance to measurements with little error. For a measurement at layer k, m_k ('measurement B' in Figure **??**) and its associated variance, V_k, one has:

$$K_k = \frac{\overline{C}_k}{\overline{C}_k + V_k} \tag{5.4}$$

3. ***The estimation of the state vector at some time is based on all measurements taken up to the 'present' time. i.e. the previous measurement is 're-evaluated' with the new information.***

   The best estimate of the track parameters, y_k, is set to the first estimate plus the difference between the measured hit, m_k and first estimate, weighted with K_k:

$$y_k = \bar{y}_k + K_k(m_k - \bar{y}_k) \tag{5.5}$$

   This corresponds to 'updated track state B' in Figure **??**).

   The updated covariance matrix reflects the size of the errors after the k'th measurement is taken into account:

$$C_k = (1 - K_k)\overline{C}_k \tag{5.6}$$

This sequence is repeated for the next measurement.

Through this mechanism the filter becomes sensitive to track direction and momentum after just a few steps. These filtering steps can be executed both in the forward and in the opposite direction of the trajectory. However the Kalman filter only works well if the uncertainties, V, and process noise, Q, are Gaussian.

One fundamental drawback of the Kalman filtering technique is that the track parameters are known with optimal precision only after the last step of the fit. However the algorithm remains fast, in terms of CPU time, even in the presence of many measurements and multiple scattering, since no large matrix inversion is required.

5.4.3 Recursive bremsstrahlung-aware Track Fitting

If a particle undergoes bremsstrahlung the track of the particle will have a smaller radius of curvature after that point, as shown in Figure **??**. The distribution of momentum of electrons that

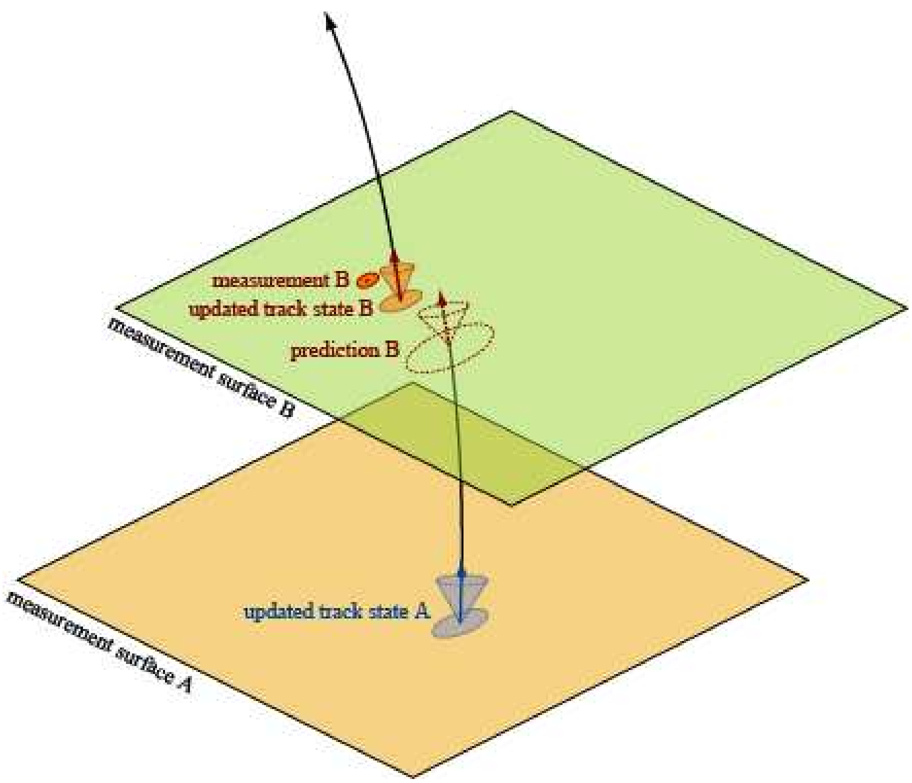

Figure 5.3: *Illustration of the Kalman Fitter process: In each filtering step the track parameters and their uncertainties are extrapolated to the next surface. The predicted position receives uncertainties from both the previous position measurement(s) and from the extrapolation uncertainty. The predicted value together with the actual measurement are used to update the track state at the next measurement surface. The algorithm iteratively repeats itself for each new measurement vector, using only values stored from the previous cycle. From [**?**].*

have undergone bremsstrahlung is far from Gaussian and the effects of bremsstrahlung at different spatial points are 100% correlated since once an electron has emitted a photon, this must be taken into account at each subsequent detector layer. A tracking algorithm not taking bremsstrahlung into account will obtain a track fit which underestimates the initial particle momentum.

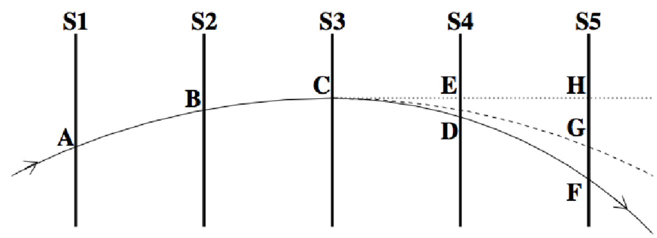

Figure 5.4: *Illustration of the path of a charged particle through detector layers $S1$ to $S5$, in a magnetic field. Point C represents the position where bremsstrahlung occurred, with point F the position of the particle at layer $S5$. Point G represents where the particle would have intersected $S5$ in the absence of bremsstrahlung and point H the position of the emitted photon.*

Bremsstrahlung recovery is extremely important in order to achieve the full range of physics goals in ATLAS. The following two track fitters are bremsstrahlung-aware.

Gaussian Sum Fitter (GSF)

The Gaussian Sum Filter is a non-linear generalisation of the Kalman Filter. It requires that all probability density functions (PDFs) be described by Gaussian mixtures [?]. In the BetheHeitler model, the PDF, f(z), of the energy loss is very non-Gaussian. If the energy loss due to bremsstrahlung is estimated by a single Gaussian it is quite a crude approximation. Estimating the Bethe-Heitler distribution with a weighted sum of Gaussians can prove to be quite accurate given enough Gaussians. It is this estimate that is used in the GSF to estimate energy loss at each material surface, as shown in Figure **??**.

However CPU time increases dramatically with increasing number of components. Several

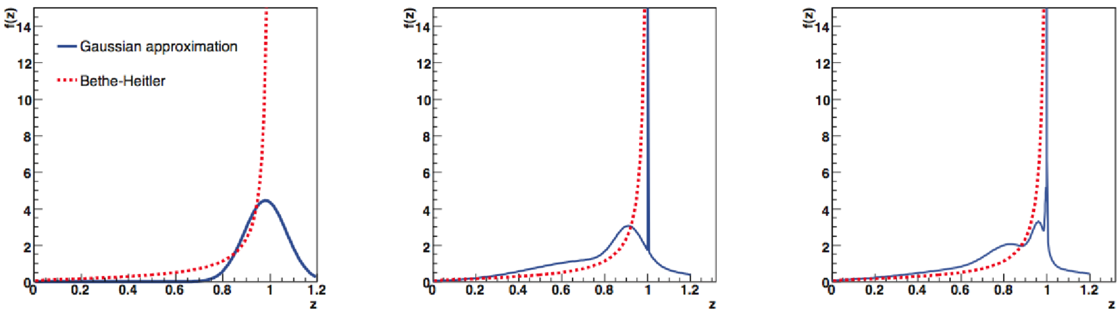

(a) $N_{Gaussians} = 1$ (b) $N_{Gaussians} = 3$ (c) $N_{Gaussians} = 6$

Figure 5.5: *The GSF models the Bethe-Heitler distribution by a weighted sum of Gaussian distributions, to take into account the asymmetry and low-energy tail. The Bethe-Heitler PDF is shown in red (dashed). The sum of the number of Gaussian mixtures is shown in blue (solid). From [*?*].*

Kalman filters run in parallel and despite algorithmic techniques to reduce complexity of the calculations, GSF has the major disadvantage that it takes one to two orders of magnitude longer to perform the track fit calculation than the Kalman Fitter. GSF does however deal quite successfully with bremsstrahlung effects.

Dynamic Noise Adjustment (DNA)

A quick and efficient method of dealing with electron tracks has been developed and implemented by Lancaster ATLAS group. It is based on Dynamic Noise Adjustment (DNA) during Kalman filtering.

The Kalman filtering technique is efficient, but to be optimal, relies on process noise and measurement noise being Gaussian in distribution and independent of each hit. Measurement noise can be considered Gaussian and independent at each detector layer. DNA looks at ways of improving electron tracking by estimating the fraction of energy retained by the electron and then dynamically calculating an effective noise variance.

At each silicon layer, a simple single-parameter fit is performed to flag hits which may be associated with bremsstrahlung. This fit tries to estimate the increase in curvature due to possible bremsstrahlung at the current detector layer. If no bremsstrahlung was flagged, the track fitter reverts to the default Kalman filtering procedure. Otherwise, the result of the single parameter fit — the estimated fraction of energy retained by the electron, z — is used to calculate the additional effective 'system noise' term, which is then fed to the Kalman Filter.

The effective 'system noise' variance calculation is illustrated by Figure **??**, which shows how the Bethe-Heitler distribution is mapped onto the Gaussian distribution of unit width. The deviation Δz of the estimated z from the median z_0 of the Bethe-Heitler distribution is mapped onto the Gaussian distribution to find the corresponding deviation Δx.

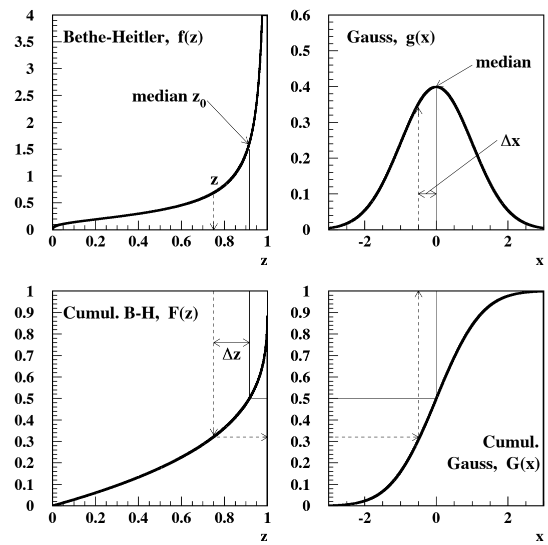

Figure 5.6: *Mapping of the Bethe-Heitler distribution onto a Gaussian distribution to calculate the effective system-noise variance in the Kalman DNA approach [**?**]. Starting at the top left distribution of the Bethe-Heitler, z, the estimated amount of energy retained by the electron is seen. This is mapped onto the bottom left distribution of the cumulative Bethe-Heitler, where Δz, the estimated difference from the median value, is shown. Moving across to the bottom right distribution of the cumulative Gaussian, and up to the Gassian distribution of unit width (top right), the value of the corresponding deviation from the Gaussian median value,Δx, can be extracted.*

The effective noise σ is then calculated as $\sigma_{DNA}(z) = \Delta z/\Delta x$. This procedure is equivalent to representing the random variable z, distributed according to the Bethe-Heitler probability density, in the form

$$z = z_0 + x\sigma_{DNA}(z)$$

where x is a random variable with Gaussian probability distribution. In this approach bremsstrahlung is legitimately treated as a source of Gaussian noise, but only in those cases when bremsstrahlung-like behaviour of the track has been detected. The proper Gaussian probability distribution of this 'system noise' is now guaranteed by construction [**?**]. Clearly σ_{DNA} also depends on the thickness of material associated with the corresponding layer, as illustrated by Figure **??**.

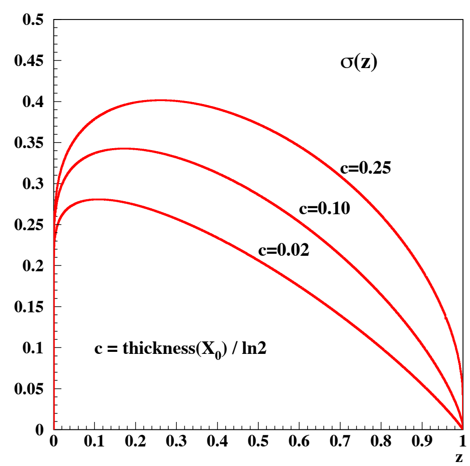

Figure 5.7: *Effective noise $\sigma_{DNA}(z)$ for various values of material thickness in the detector layer [**?**].*

The variance σ^2_{DNA} is added to the appropriate term of the Kalman covariance matrix used during the fit, consistent with the treatment of any other source of system noise. This particular noise term is adjusted dynamically according to the estimated z and the thickness of the layer, thus justifying the name of the method.

DNA Separator

If all tracks are treated as if they are electrons, then the momentum reconstruction of non-electrons is skewed to higher momentum to take into account bremsstrahlung that has not happened i.e. a reduction of momentum is noticed by the fitter that is just a fluctuation.

'DNA Separator' is a tool which permits two tunings of DNA. The first, conservative, leaves the vast majority of non-electron tracks intact. Only when a sustained momentum reduction is noticed along the track does DNA kick in. The second, aggressive, is to be used on already identified electron tracks and reacts to any momentum reduction.

Pions sometimes behave like bremming electrons and create a background for bremsstrahlung recovery. Table **??** shows that conservative DNA has good electron-pion rejection, reacting to 21% of 10 GeV electrons but only 1% of 10 GeV pions. Performance on 2 GeV electrons and pions is similar. Aggressive DNA reacts to about 70% of electrons, but should only be applied to identified electrons as electron-pion rejection is poor. The electron-pion rejection factor in the barrel is very similar to the figure over the whole η range. The actual percentage shown for the barrel is around one third of the total value, which is reasonable since the barrel η range was defined as $|\eta| < 0.8$, a third of the total range.

5.5 Summary

The ATLAS reconstruction mainly uses two mathematically equivalent, yet different approaches to track refitting, implemented as the Global χ^2 track fitter (GXF) and Kalman fitter (KF).

The KF approach to track fitting is a progressive method in the sense that the track measurements are added to the track one at a time. Mathematically, the KF performs a χ^2 minimization, equivalent to the GXF. GXF, however, combines all measurements into one big calculation to minimize the χ^2. Both methods have their strengths and weaknesses. KF is quick but might be steered

Particle	p_T	DNA tuning	Total (%)	Barrel (%)
Electron	10 GeV	Conservative	21	6
Pion	10 GeV	Conservative	1	0.3
Electron	2 GeV	Conservative	18	5
Pion	2 GeV	Conservative	1	0.4
Electron	2 GeV	Aggressive	69	23
Pion	2 GeV	Aggressive	64	21

Table 5.1: *Electron-Pion Rejection: Percentage of events where DNA reacts in full η range (Total) and in barrel where $|\eta| < 0.8$. Pions often behave like breming electrons. DNA should react to electron behaviour but have minimal impact on pions for best performance. Conservative tuning shows DNA is activated for a good percentage of electrons with a small pion background. Aggressive tuning reacts on a large percentage of electrons and pions and so should be only used for identified electrons.*

off course by bad measurements, especially early in the fitting process. GXF is less sensitive to bad measurements, or outliers, but more costly in terms of computing, particularly for tracks containing many measurements.

Tracking tools, common to all fitters, are used to provide extrapolation, material and magnetic field updates as well as calibration corrections and thus maintain fitter independence of detector-specific conditions. However, GXF handles the material interactions in the final track fit, whereas KF incorporates the material interactions at points along the track or continuously during the track propagation.

One of the advantages of GXF over the KF is that it can provide the scattering angles, which can be used to study the material distributions along the tracks. On the other hand, GXF typically needs to invert much larger matrices than the KF, which makes it desirable to limit the number of track parameters.

In general, electrons lose a significant amount of energy due to bremsstrahlung and thus the Gaussian assumption of the noise added to the track fit due to material interactions is far from being optimal. Dedicated fitting techniques, such as the Gaussian Sum Filter (GSF) or the Dynamic

Noise Adjustment (DNA) have been developed to enhance a better performance, either through a multicomponent model or modified error description, respectively.

GSF deals quite successfully with bremsstrahlung effects but takes one to two orders of magnitude longer to perform the track fit calculation than the KF. GSF is intended solely to be used on already identified electrons.

The DNA algorithm employs a method based on the underlying physical process and is fast enough to be used for online correction of tracks during the initial track reconstruction, adding approximately a 10% overhead to the default fit when the DNA algorithm is employed. DNA can also be run aggressively on identified electrons and then has very similar performance results to GSF.

'The electron is not as simple as it looks.'

William Lawrence Bragg

6
ATLAS track fitter comparisons

In this chapter I show a comparison of the different fitters implemented in ATLAS inner detector software as Athena releases progress and the fitters themselves evolve and change. Initially fitter comparisons are made using single particle Monte Carlo data and then a more realistic Monte Carlo data sample is used, of electrons from prompt J/ψ.

6.0.1 Criteria

There are no clear criteria for comparing ATLAS track fitters, since this is the first comparison study to take place between the different track fitters. The key factors selected are

- good momentum reconstruction.
- continuous tracking through the Inner Detector from silicon and into the TRT.

A compromise is sought between these two criteria, since if too tight a restriction is put on the quality of the momentum reconstruction, then the probability of loosing the TRT track extension is increased.

When working with samples of fixed numbers of generated tracks, the total number of tracks reconstructed is an indication of the tracking performance. Clearly the closer the p_T is reconstructed to the true value, the better the job the fitter is doing.

Looking at the distributions of the ratio of generated to reconstructed charge over momentum (Figure **??**), there is a characteristic tail for electrons, due to bremsstrahlung. If a track fitter is used for both electron and non-electron tracks, these tails should be reduced for electrons without over-compensating non-electron tracks. Pion and muon track reconstruction is therefore monitored using the generic track fitters. If, however, the fitter is applied only to previously identified electrons, its effects on non-electron tracks do not matter.

The ratio of generated to reconstructed charge over momentum is essentially, for electrons, the ratio of reconstructed to generated track momentum and so simultaneously indicates accurate momentum reconstruction and efficient bremsstrahlung recovery. The number of tracks with reconstructed momentum within 50, 20 and 10% respectively of the generated momentum value are used as a performance indicator and is noted in the tables below.

Traversing the Inner Detector a particle travels 40 mm from the fourth, outer, SCT layer, before it reaches the TRT. This is a difficult region for a track fitter, since if an electron undergoes bremsstrahlung close to the outer section of the SCT, then it is difficult for the track to be picked up again when it reaches the TRT. Hence the number of tracks without TRT extensions is considered, labeled 'Si only'. Clearly this should be minimised.

6.0.2 Fitter Comparisons using single particles.

Athena Release 15.0.0

The Monte Carlo data samples used for comparing the track fitters consisted of single electrons at 1 GeV, 5 GeV and 100 GeV along with 5 GeV single pions. A standard sample of 2,500 events was used. Despite this being a relatively small number, since the same tracks are being compared, this was considered a sufficient number to give a good indication of the fitter performances. Bremsstrahlung is known to have more impact on low p_T electron reconstruction than high p_T ones, so 5 GeV electrons were used to compare the performance of the three generic fitters, GXF, KF, DNA (DNA with conservative setting) and also the two electron specific fitters, GSF and AggDNA (DNA with aggressive settings).

The full η range has been divided into three, enabling a comparison in performance between the three physically different detector regions: barrel $|\eta| < 0.8$, transition $0.8 < |\eta| < 1.6$ and endcaps $1.6 < |\eta| < 2.4$.

Figure **??** and Figure **??** shows the distributions of the ratio of generated to reconstructed charge over momentum, for 5 GeV electrons and pions. The distributions are shown for the barrel, transition and endcap regions for the three generic fitters. The characteristic tail in electron momentum reconstruction is clearly seen. A track fitter aims to reduce this tail without over-compensating in momentum or affecting pion reconstruction. Figure **??** shows the pull distributions for 5 GeV electrons in the barrel region. Table **??** summarises fitter performance on pions, showing that all default fitters have similar performance.

Table **??** shows the total number of 5 GeV electron tracks reconstructed, number of tracks reconstructed within 50, 20 and 10% of the generated momentum value and the number of tracks without TRT extensions, for the five different fiters. All three generic fitters are performing well, with similar numbers of tracks reconstructed. GXF and DNA perform slightly better than KF at TRT extensions, with silicon-only numbers reduced. GSF has the least number of silicon-only tracks in all three η ranges and maximum number of tracks with reconstructed momentum within 10% of generated values. However, the high performance of the GSF comes at the expense of time and momentum measurement biased towards higher values.

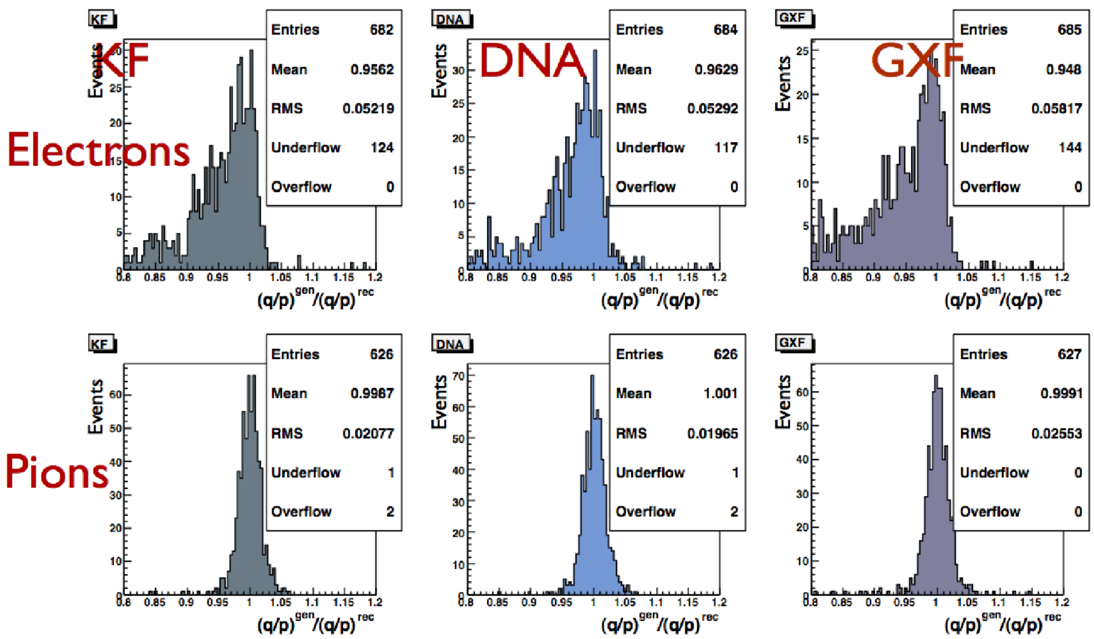

(a) Barrel region: $|\eta| < 0.8$

Figure 6.1: *The distributions of the ratio of reconstructed to generated charge over momentum are shown for 5 GeV electrons and pions in the barrel region, for the three generic fitters; Kalman Fitter (KF), Kalman Fitter Dynamic Noise Adjustment (DNA) and Global χ^2 (GXF).*

Table **??** summarises the performance of the generic fitters on 1 GeV electrons. In the barrel region GXF has the smallest number of tracks without TRT extensions and DNA has the largest

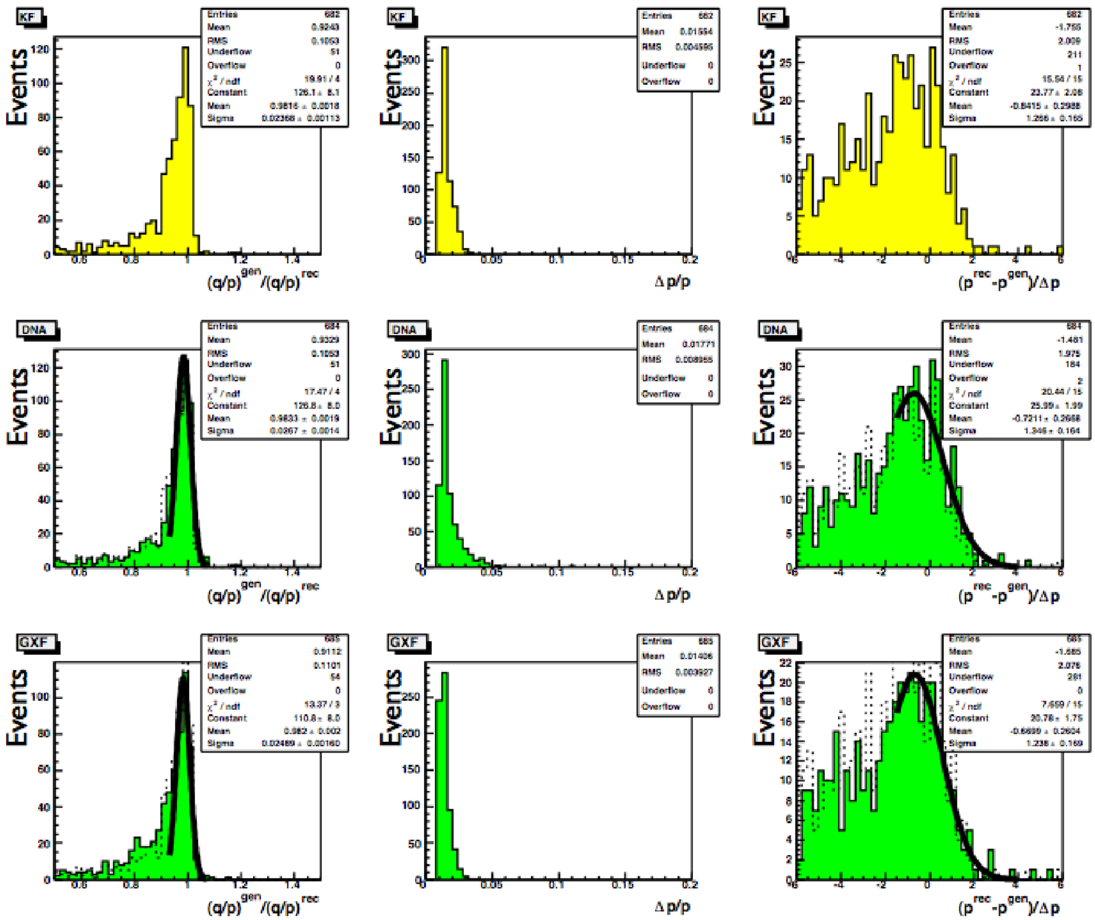

(a) Barrel region: $|\eta| < 0.8$

Figure 6.2: *The pull distributions are shown for 5 GeV electrons in the barrel region, for the three generic fitters; Kalman Fitter (KF), Kalman Fitter Dynamic Noise Adjustment (DNA) and Global χ^2 (GXF).*

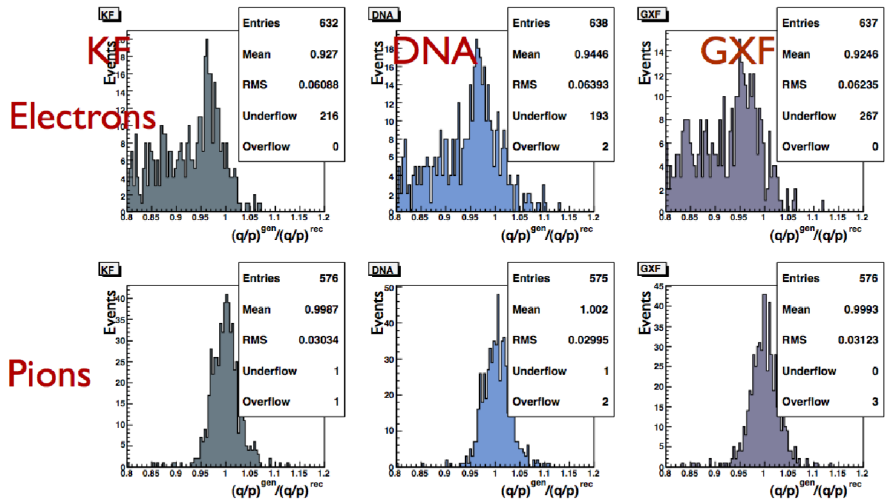

(a) Endcap regions: $0.8 < |\eta| < 1.6$

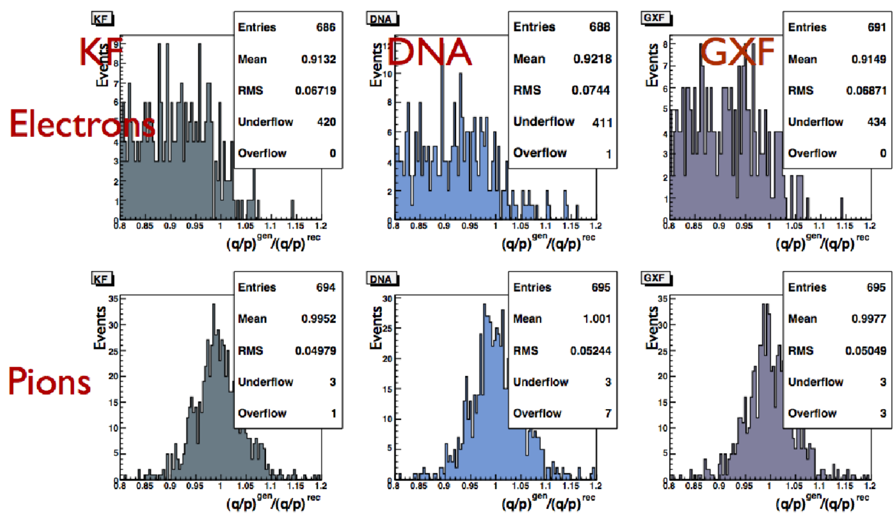

(b) Endcap regions: $1.6 < |\eta| < 2.4$

Figure 6.3: *The distributions of the ratio of reconstructed to generated charge over momentum are shown for 5 GeV electrons and pions in the transition and endcap regions, for the three generic fitters; Kalman Fitter (KF), Kalman Fitter Dynamic Noise Adjustment (DNA) and Global χ^2 (GXF).*

η Range	Fitter	Total	Within 50%	Within 20%	Within 10%	Si only
Barrel	GXF	99.4 ±3.8	91.6 ±3.7	78.5 ±3.4	62.8 ±3.0	16.3 ±1.5
$\lvert\eta\rvert$ <0.8	KF	99.0 ±3.8	91.6 ±3.7	81.0 ±3.4	70.3 ±3.2	21.9 ±1.8
	DNA	99.3 ±3.8	91.9 ±3.7	82.3 ±3.5	72.1 ±3.2	15.2 ±1.5
	AggDNA	99.3 ±3.8	91.9 ±3.7	83.5 ±3.5	74.6 ±3.3	11.5 ±1.3
	GSF	99.7 ±3.8	92.5 ±3.7	84.5 ±3.5	77.1 ±3.3	6.1 ±0.9
Transition	GXF	98.6 ±3.9	84.2 ±3.6	57.3 ±3.0	52.5 ±2.9	27.4 ±2.1
0.8< $\lvert\eta\rvert$ <1.6	KF	97.8 ±3.9	84.7 ±3.6	64.4 ±3.2	43.0 ±2.6	33.9 ±2.3
	DNA	98.8 ±3.9	86.1 ±3.7	68.6 ±3.3	51.1 ±2.8	23.5 ±1.9
	AggDNA	98.8 ±3.9	87.2 ±3.7	72.3 ±3.4	56.7 ±3.0	22.5 ±1.9
	GSF	98.5 ±3.9	88.7 ±3.7	75.9 ±3.4	61.0 ±3.1	10.1 ±1.3
Endcaps	GXF	88.9 ±3.4	61.5 ±2.8	33.1 ±2.1	18.4 ±1.5	55.6 ±2.7
$\lvert\eta\rvert$ >1.6	KF	88.3 ±3.4	62.2 ±2.8	34.2 ±2.1	18.9 ±1.6	58.9 ±2.8
	DNA	88.6 ±3.4	62.9 ±2.9	35.5 ±2.1	19.8 ±1.6	56.8 ±2.7
	AggDNA	88.6 ±3.4	65.3 ±2.9	39.8 ±2.3	23.6 ±1.7	55.6 ±2.7
	GSF	89.3 ±3.4	70.1 ±3.0	49.7 ±2.5	31.2 ±2.0	52.8 ±2.6

Table 6.1: *5 GeV electrons. The table shows the percentage of tracks reconstructed with respect to truth, percentage of tracks reconstructed within 50, 20 and 10% of the generated momentum value, plus the percentage of tracks without TRT extensions (Si only). All three generic fitters are performing well, with similar numbers of tracks reconstructed. GXF and DNA perform slightly better than KF at TRT extensions, with 'Si only' numbers reduced. GSF has the least number of 'Si only' tracks in all three η ranges and the maximum number of tracks with reconstructed momentum within 10% of generated values. However, the high performance of GSF comes at the expense of time. See Figure* **??** *for distributions in barrel and Figure* **??** *for transition and endcap regions for the three generic fitters.*

η Range	Fitter	Total	Within 50%	Within 20%	Within 10%	Si only
Barrel	GXF	95.6 ±3.8	95.6 ±3.8	95.6 ±3.8	94.4 ±3.8	4.4 ±0.8
$\|\eta\|$ <0.8	KF	95.4 ±3.8	95.3 ±3.8	95.0 ±3.8	94.5 ±3.8	5.8 ±0.9
	DNA	95.4 ±3.8	95.3 ±3.8	95.0 ±3.8	94.7 ±3.8	5.3 ±0.9
Transition	GXF	91.7 ±3.8	91.7 ±3.8	91.2 ±3.8	89.8 ±3.8	7.0 ±1.1
0.8< $\|\eta\|$ <1.6	KF	91.7 ±3.8	91.7 ±3.8	91.4 ±3.8	90.1 ±3.8	7.5 ±1.1
	DNA	91.6 ±3.8	91.6 ±3.8	91.1 ±3.8	90.5 ±3.8	7.5 ±1.1
Endcaps	GXF	92.2 ±3.5	91.9 ±3.5	91.4 ±3.5	86.3 ±3.4	49.1 ±2.6
1.6< $\|\eta\|$ <2.4	KF	92.0 ±3.5	91.8 ±3.5	91.5 ±3.5	87.1 ±3.4	48.9 ±2.6
	DNA	92.2 ±3.5	91.6 ±3.5	90.9 ±3.5	85.9 ±3.4	48.8 ±2.5

Table 6.2: *5 GeV pions. The table shows the total percentage of tracks reconstructed, percentage of tracks reconstructed within 50, 20 and 10% of the generated momentum value and the percentage of tracks without TRT extensions (Si only). In some cases pions behave in a similar way to bremming electrons. From the electron reconstruction point of view this is of course background or noise. All default fitters show similar performance on pions.*

number of tracks within 10% in the barrel. In the transition region DNA has the most tracks within 10% and the least number of tracks without TRT extensions. In the endcaps GXF and DNA are performing equally well at TRT extensions with DNA having the most tracks within 10%.

Even at 100 GeV a bremsstrahlung-aware fitter makes a difference. In barrel and transition regions DNA has the most tracks within 10% and the least number of tracks without TRT extensions, compared with the other two generic fitters. See Table **??**.

η Range	Fitter	Total	Within 50%	Within 20%	Within 10%	Si only
Barrel	GXF	99.7 ±4.0	99.7 ±4.0	82.1 ±3.6	65.8 ±3.2	19.2 ±1.8
$\lvert\eta\rvert$ <0.8	KF	98.6 ±4.0	98.6 ±4.0	84.0 ±3.7	68.7 ±3.3	24.0 ±2.0
	DNA	98.6 ±4.0	98.6 ±4.0	84.8 ±3.7	71.7 ±3.4	19.5 ±1.8
Transition	GXF	99.6 ±4.3	99.5 ±4.3	77.6 ±3.8	50.9 ±3.1	39.3 ±2.7
0.8< $\lvert\eta\rvert$ <1.6	KF	98.7 ±4.3	98.5 ±4.3	80.2 ±3.8	57.9 ±3.3	46.0 ±2.9
	DNA	99.5 ±4.3	99.3 ±4.3	83.8 ±3.9	65.3 ±3.5	38.1 ±2.6
Endcaps	GXF	98.3 ±4.5	97.7 ±4.5	51.9 ±3.3	28.9 ±2.4	67.8 ±3.7
1.6< $\lvert\eta\rvert$ <2.4	KF	96.9 ±4.5	96.7 ±4.5	53.5 ±3.3	28.7 ±2.4	69.4 ±3.8
	DNA	98.1 ±4.5	98.1 ±4.5	56.4 ±3.4	32.0 ±2.6	68.0 ±3.8

Table 6.3: *1 GeV electrons. The table shows the total percentage of tracks reconstructed, percentage of tracks reconstructed within 50, 20 and 10% of the generated momentum value and the percentage of tracks without TRT extensions (Si only). In the barrel region GXF has the smallest number of tracks without TRT extensions and DNA has the largest number of tracks within 10% in barrel. In the transition region DNA has the most tracks within 10% and the least number of tracks without TRT extensions. In the endcaps GXF and DNA are performing equally well at TRT extensions with DNA having the most tracks within 10%.*

η Range	Fitter	Total	Within 50%	Within 20%	Within 10%	Si only
Barrel	GXF	97.0 ±3.7	83.8 ±3.5	60.8 ±3.0	46.1 ±2.6	7.2 ±1.0
$\lvert\eta\rvert$ <0.8	KF	97.3 ±3.7	86.8 ±3.5	63.5 ±3.0	46.7 ±2.6	6.9 ±1.0
	DNA	97.6 ±3.7	87.8 ±3.6	66.5 ±3.1	49.3 ±2.7	6.2 ±0.9
Transition	GXF	93.3 ±3.6	69.5 ±3.1	41.5 ±2.4	26.4 ±1.9	14.3 ±1.4
0.8< $\lvert\eta\rvert$ <1.6	KF	92.6 ±3.6	72.4 ±3.2	43.4 ±2.4	27.2 ±1.9	13.9 ±1.4
	DNA	92.6 ±3.6	73.4 ±3.2	48.8 ±2.6	30.5 ±2.0	11.8 ±1.3
Endcaps	GXF	93.5 ±3.2	58.0 ±2.5	28.6 ±1.8	14.2 ±1.3	62.3 ±2.6
1.6< $\lvert\eta\rvert$ <2.4	KF	93.5 ±3.2	58.5 ±2.5	28.5 ±1.8	15.2 ±1.3	62.2 ±2.6
	DNA	93.2 ±3.2	58.4 ±2.5	29.3 ±1.8	15.1 ±1.3	61.2 ±2.6

Table 6.4: *100 GeV electrons. The table shows the total percentage of tracks reconstructed compared with truth, percentage of tracks reconstructed within 50, 20 and 10% of the generated momentum value and the percentage of tracks without TRT extensions (Si only). Even at 100 GeV generic DNA still shows an improvement. In barrel and transition regions DNA has the most tracks within 10% and the least number of tracks without TRT extensions. In the endcaps KF and DNA perform well.*

Fitter Evolution

To show the evolution of the different fitters though Athena release 14.0 to 15.0 (a time span of $\sim$1 year), numbers are shown using 10k events of 2 GeV single electrons.

The performance of the three generic fitters is summarised in Table **??** for barrel and in Table **??** for the endcap regions. All fitters show an improvement in TRT extensions, but perhaps at the expense of momentum resolution. GXF performance in Athena release 14.2. illustrates the correlation between momentum resolution and TRT extensions, with a big improvement in the number of tracks within 10% alongside a deterioration in TRT extensions.

Fitter	Release	Total	Within 50%	Within 20%	Within 10%	Si only
KF	15.0	97.8 ±2.0	93.0 ±1.9	81.1 ±1.8	67.4 ±1.7	23.0 ±1.0
	14.2	99.1 ±2.0	94.9 ±2.0	81.7 ±1.8	68.2 ±1.7	26.0 ±1.0
	14.1	99.3 ±2.0	95.0 ±2.0	81.8 ±1.8	68.3 ±1.7	26.9 ±1.0
	14.0	97.9 ±2.0	94.0 ±2.0	81.1 ±1.8	68.4 ±1.7	27.9 ±1.1
DNA	15.0	98.5 ±2.0	94.0 ±2.0	82.3 ±1.8	70.8 ±1.7	16.5 ±0.8
	14.2	99.4 ±2.0	95.5 ±2.0	83.6 ±1.8	73.4 ±1.7	18.1 ±0.9
	14.1	99.6 ±2.0	95.8 ±2.0	83.8 ±1.8	74.2 ±1.7	16.9 ±0.8
	14.0	98.7 ±2.0	95.1 ±2.0	82.8 ±1.8	73.4 ±1.7	15.5 ±0.8
GXF	15.0	98.9 ±2.0	93.9 ±2.0	79.3 ±1.8	61.0 ±1.6	16.6 ±0.8
	14.2	100.0 ±2.0	95.7 ±2.0	82.1 ±1.8	72.1 ±1.7	40.2 ±1.3
	14.1	99.7 ±2.0	95.4 ±2.0	78.8 ±1.8	57.9 ±1.5	14.3 ±0.8
	14.0	99.9 ±2.0	95.4 ±2.0	80.1 ±1.8	62.1 ±1.6	19.1 ±0.9

Table 6.5: *Fitter Evolution: 2 GeV electrons in barrel, $|\eta| < 0.8$. The table shows the total percentage of tracks reconstructed, percentage of tracks reconstructed within 50, 20 and 10% of generated momentum value and percentage of tracks without TRT extensions (Si only) for the different software releases. All generic fitters show an improvement in TRT extensions, but perhaps at the expense of momentum resolution. GXF performance in 14.2. illustrates the correlation between momentum resolution and TRT extensions, with a big improvement in the number of tracks within 10% alongside a deterioration in TRT extensions, seen as a large increase in Si only tracks.*

Fitter	Release	Total	Within 50%	Within 20%	Within 10%	Si only
KF	15.0	91.1 ±1.8	74.7 ±1.7	39.4 ±1.2	22.5 ±0.9	60.0 ±1.5
	14.2	93.7 ±1.9	75.1 ±1.7	40.8 ±1.2	23.0 ±0.9	62.1 ±1.5
	14.1	94.3 ±1.9	75.0 ±1.7	41.0 ±1.2	23.0 ±0.9	63.0 ±1.5
	14.0	92.9 ±1.9	74.7 ±1.7	41.3 ±1.2	23.6 ±0.9	62.3 ±1.5
DNA	15.0	92.0 ±1.9	76.2 ±1.7	41.9 ±1.3	23.8 ±0.9	58.0 ±1.5
	14.2	94.2 ±1.9	76.8 ±1.7	43.9 ±1.3	25.4 ±1.0	60.5 ±1.5
	14.1	94.6 ±1.9	77.1 ±1.7	44.9 ±1.3	25.7 ±1.0	61.4 ±1.5
	14.0	93.6 ±1.9	76.4 ±1.7	44.2 ±1.3	25.7 ±1.0	60.8 ±1.5
GXF	15.0	92.5 ±1.9	75.2 ±1.7	38.6 ±1.2	21.3 ±0.9	57.7 ±1.5
	14.2	90.7 ±1.8	83.8 ±1.8	65.0 ±1.6	50.8 ±1.4	53.9 ±1.4
	14.1	93.9 ±1.9	74.3 ±1.7	38.8 ±1.2	21.6 ±0.9	58.4 ±1.5
	14.0	94.2 ±1.9	74.5 ±1.7	39.6 ±1.2	22.6 ±0.9	60.6 ±1.5

Table 6.6: *Fitter Evolution. 2 GeV electrons in endcaps:* $1.6 < |\eta| < 2.4$. *The table shows the percentage of tracks reconstructed compared with truth, percentage of tracks reconstructed within 50, 20 and 10% of generated momentum value and percentage of tracks without TRT extensions (Si only) for the different software releases. All generic fitters show an improvement in TRT extensions. GXF performance in 14.2 shows similar improvement in momentum resolution as seen in the barrel, but without the marked decrease in TRT extension performance.*

6.0.3 Fitter Comparisons using electrons from prompt J/ψ

In preparation for early data it seems necessary to find a method of fitter comparison that can be used to assess performance during data-taking. Low energy resonances, such as J/ψ, will be one of the main sources of isolated electrons in the early data. J/ψ signal samples are therefore ideal to study the performances of offline reconstruction at low energies. Using electrons from J/ψ allows us to compare fitter performance, by considering the well understood and measured J/ψ mass peak at 3.097 GeV as our standard candle. Likewise, L_{xy}, the transverse distance from the primary vertex (Figure **??**), can also be used as a key indicator since L_{xy} for prompt J/ψ is zero and any deviation from this is a measurement of resolution.

In this section I show a comparison of the performance of the three generic fitters and two electron-specific fitters on electrons from prompt J/ψ, with the Inner Detector divided into just two η regions, $|\eta| < 1$ and $|\eta| > 1$.

The generic Global χ^2 (GXF), Kalman Fitter (KF) and Kalman DNA Fitter (DNA) as well as the electron-specific Aggressive DNA (AggDNA) were used to reconstruct AODs from RDOs. The egamma Refit tool was used to re-reconstruct from AODs (initial reconstruction with GXF) using the electron-specific Gaussian Sum Fitter (GSF) and AggDNA. To try to clarify the mode in which AggDNA was being used I will refer to 'AggDNA full fit', when reconstruction was carried out on RDOs, and 'refit AggDNA' when a refit was carried out on AODs.

The RDO sample used was prompt J/ψ decay into two electrons each with transverse momentum of at least 3 GeV. Reconstruction was carried out with each of the track fitters. Combinations were made between oppositely charged electron candidates. Events were selected where there was at least 1 J/ψ candidate, in a mass window between 1.5 and 4.0 GeV with electron candidates coming from a common vertex. The AODs were produced by running on the grid. One of the many wonders of the grid is that not all subjobs complete. From the 200k events advertised I managed to collect back 178k events that were common to all six fitters. I therefore have reasonably large statistics plus the added advantage of being able to make fine comparisons between the same events.

Electron Track Pt

The ability of a fitter to reconstruct accurately the p_T of a track must be a high priority. Figure **??** shows the electron track p_T from J/ψ candidates with the different fitters. The fill colour in the p_T distributions shows when both electrons have satisfied the electron quality criteria (Table **??**) and numbers are shown in Table **??**. There appears to be a marked jump between the number of J/ψ candidates where both electrons are required to pass the Medium and Tight requirements [1)]. DNA performs extremely well at numbers of reconstructed electrons up to Medium electron quality criteria. GXF and refit AggDNA reconstruct the most electrons which pass Tight electron quality criteria. The generated sample requires the electrons to have p_T greater than 3 GeV. The distribution tails at low p_T are poorly reconstructed electrons. As the electron quality criteria are tightened, then these tails disappear. The tails are much less pronounced for the refit GSF and refit Aggressive DNA, since these fitters are only working on already identified electrons.

One would expect that a bremsstrahlung-aware fitter would reconstruct more electron tracks and would also do so more accurately. Table **??** shows that indeed the percentage of J/ψ candidates reconstructed is improved. It is however only a very small increase. The refitters can push up p_T to take into consideration the losses from bremsstrahlung, but they cannot recover new tracks, by definition.

Instead of comparing fitter performance with truth, the reconstructed electron p_T distributions for each fitter are divided by the p_T distribution for the default track fitter, GXF. Figure **??** shows the electron track p_T for each fitter wrt GXF electron track p_T. There appears to be a curious turning point at 5.5 GeV, in both η ranges, where all the fitters follow a similar pattern of reconstructing

[1)] Indeed the criteria have since been optimised and modified for Athena 15.5.X (releases since 15.5.0)

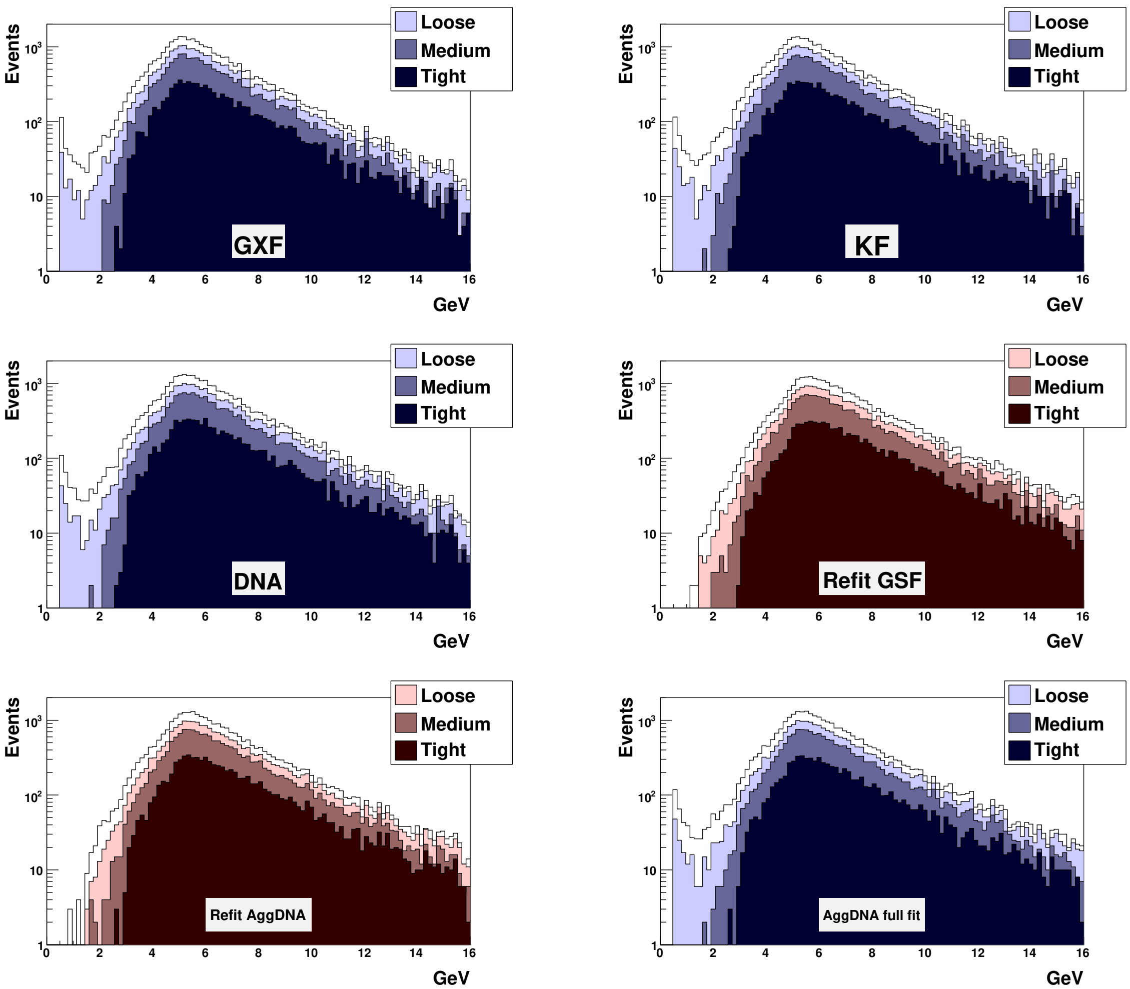

Figure 6.4: *Electron track p_T shown for J/ψ candidates with the different fitters, displayed from top left to bottom right; GXF, KF, DNA,GSF, refit AggDNA, AggDNA full fit. Both electrons are required to pass the electron quality criteria. Refits push p_T up but cannot find new tracks, by definition. Aggressive DNA full fit from RDOs also pushes up p_T but can recover new tracks too. Percentage of J/ψ candidates reconstructed by the different fitters, where both electrons are required to pass the electron quality criteria, are shown in Table* **??**.

lower numbers compared to GXF below this value and higher numbers above. It is clear that Refit GSF is most active at pushing up p_T. This effect is even more evident at large η .

J/ψ mass peak.

The position and resolution of the reconstructed J/ψ mass peak are a key indicator of a track fitter's performance.

Table **??** summarises the number of reconstructed J/ψ candidates in the mass range 1.5 GeV to 4.0 GeV, using the different fitters. The bremsstrahlung-aware fitters have more entries and show more symmetric resolution. There is also a noticeable pattern of mass shift; generic fitters -75 MeV, GSF +120 MeV and AggDNA -20 MeV.

Figure **??** shows the cases when both electrons are in the barrel and Figure **??** when both electrons are at $|\eta| > 1$. It is noticeable that the J/ψ mass width decreases as the electron quality criteria tighten. The GSF mass shift stands out, particularly at high η. The number of entries where both electrons are in these specified η ranges and pass the electron quality criteria is summarised in Table **??** for comparison of fit statistics.

	GXF	KF	DNA	Refit GSF	Refit AggDNA	AggDNA full fit
% reconstructed	70.4 ± 0.4	70.6 ±0.4	71.0 ± 0.4	69.5 ± 0.4	68.9 ± 0.4	71.4 ± 0.4
Peak value (GeV)	3.022	3.021	3.019	3.206	3.076	3.075
σ_L	0.356	0.228	0.181	0.225	0.186	0.186
σ_R	0.063	0.062	0.775	0.057	0.069	0.071

Table 6.7: *Reconstructed J/ψ candidates in the mass range 1.5 GeV to 4.0 GeV. The table shows the percentage of reconstructed J/ψ candidates compared with truth, mass peak value and left and right hand resolutions, σ_L, σ_R, of the asymmetric reconstructed mass peak (extracted from fits of Figure* **??***) for the different fitters. The bremsstrahlung-aware fitters have more entries and clearly show more symmetric resolutions. There is also a noticeable pattern of mass shift; generic fitters -75 MeV, GSF +120 MeV and AggDNA -20 MeV.*

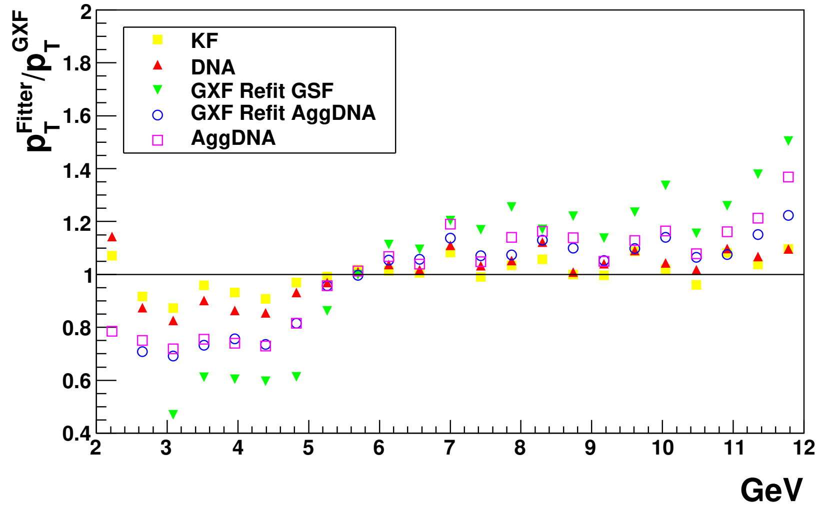

(a) Barrel

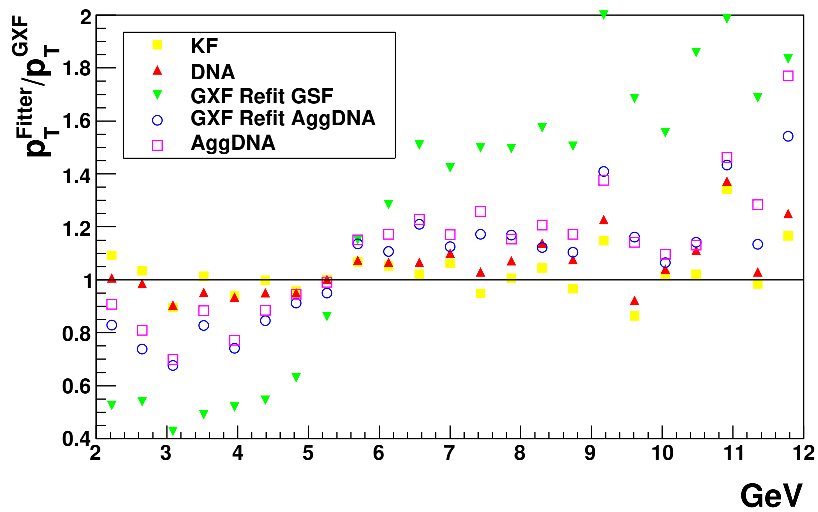

(b) $|\eta| > 1$

Figure 6.5: *Electron track p_T for each fitter wrt GXF electron track p_T. In the barrel all fitters show a similar trend compared with the default fitter GXF. At larger η, there is more marked difference between the fitters. The bremsstrahlung-aware fitters are clearly pushing up p_T, with GSF being the most active.*

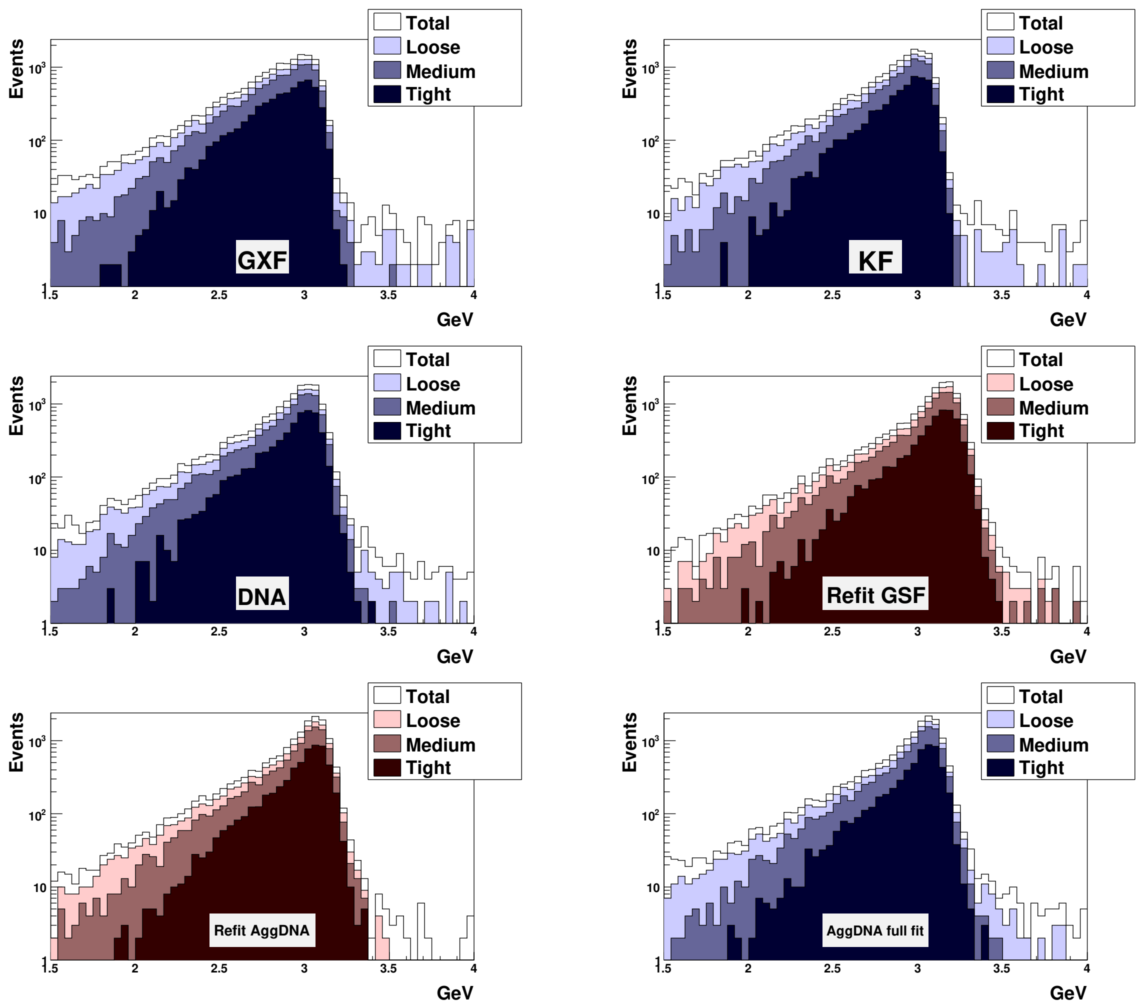

Figure 6.6: *Reconstructed J/ψ mass peak for the different fitters, in the barrel. Both electrons are required to be in region $|\eta| < 1$ and pass electron quality criteria. See Table* **??** *for a summary of the number of events passing the different electron quality criteria. The tightening of the J/ψ mass width is clearly visible as the electron quality criteria tighten.*

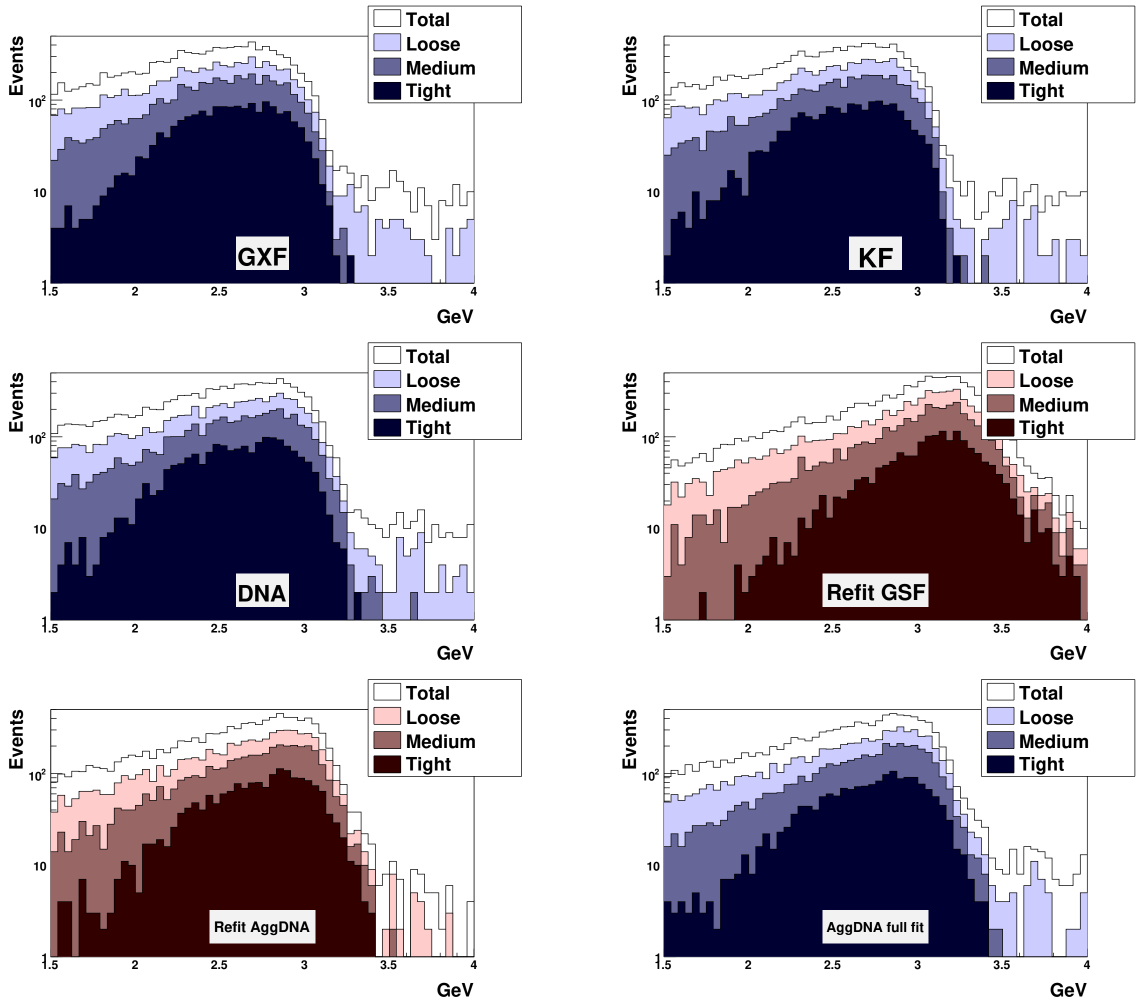

Figure 6.7: *Reconstructed J/ψ mass peak for the different fitters, outside the barrel. Both electrons are required in region $|\eta| > 1$ and pass the specified electron quality criteria. The GSF mass shift is very noticeable.*

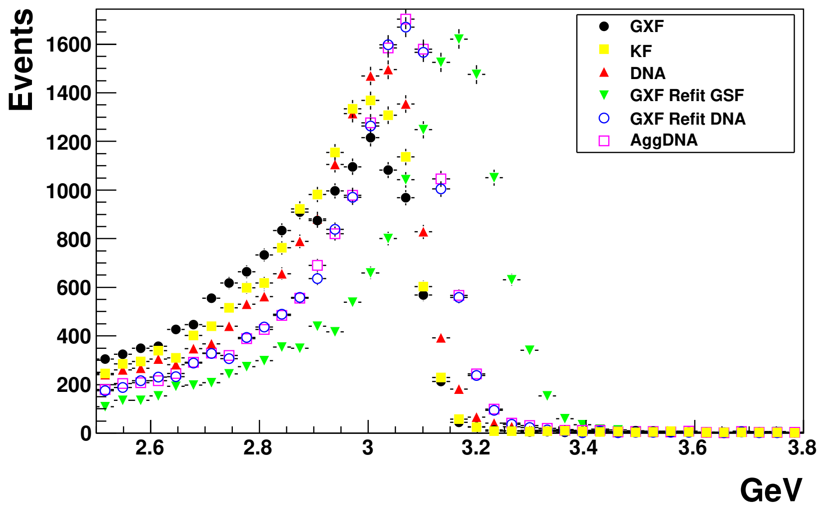

(a) Barrel

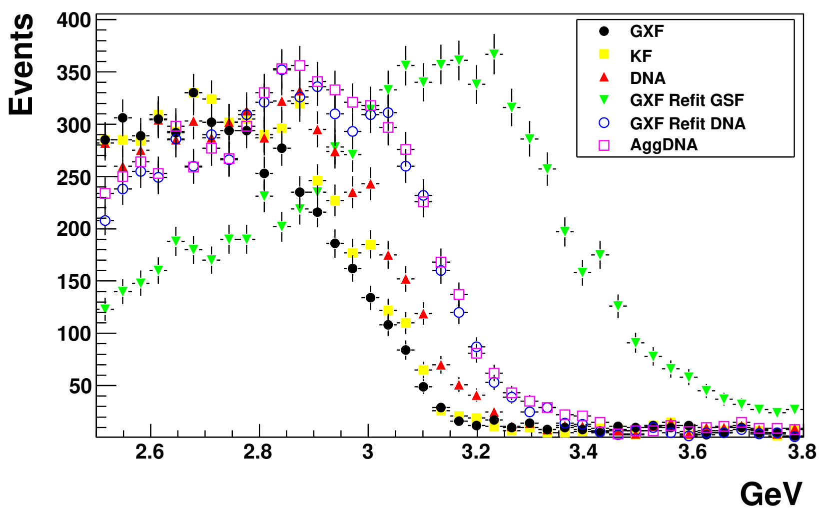

(b) $|\eta| > 1$

Figure 6.8: *J/ψ mass peak reconstructed with different fitters. As expected, the resolution of all fitters is better in the barrel. The pattern of mass shift is noticeable; generic fitters -75 MeV, GSF +120 MeV and AggDNA -20 MeV. GSF over estimation of J/ψ mass is clearly seen.*

Region	Criteria	GXF	KF	DNA	Refit GSF	Refit AggDNA	AggDNA full fit
$\lvert\eta\rvert < 1$	Total	77.0 ± 0.6	77.1 ± 0.6	77.2 ± 0.6	75.7 ± 0.6	75.7 ± 0.6	77.2 ± 0.6
	Loose	63.9 ± 0.6	64.1 ± 0.6	64.1 ± 0.6	63.2 ± 0.6	6.3 ± 0.6	64.0 ± 0.6
	Medium	51.3 ± 0.5	50.9 ± 0.5	51.5 ± 0.5	51.4 ± 0.5	51.4 ± 0.5	51.5 ± 0.5
	Tight	27.4 ± 0.4	27.4 ± 0.4	27.2 ± 0.4	27.4 ± 0.4	27.4 ± 0.4	26.8 ± 0.4
$\lvert\eta\rvert > 1$	Total	62.0 ± 0.6	62.2 ± 0.6	63.0 ± 0.6	62.4 ± 0.6	60.8 ± 0.6	64.1 ± 0.6
	Loose	39.3 ± 0.5	39.7 ± 0.5	40.1 ± 0.5	39.8 ± 0.5	39.0 ± 0.5	40.6 ± 0.5
	Medium	24.5 ± 0.4	24.5 ± 0.4	25.0 ± 0.4	24.9 ± 0.4	$24\ 8 \pm 0.4$	25.2 ± 0.4
	Tight	10.8 ± 0.3	11.0 ± 0.3	10.8 ± 0.3	10.7 ± 0.3	10.8 ± 0.3	10.7 ± 0.3

Table 6.8: *Percentage of reconstructed J/ψ candidates in mass range 1.5 GeV to 4.0 GeV. Numbers are shown for the different fitters where both electrons pass the electron quality criteria and are in the specified η range.*

6.1 Summary

The ATLAS track fitters all perform well in the last software release that I made the comparisons [2). However a new software release [3) is now available and first data has arrived. The obvious next step is to study the different track fitter performances on data.

[2)]The most recent athena release where I made comparisons was 15.2.0.1. Athena releases 15.4 and 15.5 were not used for comparison studies due to software problems with some fitters.

[3)]athena 15.6

'You know that we are living in a material world

And I am a material girl'

Madonna

7

Material Study

Mapping the material in ATLAS will be one of the major tasks at the beginning of data taking. The ultimate electron reconstruction performance will only be reached when the material quantity in the Inner Detector is understood.

The track reconstruction inefficiencies for pions and electrons reflect the shape of the amount of material in the Inner Detector, as described in the ATLAS Technical Design Report [**?**] and shown in Figure **??**. In addition to multiple scattering, pions are affected by hadronic interactions in the Inner Detector material, while electrons are subject to even larger reconstruction inefficiencies due to bremsstrahlung.

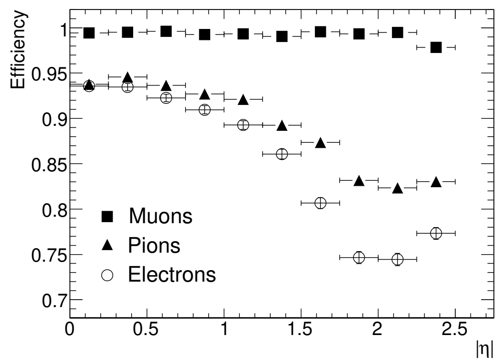

Figure 7.1: *Track reconstruction efficiencies as a function of $|\eta|$ for muons, pions and electrons with p_T=25 GeV. The inefficiencies for pions and electrons reflect the shape of the amount of material in the Inner Detector as a function of $|\eta|$ [**?**].*

This study considers the Dynamic Noise Adjustment (DNA) track fitter as a tool for mapping the material of the Inner Detector. DNA finds points on a trajectory where the momentum is changing. Both electron bremsstrahlung and pion scattering are happening in the material. The more material present the more the tracks will suffer momentum reduction leading to more 'DNA' hits. The aim of this study is to convert DNA information into a material budget.

There are many more pion tracks than electron tracks in an average LHC event and thus the vast majority of DNA activity will be due to pion scattering rather than electron bremsstrahlung. We will therefore not limit ourselves statistically by requiring electron tracks and an MC sample of indirect J/ψ decay in the di-muon channel is used in this study to emphasise the use of pions rather than electrons. In this approach, DNA fit effectively serves as a kink-finder.

7.0.1 ATLAS distorted geometry in simulations.

Mapping the material with data will be a long task. Simulations with distorted ATLAS detector geometry provide a good test bench to quantify detection possibilities.

This study was performed using the so-called Computing System Commissioning (CSC) distorted geometry [**?**]. In this description (CSC-01-02-00) material is added in only half of the Inner Detector at $0 < \phi < \pi$ as shown in Figure **??**. I will refer to $0 < \phi < \pi$ as $+\phi$ and $0 > \phi > -\pi$ as $-\phi$.

The barrel layer in front of SCT2 is implemented as a conical cylinder, increasing from 1% X_0 at the barrel centre to 3% X_0 at the barrel end. The extra material dimensions being R_{min}=347.015 mm and R_{max}=348.9 mm at z=0 mm increasing to R_{min}=343.245 mm and R_{max}=348.9 mm at z=781 mm. The radiation lengths stated are for particles travelling normal to the surface. The resulting radiation lengths at $|\eta| > 0$ will therefore be higher due to the incident angle.

7.0.2 ATLAS inner detector material budget

The material distribution in the ATLAS inner detector is shown in Figure **??** a) in radiation lengths and in Figure **??** b) in interaction lengths. The relation between interaction (X_0) and radiation length (λ) depends upon the material's nuclear structure. For example, carbon has a radiation length of 42.7 gcm^{-2} and nuclear interaction length of 85.8 gcm^{-2} [**?**]. So in the case of carbon 1% X_0 carbon is roughly equivalent to 0.5% λ.

7.0.3 Material information from geantino scans

Geant4 is a toolkit for the simulation of the passage of particles through matter. Geantinos are a Geant4 construct [**?**]. These 'particles' do not interact with matter, they just carry information about the geometry they traverse.

The simulation interface permits the specification of parameters such as the ATLAS geometry model, primary vertex position and η region. The resulting scans illustrate the material budget of the separate constituents of the Inner Detector, as shown in Figure **??**.

Geant4 was used to extract the amount of material for the four SCT layers and the 'extra'

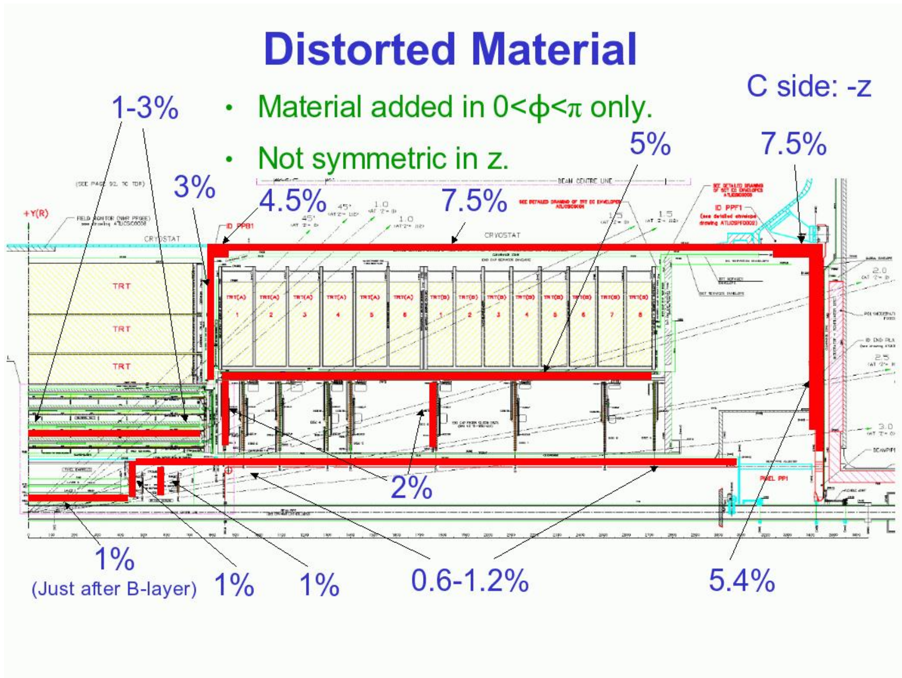

(a) C side: -z

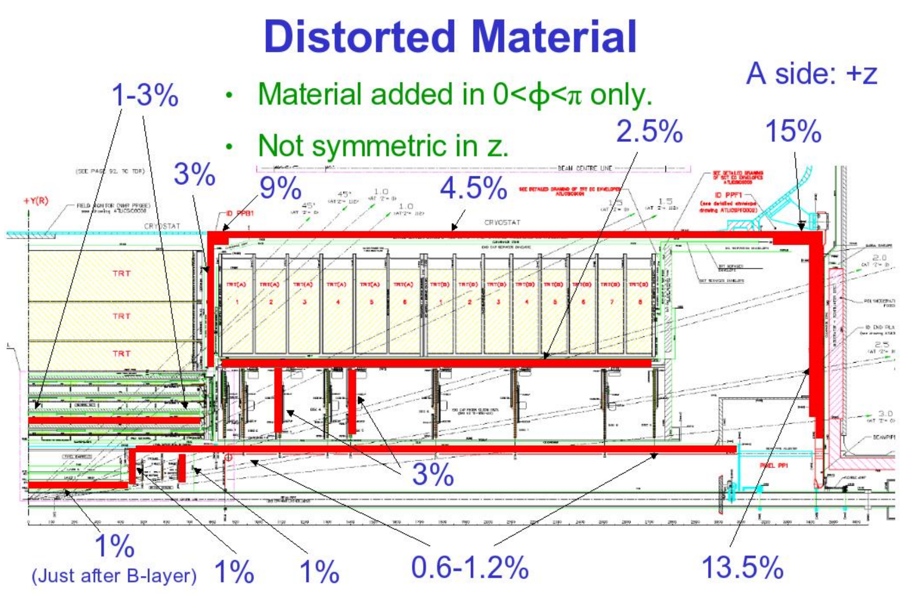

(b) A side: +z

Figure 7.2: *ATLAS simulation geometry (CSC-01-02-00), with additional material shown in red. Additional material is present in barrel SCT layer 2 in* $+\phi$ $(0 < \phi < \pi)$ *for both positive and negative z. The distorted geometry of ATLAS detector in simulations provides a good test bench to quantify detection possibilities.*

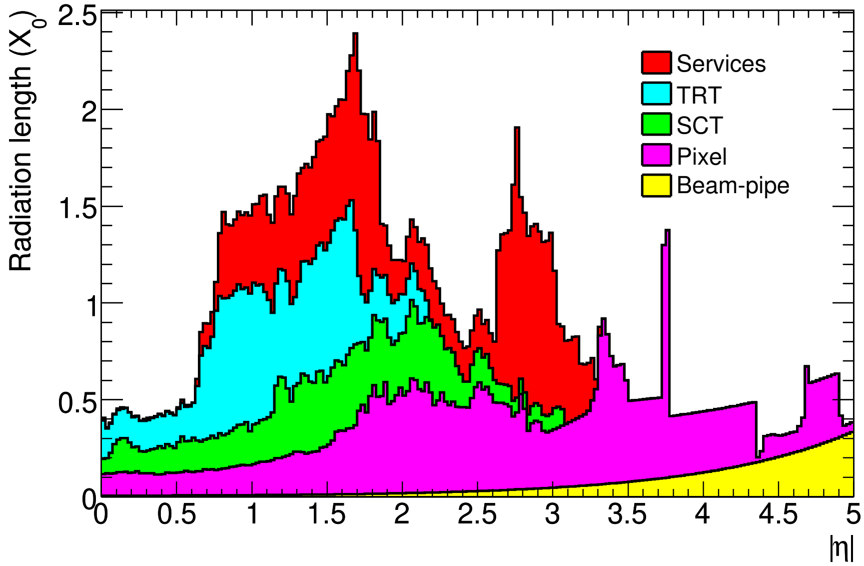

(a) Inner Detector Material budget in terms of radiation length.

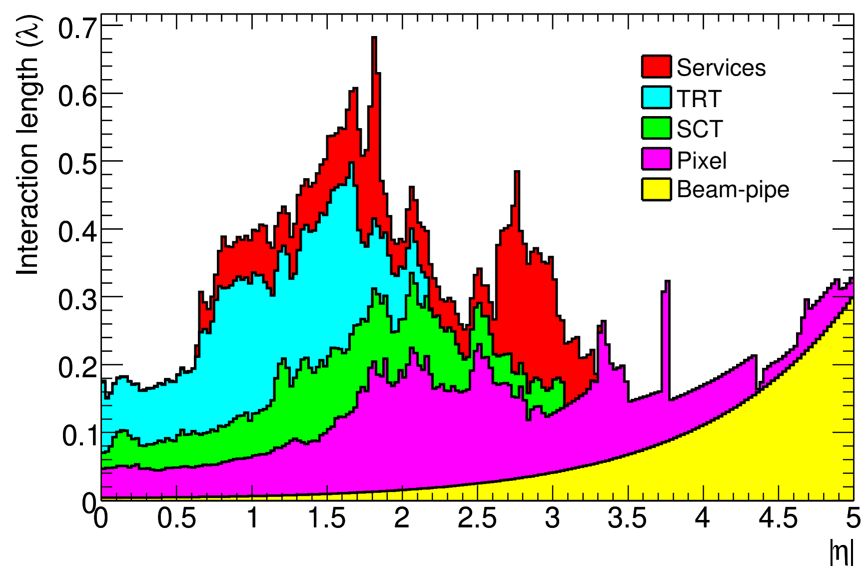

(b) Inner Detector Material budget in terms of interaction length.

Figure 7.3: *Material distribution in radiation and interaction lengths (X_0, λ) at the exit of the Inner Detector envelope, including the services and thermal enclosures. The distribution is shown as a function of $|\eta|$ and averaged over ϕ. The breakdown indicates the contributions of external services and of individual sub-detectors, including services in their active volume [**?**].*

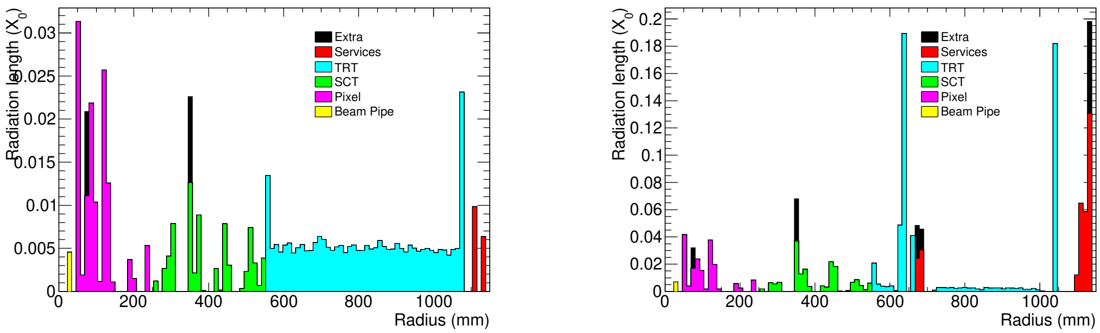

(a) 0.00< η <0.01

(b) 0.99< η <1.00

Figure 7.4: *Geantino scans of the Inner Detector. The material budget within the Inner Detector envelope including services is shown in two η ranges. The 3 pixel layers, in pink, and the 4 SCT layers, in green, can be clearly seen. The extra material contributions are shown in black.*

material at barrel layer SCT2.

The distribution of this extra material in terms of η is shown in Figure **??**. The fitted function takes into account the linear increase of material from 1% X_0 at z=0 mm to 3% X_0 at z=781 mm. The factor $1/\sin\theta$ accounts for the effective increase in material due to the angle of incidence. The function is parameterised as

$$\begin{aligned} & 1\%\left(1+2(z/z_{max})\right)\frac{1}{\sin\theta} \\ = {} & 1\%\left(1+2(R/z_{max})\frac{1}{\tan\theta}\right)\frac{1}{\sin\theta} \\ = {} & 1\%(1+2(R/z_{max})\sinh\eta)\cosh\eta \end{aligned} \tag{7.1}$$

where R=347.96 mm, the average radius of extra material at z=0 mm and z_{max}=781 mm, the full length of the barrel.

Looking purely at the silicon structure of the four barrel SCT layers, Figure **??** shows that each layer is essentially a cylinder of constant thickness, 0.07 mm. The effective radiation length

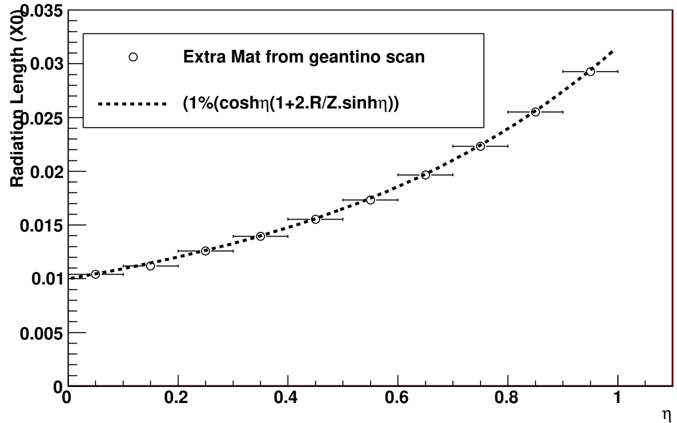

Figure 7.5: *A conical cylinder of carbon in front of SCT2, increases from 1% X_0 at the barrel centre to 3% X_0 at the barrel end. The fitted function takes into account the linear increase in material, 1%$(1+2R/z_{max}sinh\eta)$, plus the coshη effective increase in material due to the angle of incidence.*

increases with η as $1/\sin\theta$ due to the incident angle. The fit function used is

$$0.068/\sin\theta = 0.068\ \cosh\eta \tag{7.2}$$

showing that the material budget of each silicon layer is $6.8\% X_0$ However when the total SCT material is taken into account, with contributions from many components, a lot more structure is seen in the distribution of material. This is shown in Figure **??** with respect to η and with respect to z in Figure **??**. The peaks in the material distributions are mainly due to the hybrid assembly, a component of each module which contains the readout electronics (see Chapter **??**, Figure **??**).

The total SCT material budget is shown in Figure **??**, with contributions from the 4 individual SCT layers shown. The modules line up in z but not in η. This is particularly noticeable at η ~0.1, where the hybrid assemblies from all 4 SCT layers align resulting in a track from z=0 traversing $\sim$ 22% X_0. Contrasting with η ~0.25 where a track from z=0 would not traverse a single hybrid assembly and thus only $\sim 5\% \ X_0$.

Figure **??** shows the layout of the modules in diagrammatic form, illustrating the lining up of the hybrid material between SCT layers. This diagram also shows the asymmetry of the SCT module layout, such that the hybrid structure positions are not symmetric about η=0.

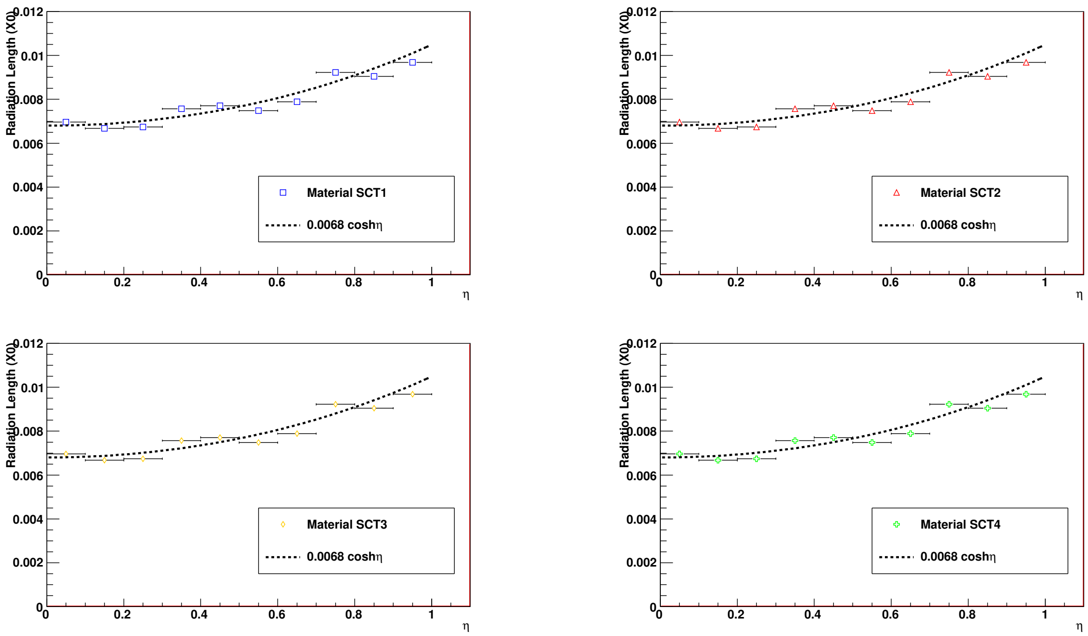

Figure 7.6: *Material distribution of the silicon sensor, for the four SCT layers, as a function of η. Purely looking at the silicon structure of the SCT, each SCT layer is essentially a cylinder of constant thickness. The effective radiation length increases with η as $1/\sin\theta$ due to the incident angle, which is equivalent to* $\cosh\eta$.

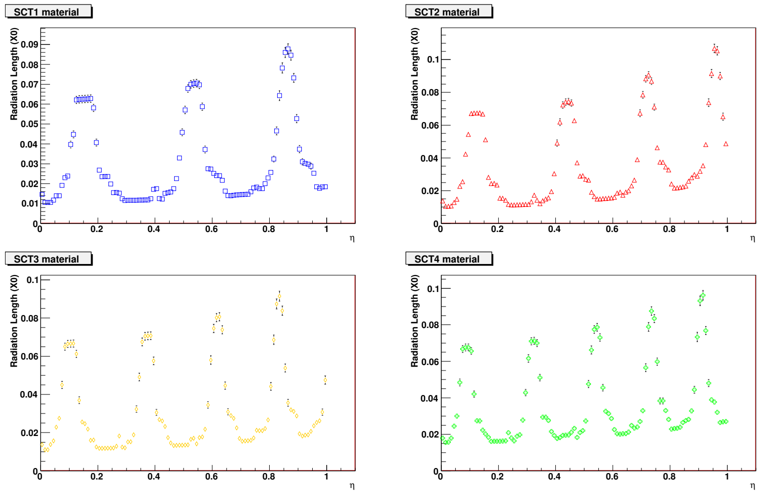

Figure 7.7: *Material distribution of the four barrel SCT layers as a function of η. When all components of the SCT are considered then there is more structure to the SCT material budget. The peaks are mainly due to the hybrid assembly, a component of each module which contains the readout electronics. See Chapter* **??**, *Figure* **??** *for SCT barrel module description. The material structure alignment is shown in diagrammatic form in Figure* **??**.

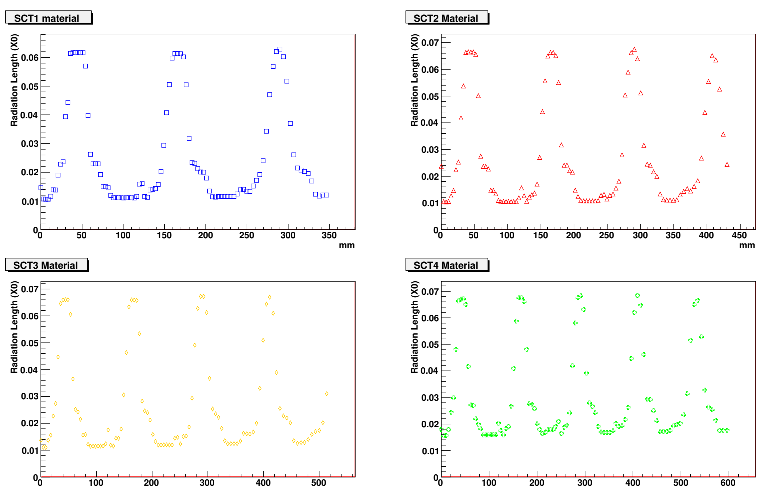

Figure 7.8: *Material distribution of the barrel SCT as a function of z. The material is shown here for each SCT layer in positive z, for $\eta < 1$. The material structure alignment in z is shown in diagrammatic form in Figure* **??**.

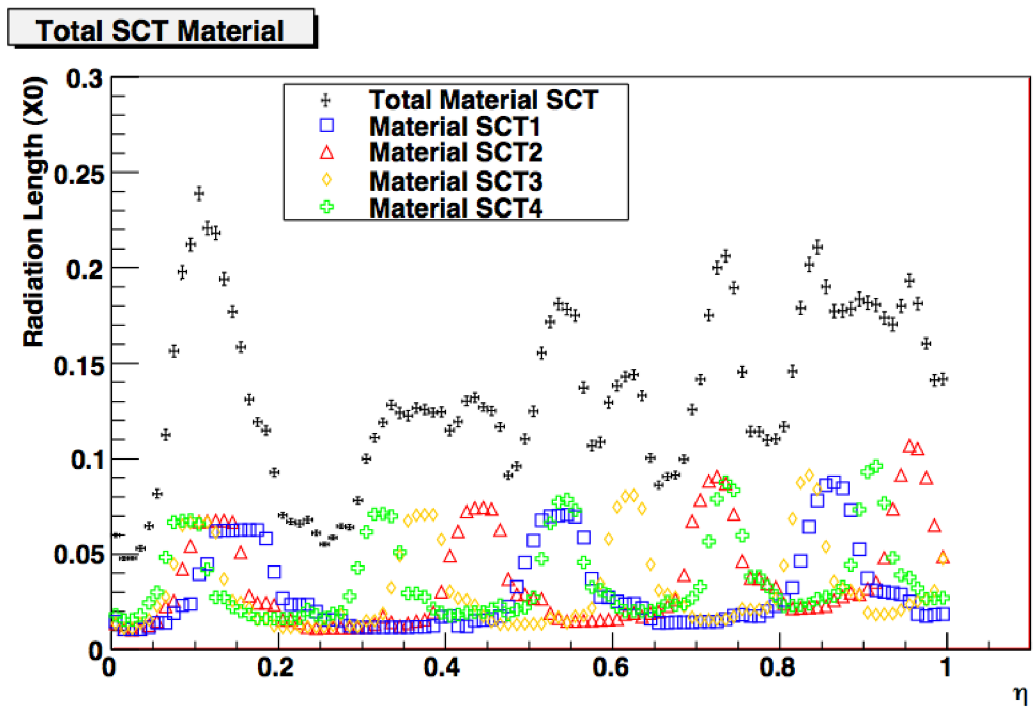

Figure 7.9: *Material distribution of the barrel SCT as a function of* η*. Each SCT layer has 12 SCT modules lined up in z along the length of the Inner Detector barrel. Due to the structure of the modules this lining up can cause fluctuations in the total SCT material budget. This is particularly noticeable at* η *~0.1, where the hybrid assemblies from all 4 SCT layers align resulting in a track from z=0 traversing* $\sim 22\% X_0$*. Contrasting with* η *~0.25 where a track from z=0 would not traverse a single hybrid assembly and thus only* $\sim 5\% X_0$*.*

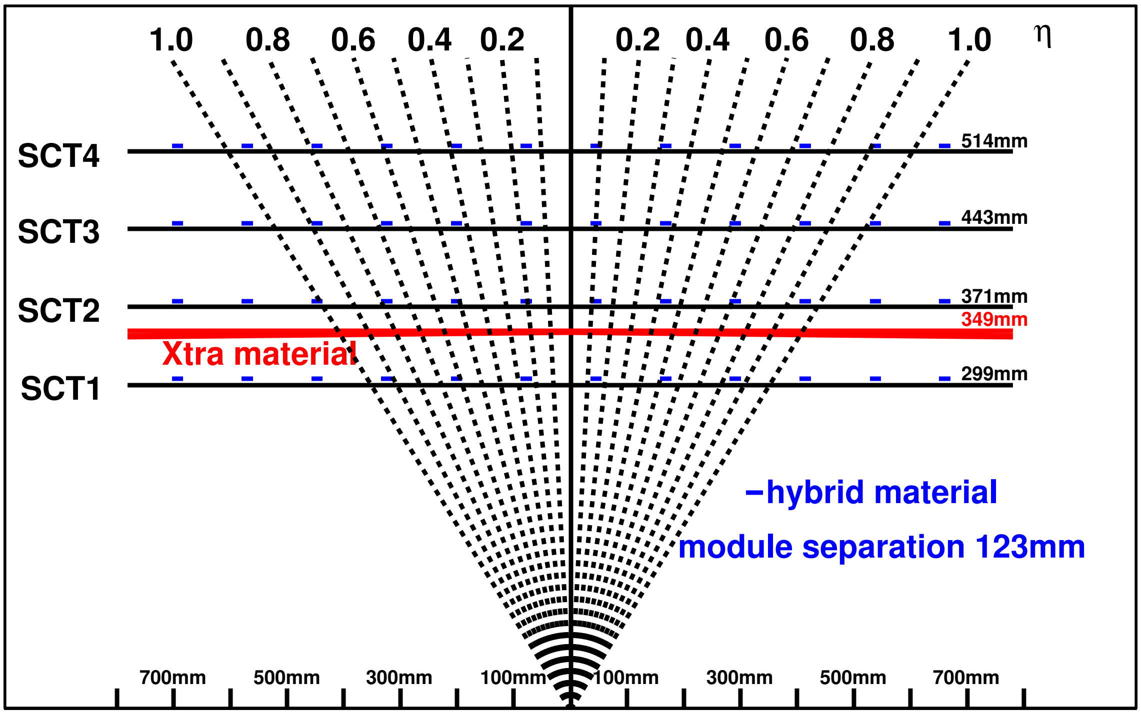

Figure 7.10: *Simple diagramatic representation of the SCT layout decsribed by ATLAS geometry CSC-01-02-00. The hybrid assembly of readout electronics makes a considerable material contribution. When the hybrid assemblies of the 4 SCT layers line up in η, then the SCT material traversed by a particle is greatly increased. This diagram also shows the asymmetry of the SCT module layout, such that the hybrid structure positions are not symmetric about η=0. The material contribution from the hybrid structures can be seen in the geantino scans, with Figure* **??** *showing structures in z and Figure* **??** *showing structures in η.*

In this material study we will assume that all tracks are due to pions. It is therefore necessary to convert the SCT material budget from radiation lengths into interaction lengths.

The contributions from the four main SCT components (as described in Chapter **??**, Section **??**) is shown in Figure **??**, measured in radiation lengths. The hybrid assemblies make a considerable contribution, in addition to the fairly constant material contribution from the silicon sensors.

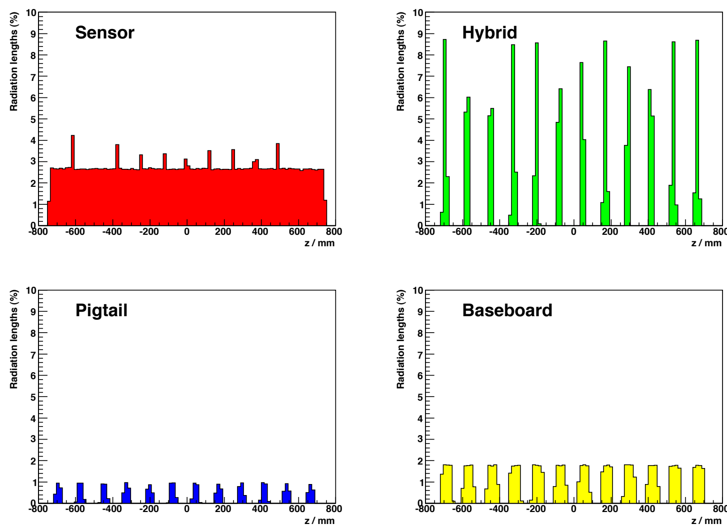

Figure 7.11: *Material budget measured in radiation lengths as a function of z. The material budget of the 4 key components of SCT barrel modules are shown. Structure can be clearly seen. Detector geometry model ATLAS-GEO-03-00-00 [**?**].*

Figure **??** focuses on a single module, showing the contributions from the four main components. The material budget in radiation lengths was extracted from geantino scans and the material budget in interaction lengths was estimated using values from Table **??**. To convert the material budget from radiation lengths to interaction lengths the silicon contribution was reduced by a fifth (22 X_0:108 λ) and the baseboard contribution by a half (41 X_0:85 λ). For the remainder of the material a conversion factor was approximated to a third, to try and take into account the metal and kapton contributions.

Structure	Material	Radiation length (X_0) gcm^{-2}	Nuclear interaction length (λ) gcm^{-2}
Sensor	Silicon	21.82	108.4
Baseboard	BeO	41.3	85.0
Baseboard	Graphite	42.70	85.8
Hybrid	Copper	12.86	137.3
Pigtail	Aluminium	24.01	107.2
Hybrid, Pigtail	Kapton (polymide)	40.56	85.8

Table 7.1: *Atomic and nuclear properties of materials: [**?**]*

There is greater modulation in the SCT material budget when it is considered in interaction lengths compared to radiation lengths i.e. the peak height is 11 times the silicon contribution when measured in interaction lengths compared to only 7 times when measured in radiation lengths(0.022 λ/0.002 λ c.f. 0.07 X_0/0.01 X_0). The average contribution of a single SCT layer is calculated from Figure **??** to be ~2.3% X_0 or ~0.7% λ.

The validity of this conversion was checked with two other sources

- The material budget for the Inner Detector is shown in Figure **??** [**?**] in interaction lengths. The total contribution from the SCT at η=0 is 8% λ and thus 2% λ per SCT layer.
- The ATLAS Technical Design Report [**?**] illustrates the Inner Detector material budget as shown in Figure **??**. At $|\eta|$=1 the SCT contribution is ~13.5% X_0 or ~6.5% λ, which indicates ~8.7% X_0 or ~4.2% λ at η=0 when $1/\sin\theta$ considered, or 1% λ per SCT layer.

The track p_T distribution is fairly constant over the range $|\eta| < 1$, as shown in Figure **??**. This η range is equivalent to $|z|$ <500 mm for SCT2. Track distribution should therefore not affect the number of DNA hits observed in the range considered.

The SCT material contribution was extracted from geantino scans in the range z=-500 mm to z=500 mm in 5 mm bins. The material budget, in interaction lengths, of a single SCT barrel layer is shown in Figure **??**.

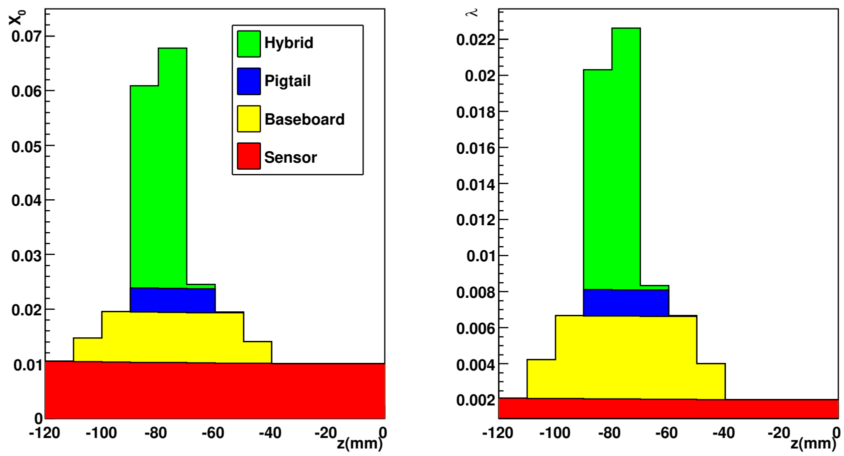

Figure 7.12: *Material budget of a single SCT barrel module, in radiation lengths (left). Conversion from radiation lengths to interaction lengths is estimated by considering the four main components (right), using material properties shown in table* **??**.

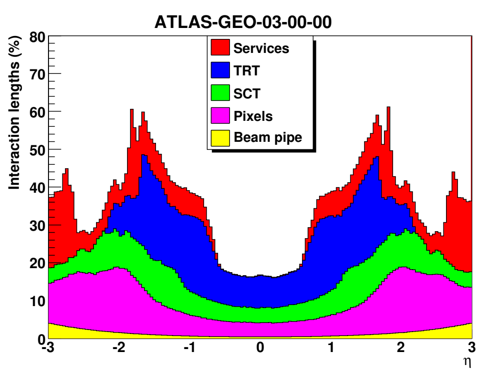

(a) Inner Detector material budget. Contributions shown from sub-detectors and extra material [**?**].

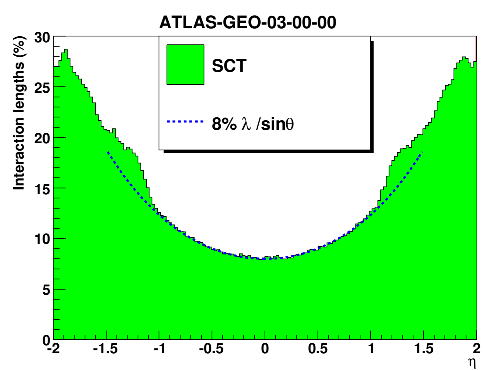

(b) SCT material budget.

Figure 7.13: *Material budget measured in Interaction Lengths, λ as a function of η. A region of* $1/\sin\theta$ *(*$\cosh\eta$*) is seen for the SCT material budget for* $|\eta| < 1$*, with 8%* λ *at* η*=0. The* $1/\sin\theta$ *dependence is due to the incident angle of the track traversing material. Vertex smearing results in SCT structure smoothing.*

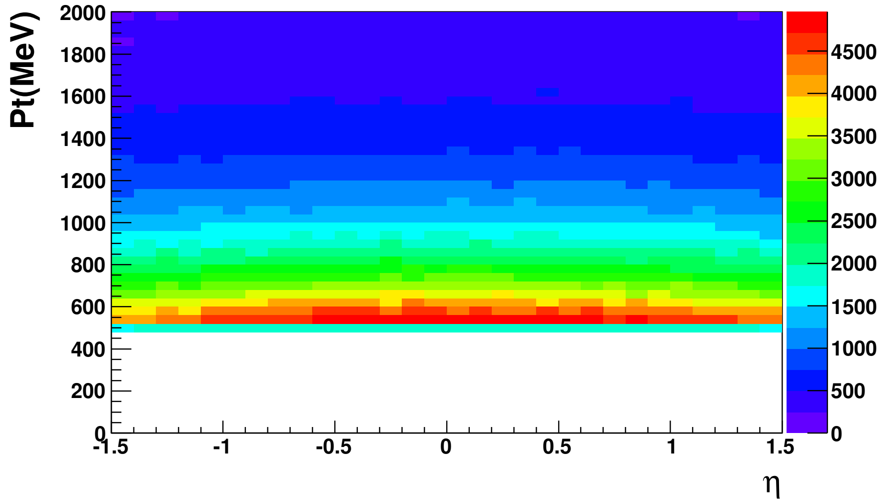

Figure 7.14: *Reconstructed track p_T distribution as a function of η . The track p_T is fairly constant over the range $|\eta| < 1$ which is equivalent to $|z|$ <500 mm for SCT2. The MC sample used is indirect $J/\psi(\mu\mu)$ with a 6 and 4 GeV muon.*

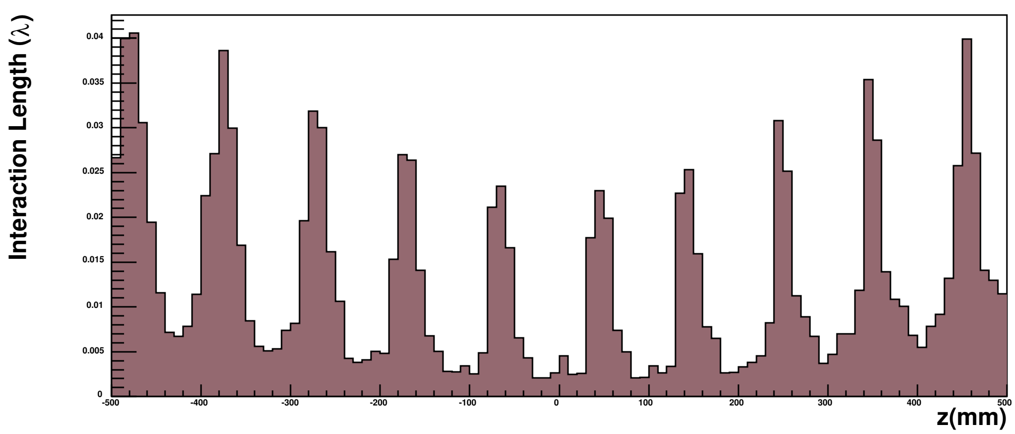

Figure 7.15: *Material budget of a single SCT barrel layer measured in interaction lengths as a function of z.*

7.1 Material Study using DNA track fitter

The aim of this study is to convert DNA hits into a material budget measured in interaction lengths. A 'DNA hit' is a hit on an active layer where the track momentum has reduced and the DNA fitter flags a possible brem. Figure **??** shows the position of DNA hits in a cross-section view of the barrel. The 4 SCT barrel layers show up clearly, since more material leads to more DNA hits.

Material causes DNA activity, not just in the same layer, but also in the following layer. Depending on the fit direction, this is felt in the next outside layer in forwards fit, and the preceding inside layer for backwards fit. This happens because sometimes the deviation from the direction is not significant at that hit, but becomes significant at the next. So, sometimes a DNA hit is associated to the next layer rather than the current one. Without this complication there would be a 1:1 correspondence between DNA hits and the amount of material (subject to efficiency).

The number of DNA hits as a function of η and integrated over ϕ, for the four SCT layers is shown in Figure **??** and Figure **??** . The difference in the number of hits in $+\phi$ and $-\phi$ is shown in the lower row. Figure **??** shows increased number of DNA hits in $+\phi$ at SCT2 and SCT3 compared with SCT1 and SCT4, since in forwards fit the DNA activity from the extra material at SCT2 $+\phi$ is being picked up at that layer and the following layer. Figure **??** shows increased number of DNA hits for $+\phi$ at SCT1 and SCT2 compared with SCT3 and SCT4, since in backwards fit the DNA activity from the extra material at SCT2 is being picked up at that layer and the preceding layer.

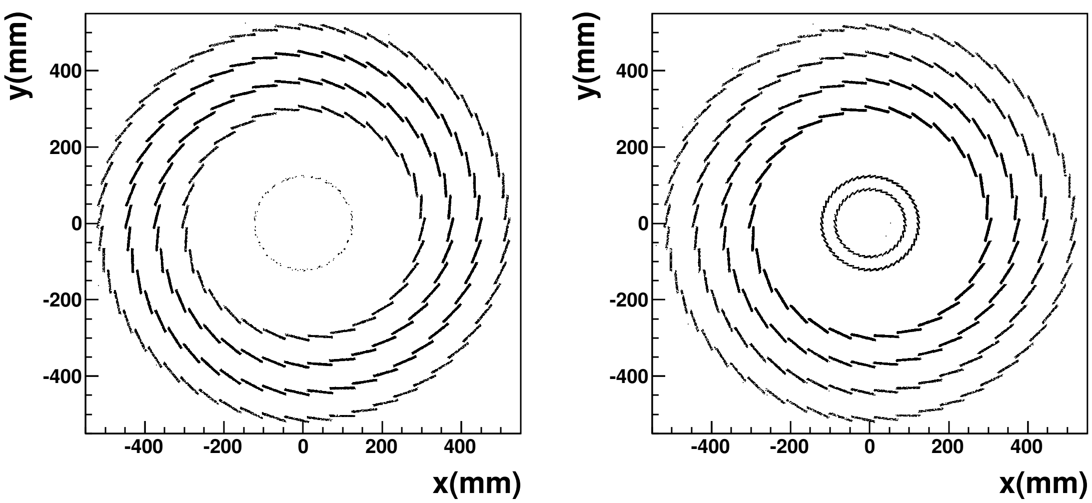

Figure 7.16: *The position of DNA hits is plotted as a function of x and y, providing a cross-section view of the barrel. DNA hits for forwards (left) and backwards(right) track fitting is shown. The more material there is the more DNA activity is observed. The location of the bremsstrahlung is not precise and the effect often shows up in the next layer. Depending on the fit direction, this is felt in the next outside layer in forwards fit, and the preceding inside layer for backwards fit.*

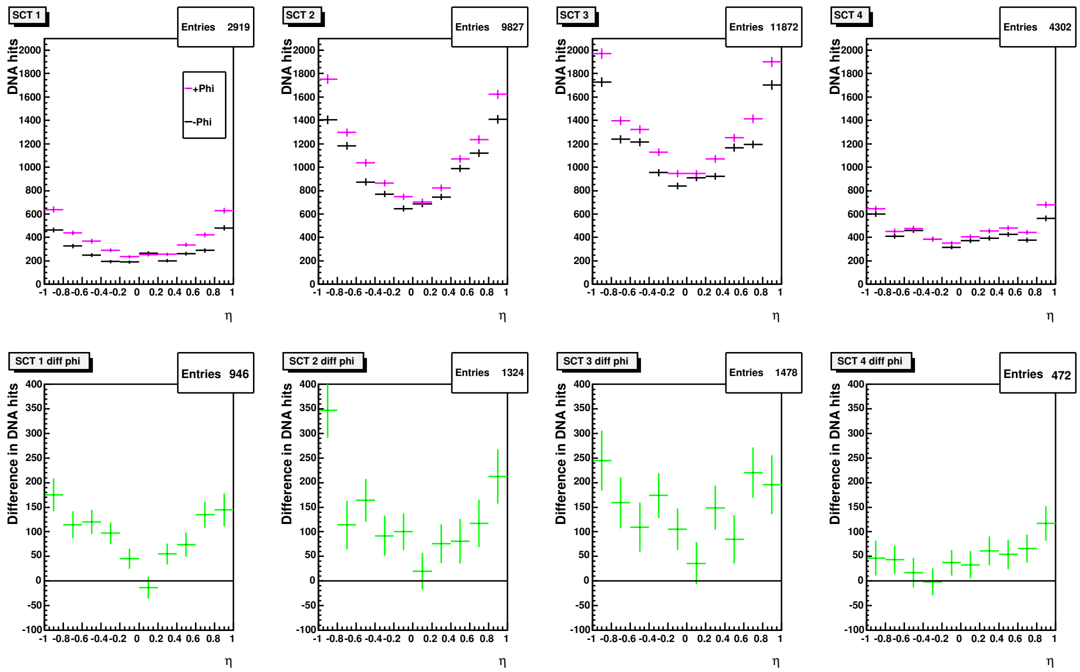

(a) Forwards Fit.

Figure 7.17: *The number of DNA hits as a function of η and integrated over ϕ, for $+\phi$ (pink) and $-\phi$ (purple). The difference in the number of hits between $+\phi$ and $-\phi$ shown in the lower row (green), for the four SCT layers. Forwards fit: The number of DNA hits increases as the fit progresses from SCT1(top left) through to SCT3. The number of DNA hits reduces for SCT4 (top right) since the next tracking measurement is from the TRT, which has large errors, so DNA cannot get a good hold on the change in momentum. The difference in the number of DNA hits between $+\phi$ and $-\phi$ (bottom row) clearly shows an increase at SCT2 and SCT3, the layer with the extra material and the following outside layer*

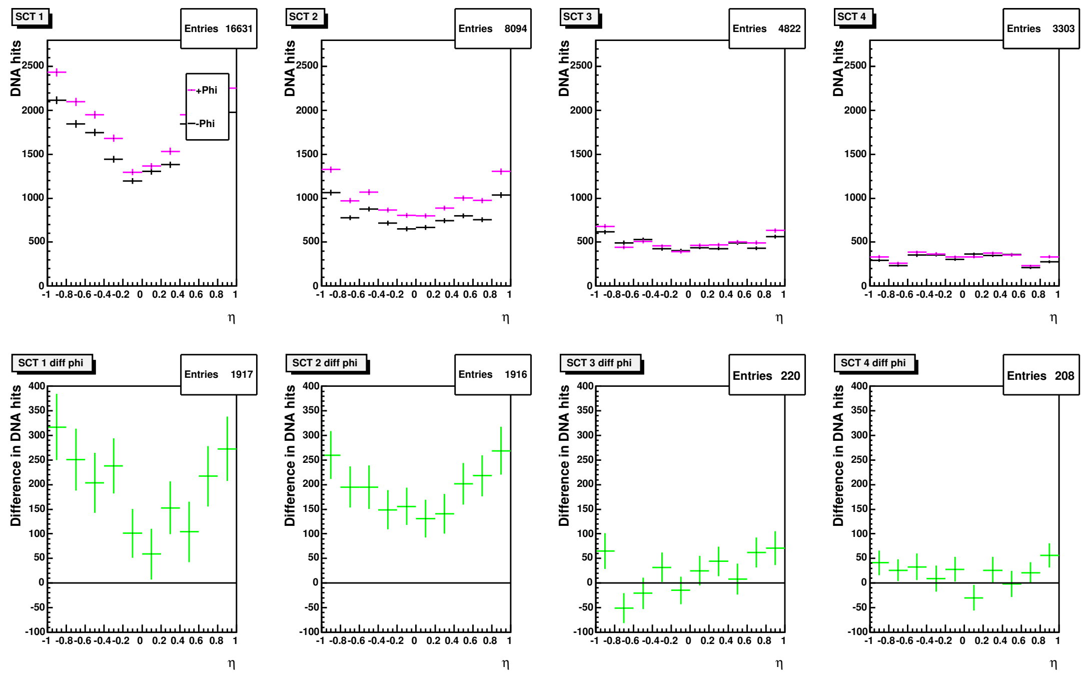

(a) Backwards Fit.

Figure 7.18: *The number of DNA hits as a function of η and integrated over ϕ, for $+\phi$ (pink) and $-\phi$ (purple). The difference in the number of hits between $+\phi$ and $-\phi$ shown in the lower row (green), for the four SCT layers. Backwards fit: The number of DNA hits increases as the fit progresses from SCT4 (top right) through to SCT1 (top left). The difference in the number of DNA hits between $+\phi$ and $-\phi$ (bottom row) clearly shows an increase at SCT1 and SCT2, the layer with the extra material and the preceding inside layer.*

7.1.1 Model

Using forwards tracking, DNA hits seen at SCT2 will be due to material in SCT1 as well as SCT2. In $+\phi$, there will also be a contribution from the ‘extra’ material just in front of SCT2. The extra material can be used to help understand the material layout and set the scales.

With knowledge gained from studying DNA hits at SCT2 $+\phi$, DNA hits seen at SCT2 $-\phi$ can then be converted into a material budget for SCT2 measured in interaction lengths. This should be consistent with the SCT material contribution, as measured by the geantino scans.

The impact of SCT2 on DNA hits can be considered true to its actual material structure, such that the more material there is in SCT2, the more DNA hits will be observed at SCT2.

The reconstructed longitudinal impact parameter, $z0$, is non-zero as shown in Figure **??**. Thus only a small percentage of tracks originate from z=0. This means that a DNA hit at a certain location in SCT2 could have traversed SCT1 in a range of locations, and so traversed a different amount of material, as indicated in Figure **??**. The material contribution from SCT1 therefore needs to be smeared to take into account the variation in material traversed by the track.

The smearing is carried out such that the actual SCT material (Figure **??**) is shifted by the reconstructed $z0$ value and weighted by the fraction of events in that $z0$ range. Hence greatest weight is given to material near η=0 and contributions from larger $|z0|$ are included with a smaller weight. The resulting material contributions of SCT1 and SCT2 are shown in Figure **??**.

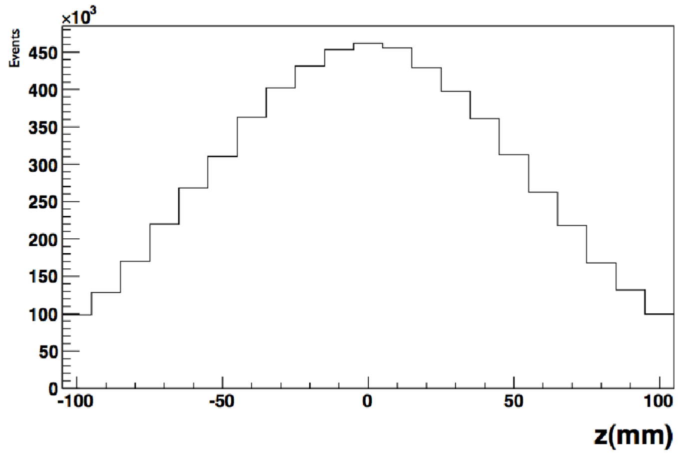

Figure 7.19: *Reconstructed longitudinal impact parameter, $z0$, as a function of z. Non-zero $z0$ necessitates the smearing of SCT1 material.*

The key features of the model are:

1. Highly modulated pattern from SCT2.

2. Similar, but smeared pattern from SCT1.

3. Extra material implemented as 0.5 $\%\lambda$ at z=0 increasing to 1.5 $\%\lambda$ at the end of the barrel (z_{max}=781 mm), with a $1/\sin\theta$ factor due to the incident angle. This is parameterised as

$$0.5\%\left(1+2\frac{z}{z_{max}}\right)\frac{1}{\sin\theta}$$

4. Constant noise term. Previous studies have shown that a significant fraction of DNA hits in pion tracks are actually fakes. No interaction takes place. There is simply a fluctuation in the measurement which initiates DNA activity. A certain amount of noise is therefore expected but, since ATLAS is cylindrically symmetrical, noise cannot depend on z.

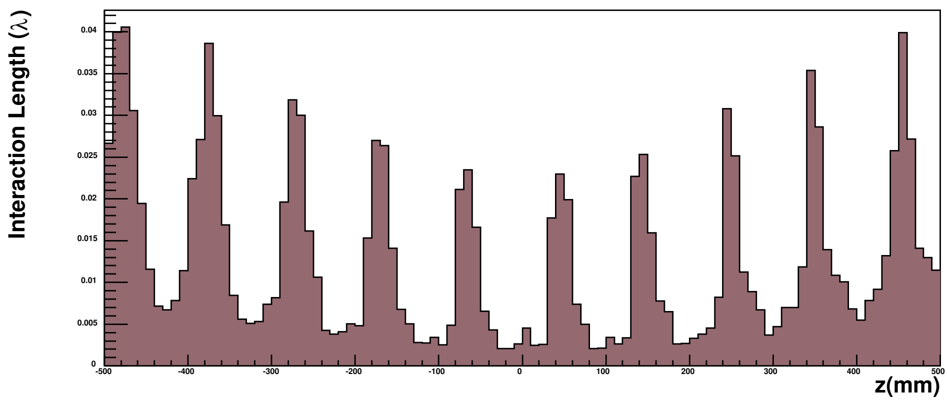

(a) SCT2

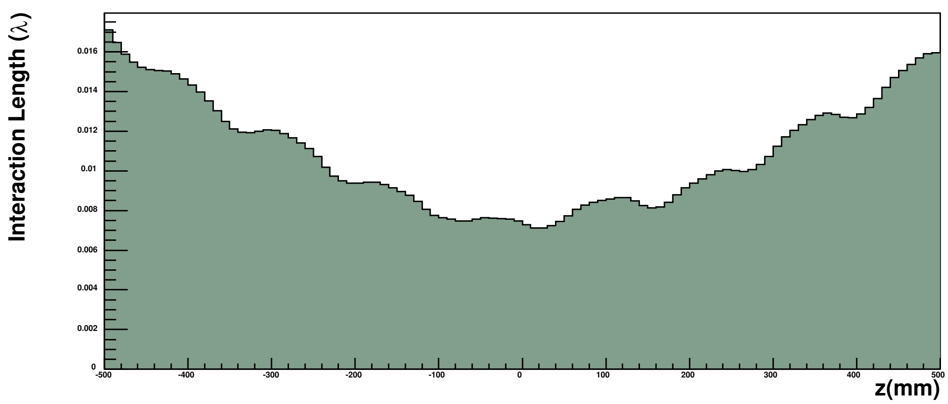

(b) SCT1

Figure 7.20: *SCT1 and SCT2 material contributions in interaction lengths as a function of z. Since DNA hits at SCT2 are to be studied, the impact of SCT2 is considered true to the actual material structure whereas the material contribution from SCT1 is considered to be smeared.*

A model of the relationship between the number of DNA hits at SCT2 $+\phi$ and the material associated with those hits might look like:

$$N = P(\mathrm{Mat_{SCT2}} + E \cdot \mathrm{Mat_{SCT1}} + \mathrm{Mat_{extra}}) + C \tag{7.3}$$

where

- N=Number of DNA hits per 1k events.
- P=A factor accounting for the overall sensitivity of DNA.
- E=Sensitivity of DNA to previous material layer.
- $\mathrm{Mat_{SCT2}}$=Amount of SCT material at current layer as shown in Figure **??** a).
- $\mathrm{Mat_{SCT1}}$=Amount of SCT material at previous layer as shown in Figure **??** b).
- $\mathrm{Mat_{extra}}$=Amount of extra material in detector simulation as shown in Figure **??**.
- C=Constant noise term.

Since the extra material is essentially at the same radius as SCT2, DNA sensitivity is considered the same for both of these material layers. The extra material has a well understood 'simple' structure and thus is used to set the scale.

7.1.2 Fit Results

The ROOT [**?**] minimisation package TMinuit is used to fit the proposed function to the DNA hits at SCT2 $+\phi$, forwards fit. The fit result is shown in Figure **??**, the parameter values in Table **??** and the parameter correlation coefficients in Table **??**. The χ^2 of the fit is 225.5 per 97 degrees of freedom.

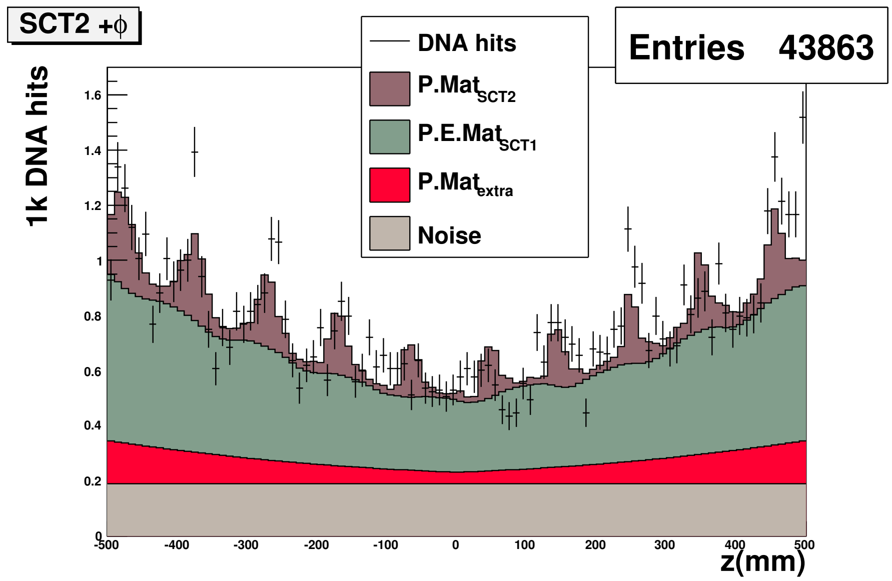

Figure 7.21: *DNA hits at SCT2 +ϕ for $|z|$ <500 mm. The fit results are shown; the constant noise contribution in grey, extra material contribution in pink, smeared contribution from SCT1 in green and the highly modulated contribution from SCT2 in purple.*

Parameter	Value	Error
C	0.19	0.03
E	4.35	0.76
P	8.13	0.77

Table 7.2: *Parameter values from TMinuit.*

Parameter	C	E	P	Global
C	1.000	-0.633	0.273	0.97204
E	-0.633	1.000	-0.911	0.99493
P	0.273	-0.911	1.000	0.99215

Table 7.3: *Parameter Correlation Coefficients from TMinuit. There is a high correlation between the factor for overall sensitivity to DNA, P, and the factor that weights the sensitivity of DNA to the previous layer, E. This is expected since there is little structure in the SCT1 material contribution to separate the two parameters.*

The parameters obtained from the fit in +ϕ will now be used to extract the material budget of SCT2 from the DNA hits in $-\phi$.

The detector simulation does not have extra material in $-\phi$, so Equation **??** becomes

$$N = P(\text{Mat}_{\text{SCT2}} + \text{E} \cdot \text{Mat}_{\text{SCT1}}) + C \tag{7.4}$$

and rearranging gives

$$(N - C)/P = \text{Mat}_{\text{SCT2}} + E \cdot \text{Mat}_{\text{SCT1}} \tag{7.5}$$

The DNA hits in $-\phi$ purely due to material are therefore represented by $(N - C)/P$. Since the material was measured in interaction lengths, then the units of $(N - C)/P$ are also in interaction lengths.

One could simply plot the following

$$\text{Mat}_{\text{SCT2}} = (N - C)/P - E \cdot \text{Mat}_{\text{SCT1}} \tag{7.6}$$

for SCT2 DNA hits in $-\phi$, to extract the DNA hits due to the material of SCT2. However I chose another approach: parameter E still weights the sensitivity of DNA to the preceding layer, but the DNA hits coming from SCT2 have a weight of 1 and those DNA hits from SCT1 have a weight of E. With this method a better understanding of the errors is available.

Equation **??** becomes

$$(N - C)/P = \text{Mat}_{\text{SCT}}(1 + E) \tag{7.7}$$

So considering the overall contribution of DNA hits due to material, a factor $E/(E + 1)$ is due to SCT1 and a factor $1/(E + 1)$ is due to SCT2.

The contribution from SCT2 is now

$$\mathrm{Mat}_{\mathrm{SCT}} = ((N-C)/P) \cdot 1/(1+E) \tag{7.8}$$

and the contribution from SCT1

$$\mathrm{Mat}_{\mathrm{SCT}} = ((N-C)/P) \cdot E/(1+E) \tag{7.9}$$

This distribution is plotted in 100 mm bins to smear any material structure effects, and shown in Figure **??** a). $1/\sin\theta$ is fitted to estimate the smoothed SCT1 contribution.

Figure **??** b) shows the overall contribution of DNA hits due to material, $(N-C)/P$. The fit obtained from Figure **??** a) separates the contributions from SCT1 and SCT2; the smoothed contribution from SCT1 is below the dotted fit line, shaded, and the modulated contribution from SCT2 is above.

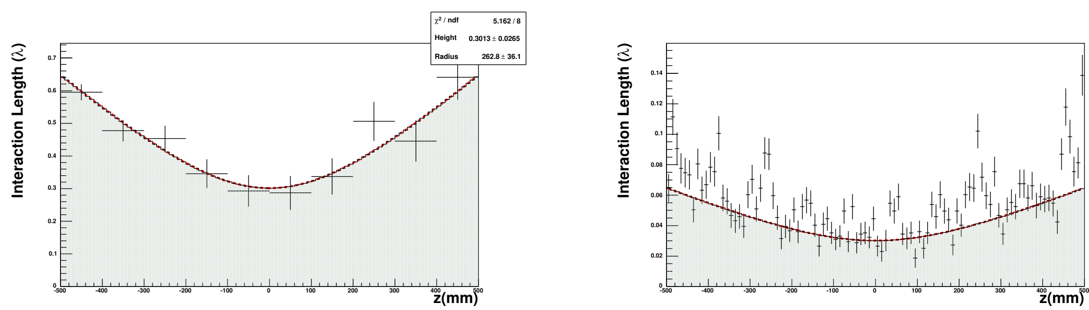

(a) Smoothed material contribution from SCT1 in $-\phi$. $((N-C)/P) * \cdot E/(E+1)$ plotted. 1/sinθ is fitted (dotted red line).

(b) Material contribution from SCT1 and SCT2 in $-\phi$. $(N-C)/P$ plotted. The dotted red line, from fit of a), separates the contribution from the two layers.

Figure 7.22: *The impact of the previous layer on DNA hits at the current layer is estimated. Parameter E is taken from the TMinuit fit of DNA hits in $+\phi$.*

Subtracting the smoothed SCT1 contribution from the overall material contribution results in

Figure **??**. This represents the SCT2 material budget measured in interaction lengths. There is clearly some modulation in the structure. The bottom plot shows the SCT material budget extracted from geantino scans. A promising similarity in modulation is observed.

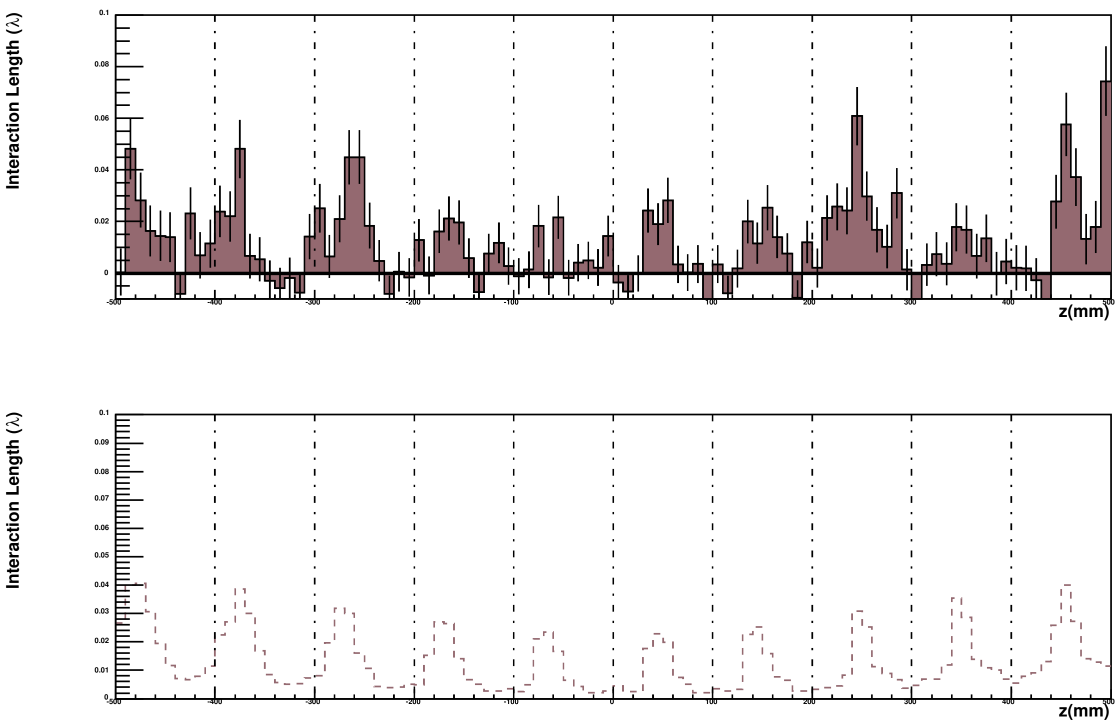

Figure 7.23: *The top plot shows the SCT2 material measured in interaction lengths, extracted from DNA hits in* $-\phi$. $(N-C)/P$ *plotted minus* $1/\sin\theta$ *contribution from SCT1. The bottom plot shows the SCT material budget extracted from geantino scans. A promising similarity in modulation can be seen.*

SCT1 contribution, $E/(E+1)$, is estimated to be $(81\pm3)\%$. This means that $\sim 80\%$ of DNA hits at a certain SCT layer are due to material at the previous layer.

The conversion of SCT material from radiation lengths to interaction lengths is 'checked' by altering the conversion factor in the fit of DNA hits in +ϕ. The χ^2 is minimised using a factor of

0.38 for the material (excluding silicon). The result of the new conversion factor is shown by the dotted back line in Figure **??** and agrees well with the previous method used.

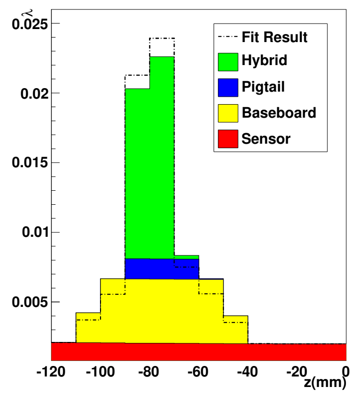

Figure 7.24: *Material contribution of SCT barrel module estimated by minimising the χ^2 of the fit, shown by dotted line. The silicon contribution is considered separate, but the conversion factor for the remaining material is 0.38. This is in good agreement with the previous conversion method, shown in solid color.*

Another confirmation is carried out by a simultaneous fit in $+\phi$ and $-\phi$. Table **??** shows the new fit results. These are in agreement with the previous values from the fit just in $+\phi$. The weight of contribution from the previous layer, given by parameter E, reduces.

Table **??** summarises the new fit coefficients. The correlation between P and E reduces, similarly between P and C, but between A and E the correlation increases, compared with the fit just in $+\phi$. The χ^2 of the fit is 433.1 per 197 degrees of freedom, very similar to the previous fit.

7.2 First look at data

A first look at DNA hits with data is promising. Figure **??** shows a scan of the Inner Detector layers which have bremsstrahlung associated with them through the DNA method. The four SCT barrel

Parameter	Value	Error
C	0.23	0.02
E	3.77	0.38
P	8.28	0.45

Table 7.4: *Parameter values from TMinuit for a simultaneous fit in $+\phi$ and $-\phi$. The values and errors are in good agreement with fit just in $+\phi$.*

Parameter	C	E	P	Global
C	1.000	-0.662	0.170	0.97044
E	-0.662	1.000	-0.839	0.99107
P	0.170	-0.839	1.000	0.98450

Table 7.5: *Parameter Correlation Coefficients from TMinuit for simultaneous fit in $+\phi$ and $-\phi$. The correlation between P and E reduces and between P and C reduces, but between A and E the correlation increases, compared with the fit just in $+\phi$.*

layers are clearly seen in forwards fit. The three pixel layers also acquire DNA hits in backwards fit, once the fitter has a good handle on the track. The position of the bremsstrahlung activity is associated with the closest active layer. It is *not* a free scan of Inner Detector material as one would get from a conversion fitter and so not as impressive as it might look at first.

The key point is that Kalman DNA Fitter works on data in a reliable way and produces results expected from MC.

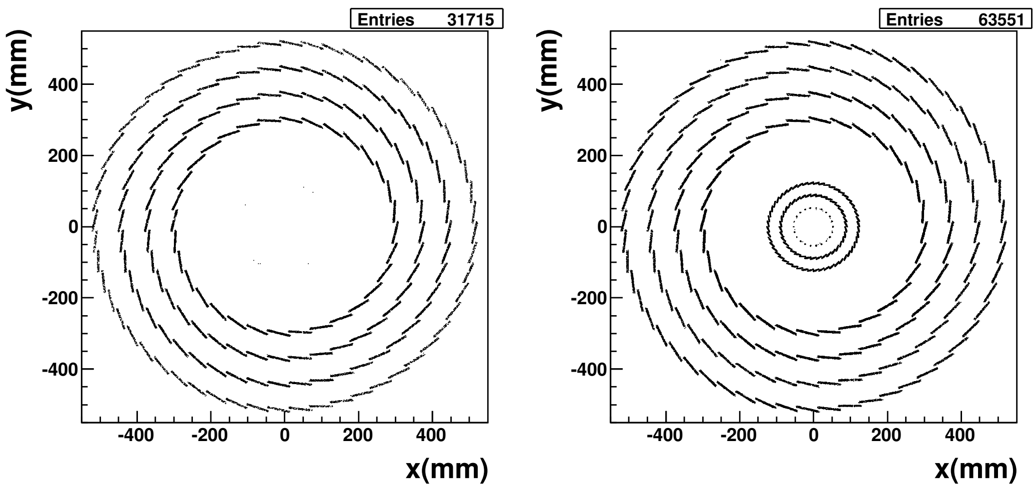

Figure 7.25: *DNA hits in the barrel ($|\eta < 1|$) with about 67k events, minimum bias collision candidates. The four SCT layers show up clearly in forwards fit (left). The three pixel layers also acquire DNA hits in backwards fit (right), once the fitter has a good handle on the track. The position of bremsstrahlung activity is associated to the closest active layer.*

7.3 Summary

Mapping the material in ATLAS will be one of the major tasks at the beginning of data taking.

Dynamic Noise Adjustment (DNA) track fitter finds points on a trajectory where the momentum is changing. Whether this is electron bremsstrahlung or pion scattering, it occurs due to the presence of material. So the more material there is, the more DNA activity will be seen.

I have carried out a feasibility study to show that DNA hits can be used as an indicator of the presence of material. Modulation in the SCT material was observed through DNA hits, which agreed well with the true modulation seen through geantino scans.

With huge statistics soon available with data and a priori symmetries of the detector, this tool could be made quite successful.

'The electron: may it never be of use to anybody'

JJ. Thomson's colleagues

8

Cowboys and Sailors

Prompt J/ψ have a zero pseudo-proper time since they are produced directly from parton interactions, whereas indirect J/ψ primarily come from B-hadron decays with an exponentially decaying pseudo-proper time distribution due to the lifetime of the parent B-hadrons.

The pseudo-proper time distributions shown in Figure **??** of a) $J/\psi \rightarrow \mu\mu$ and b) $J/\psi \rightarrow ee$ give access to a number of important measurements, such as the detector resolution in (pseudo-)proper time, relative yields of prompt and indirect J/ψ , and effective average lifetime of B hadrons. As expected the resolution of electrons is not as good as that for muons. This is due to bremsstrahlung and can be improved, to a certain extent, by using a bremsstrahlung-aware track fitter.

In this chapter I suggest that it is important to consider the kinematics of electron tracks and show that the separation of prompt from indirect J/ψ is improved by consideration of two distinct kinematics of J/ψ decays, known as ‘cowboys’ and ‘sailors’. I will also discuss the feasibility of measuring the ratio of indirect to prompt J/ψ production in the electron channel.

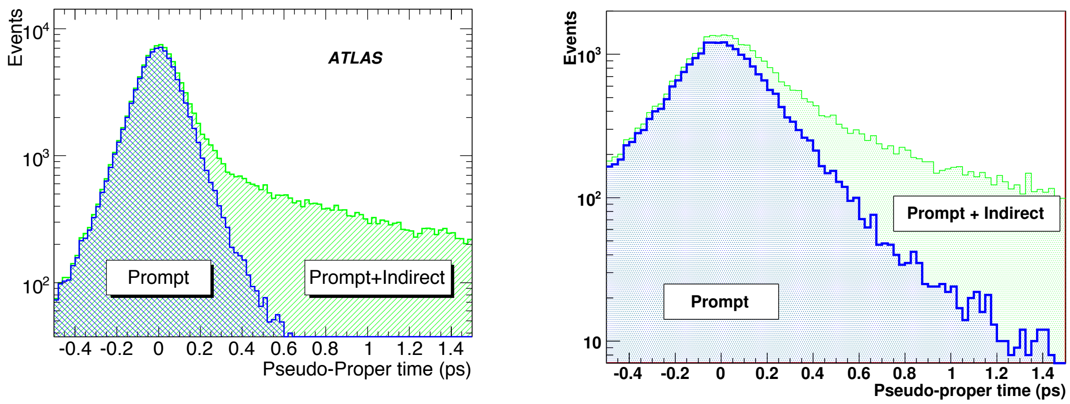

(a) Pseudo-proper time distribution for reconstructed prompt $J/\psi \rightarrow \mu\mu$ and the indirect B-decay $J/\psi \rightarrow \mu\mu$ candidates.[**?**]

(b) Pseudo-proper time distribution for reconstructed prompt $J/\psi \rightarrow ee$ and the indirect B-decay $J/\psi \rightarrow ee$ candidates. Events shown that pass EF in full η range, reconstructed with GXF track fitter.

Figure 8.1: *Pseudo-proper time distributions for $J/\psi \rightarrow \mu\mu$ and $J/\psi \rightarrow ee$.*

8.1 Data Samples

In order to study $J/\psi(ee)$ decay it is necessary to combine prompt and inclusive indirect $J/\psi(ee)$ Monte Carlo data samples. In the absence of an appropriate inclusive sample $bb \rightarrow J/\psi(ee)$, an exclusive sample $B_d \rightarrow J/\psi(ee)K_s^0$ with its cross-section properly rescaled, is used in this study. The momentum distribution of the J/ψ will be different, but the distribution in L_{xy} should not be too different.

8.2 Trigger

The B-Physics trigger EF_MU4_Jpsie5e3_FS is chosen for this study. This FullScan trigger is seeded by a single Level-1 muon and two electromagnetic clusters. In the HLT the muon is confirmed, with a p_T above 4 GeV. The EF requires two electrons (with p_T of at least 5 and 3 GeV) which are combined to pass a J/ψ mass cut. The full scan of the Inner Detector is fairly computer intensive and such triggers are only likely to be available at low LHC luminosities.

One possible source of indirect J/ψ is from B-meson decay as described in Section **??** and shown in Figure **??**. On the opposite side to the J/ψ, two virtual W bosons are produced, which can then decay leptonically. The muons from such decays are independent of the J/ψ but can be used to trigger and thus capture the $J/\psi(ee)$ decay event.

An alternative, the egamma trigger EF_2e5medium trigger, requires 2 electrons with at least 5 GeV that have passed the Medium electron quality criteria. This trigger is expected to have a huge prescale to reduce the big background and so is less attractive.

8.3 Cross-sections

The cross-section ratio of indirect to prompt J/ψ at 10 TeV in the di-muon channel, $bb \rightarrow J/\psi(\mu 2.5\mu 5.5) : pp \rightarrow J/\psi(\mu 2.5\mu 2.5)$, is $\sim$ 1:5 (45 nb:245 nb) [**?**]. The ratio should be similar for J/ψ decay in the di-electron channel. The cross-section for the prompt $pp \rightarrow J/\psi(e3e3)$ sample is quoted as 90 nb [**?**], so a cross-section $\sim$17 nb is expected for $bb \rightarrow J/\psi(e3e3)$.

However the exclusive indirect J/ψ (ee) sample has a generation requirement of a 6 GeV muon, leading to an increased number of events passing the Event Filter. This makes the generation much more efficient, but complicates the calculation of the cross-section associated with this sample.

11% of inclusive b-decays have a muon present in the final state. Table **??** shows the cross-sections for indirect J/ψ (ee) production with a muon of more than 0 GeV, 3 GeV and 6 GeV present. Therefore if an indirect J/ψ has a muon present, $\sim 5\%$ of such muons will have a p_T greater than 6 GeV. Combining the above factors, the cross-section for the exclusive J/ψ (e3e3) MC data sample such that it can be considered as inclusive J/ψ (e3e3), with a 6 GeV trigger muon, is estimated to be 17 nb$\times$11% $\times$ 5% $\simeq$0.10 nb

About 64% of the indirect sample events pass Level-1 trigger and then $\sim$ 44% that have passed Level-1 go on to pass the Event Filter (see Table **??**). So the effective cross-section of the indirect sample after the Event Filter is 0.10 nb$\times$64% $\times$ 44% $\simeq$0.03 nb.

Muon Pt requirement (GeV)	σ(nb)
0	387
3	68
6	21

Table 8.1: *Cross-sections for indirect J/ψ MC sample, with different muon p_T requirements. These cross-sections indicate that if an indirect J/ψ sample has a muon present, then $\sim 5\%$ (21/387) of such muons will have a p_T greater than 6 GeV.*

For the prompt sample, as there is no physical reason for the trigger muon to be correlated to the J/ψ, the muon requirement is removed altogether. The sample is then treated as if all events pass the Level-1 $\mu 4$ trigger. Some basic features of the Event Filter trigger are emulated. The resulting cross-section is therefore reduced, effectively increasing the size of the prompt sample. With full simulation only 330 events passed the Level-1 trigger, out of the sample size of 180k, so by adding the muon requirement the effective cross-section reduces from 90 nb to $\sim$0.17 nb. About 30% of the prompt sample events that pass Level-1 trigger go on to pass the Event Filter (see Table **??**). So the effective cross-section of the prompt J/ψ after the Event Filter reduces to 0.17 nb$\times$30% $\simeq$0.05 nb.

The two samples are therefore combined in the indirect:prompt ratio of 0.03 nb:0.05 nb=3:5

after Event Filter. I will then refer to this value of the ratio as ‘input’.

8.4 Background

The main background for this study is expected to come from jets. The naming scheme for the jet MC samples is such that JX denotes the parton p_T range i.e. J1 refers to 17< p_T <35 GeV, J2 refers to 35< p_T <70 GeV and J3 refers to 70< p_T <140 GeV. Table **??** lists the jet datasets, detailing cross-sections, corresponding integrated Luminosity and the number of events that pass the Level-1 and Event Filter triggers. Table **??** shows the number of events for the different background samples (normalised to the same integrated Luminosity of 1 pb^{-1}) that pass a cut on the reconstructed J/ψ mass and then tighter and tighter electron quality criteria.

The main background appears to be from low p_T jets (J1 and J2). The bb J2 sample has one event (out of 20k events) passing the requirement for one electron to pass Loose quality criteria and the other Medium. It is likely that this event is in fact a J/ψ event and not combinatorial background.

With both electrons required to pass the Medium electron quality criteria the background should be significantly reduced. However the background MC statistics are insufficient to allow a clear understanding of the remaining background with the higher electron quality criteria (see Table **??**).

500k Minimum bias events were also studied. Only one event passed the Event Filter, which then did not pass the J/ψ mass window cut.

The net result of the background study is that there is not enough statistics to draw any quantitative conclusions on the rate of background events. However it shows that the level of the background should be manageable, but is likely to have large systematic errors.

In the absence of adequate background distributions our studies of the measurement of indirect-to-prompt $J/\psi \rightarrow ee$ production are effectively feasibility studies. With real data, background events – as well as signal events – will be produced in correct proportions and this will make such measurements significantly more challenging. With real data, the background can be studied to see how jets fake electrons, with and without the trigger requirement, so as to be able to look at electron candidates in jets.

Process Name	Dataset	σ (nb)	N_e	$\mathscr{L}(pb^{-1})$	Pass L1	Pass EF
`PythiaB_bb_J2`	108469	4041	20k	0.005	1573	109
`PythiaB_bb_J3`	108470	309	20k	0.065	3157	630
`PythiaB_cc_J2`	108474	9278	20k	0.002	816	62
`PythiaB_cc_J3`	108475	689	20k	0.0290	1820	359
`J1_pythia_jetjet`	105010	362972	70k	0.0002	26161	775
`J2_pythia_jetjet`	105011	57068	80k	0.0014	50203	4361
`J3_pythia_jetjet`	105012	3280	75k	0.02	57238	13032
`J4_pythia_jetjet`	105013	35	70k	2.0	56860	23884
`J5_pythia_jetjet`	105014	5	80k	16	66294	36601
direct J/ψ e3e3	105751	90	180k	2	330	102
Indirect $\mu 6$ J/ψ e3e3		0.1	90k	900	57866	25566

Table 8.2: *Background and signal samples. JX denotes the parton p_T range of each jet sample. This table shows, for each MC dataset, the cross-section (σ), number of events (N_e), luminosity ($\mathscr{L}$) and number of events that pass Level-1 trigger (Pass L1) and Event Filter (Pass EF).*

Process	Pass EF	Pass Mcut	L	LL	M	LM	MM
`bb_J2`	(22 ± 2) k	(3.2 ± 0.8) k	(1.4 ± 0.5) k	400 ± 280	200 ± 200	200 ± 200	0
`bb_J3`	(97 ± 0.4) k	(0.9 ± 0.1) k	170 ± 50	15 ± 15	15 ± 15	0	0
`cc_J2`	(31 ± 4) k	(2.5 ± 1.1) k	0	0	0	0	0
`cc_J3`	(12 ± 0.6) k	(1.2 ± 0.7) k	172 ± 80	35 ± 35	0	0	0
`J1_jetjet`	(390 ± 14) k	(53 ± 5) k	(22 ± 3) k	(4.5 ± 1.5) k	(3.5 ± 1.3) k	(1.5 ± 0.9) k	0
`J2_jetjet`	(3100 ± 45) k	(300 ± 15) k	(105 ± 85) k	(20 ± 3.7) k	(12 ± 3) k	(3.5 ± 1.5) k	0
`J3_jetjet`	(650 ± 6) k	(40 ± 1.5) k	(9 ± 0.7) k	800 ± 200	550 ± 150	100 ± 70	0
`J4_jetjet`	(12 ± 0.1) k	550 ± 15	55 ± 5	5 ± 2	1.5 ± 0.9	0.5 ± 0.5	0
`J5_jetjet`	(2 ± 0.01) k	60 ± 2	4 ± 0.5	0.05 ± 0.05	0.3 ± 0.1	0	0
direct J/ψ	50 ± 5	37 ± 4	37 ± 4	28 ± 4	36 ± 4	28 ± 4	22 ± 3
Indirect $\mu 6$ J/ψ	28 ± 0.2	19 ± 0.1	17 ± 0.1	12 ± 0.1	15 ± 0.1	11 ± 0.1	7.6 ± 0.1

Table 8.3: *Background and signal samples normalised to integrated Luminosity of 1 pb^{-1}. This table shows the number of events that pass Event Filter (Pass EF), the number of events with reconstructed J/ψ mass between 1.5 and 4.0 GeV with vertexing χ^2 <50 (Pass Mcut) and then the number of events that pass successively strict electron quality criteria. L=One electron candidate pass Loose cuts. LL=Both electron candidates pass Loose cuts. M=One electron candidate pass Medium cuts. LM=One electron candidate pass Medium cuts and the other pass Loose cuts. MM=Both electron candidates pass Medium cuts.*

8.5 L_{xy} study

L_{xy} is the distance of the secondary vertex from the primary vertex in the transverse plane projected onto the J/ψ momentum direction, as illustrated in Figure ??. It can be used to distinguish between prompt and indirect J/ψ. The prompt J/ψ has a true zero L_{xy} and B-hadron decays into $J/\psi + X$ has an exponentially decaying L_{xy} distribution due to the non-zero lifetime of the parent.

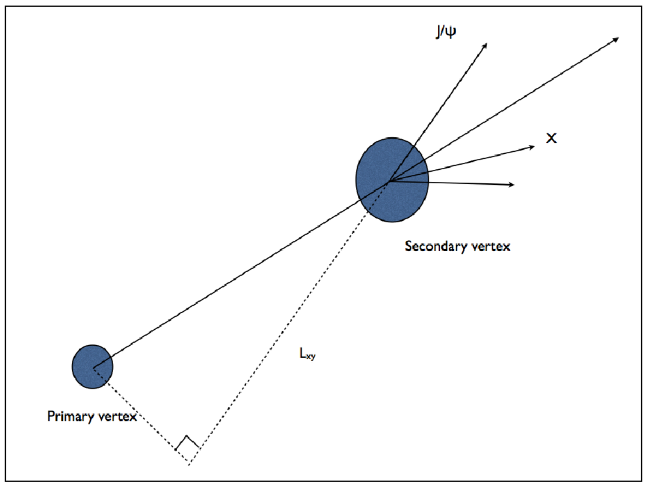

Figure 8.2: *Graphical representation of L_{xy}, the distance of the secondary vertex from the primary vertex in the transversate plane projected onto the J/ψ direction.*

A feature emerges if one considers the difference in the azimuthal angle, ϕ, between the positive and negative electron. Reconstructed L_{xy} is seen to depend upon track kinematics. The two situations are defined depending on the difference between the track ϕ of the positive electron (ϕ_+) and negative electron (ϕ_-).

$$\text{‘Cowboy’} : \sin(\phi_+ - \phi_-) < 0 \tag{8.1}$$

$$\text{‘Sailor’} : \sin(\phi_+ - \phi_-) > 0 \tag{8.2}$$

The sine of the difference in angle is used rather than an absolute difference, due to the ATLAS definition of ϕ, which goes between $\pm\pi$. A small angular difference between the two tracks can therefore result in an absolute difference above 2π.

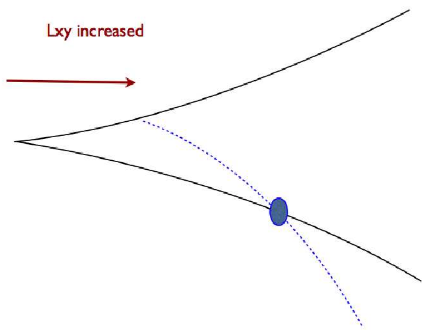

(a) Sailor: positive difference in ϕ between the positive and negative electron. The tracks are divergent as they progress, in the shape of sailor legs (see Figure ??).

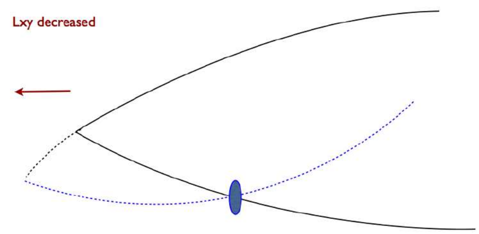

(b) Cowboy: negative difference in ϕ between the positive and negative electron. The tracks are convergent as they progress, in the shape of cowboy legs (see Figure ??).

Figure 8.3: *Graphical representation of possible explanation for L_{xy} shift seen for cowboys and sailors.*

When the L_{xy} distributions for prompt $J/\psi \to ee$ are plotted separately for cowboys and sailors it can be seen that they are asymmetric. Sailors have a tail on the right, indicating a tendency for L_{xy} to be increased and cowboys have a tail on the left, indicating a tendency for L_{xy} to be decreased. Also the peak position shifts from zero. For sailors the peak position becomes positive and for cowboys, negative. This shift in peak position and asymmetric tails I shall call the 'cowboy and sailor effect'. This is shown in Figure **??** a) together with the fits using an asymmetric Gaussian function. It is noteworthy that the left hand resolutions for cowboys are very similar to the right hand sailor resolutions, and vice versa. The similarity between the two cases is shown by reflecting one distribution, as shown in Figure **??** b).

Figure **??** shows two $J/\psi \to$ ee events displayed using ATLAS 'virtual point 1'(vp1) event display software [?]. The sailor event shown is reconstructed with negative L_{xy} ($L_{xy} = -0.525$ mm). The tracks can be seen to be divergent as they progress. The cowboy event is reconstructed with

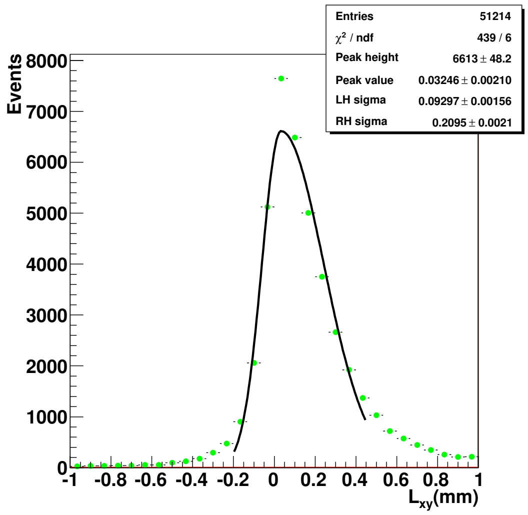

(a) Sailors :$\sin(\phi_+ - \phi_-) > 0$

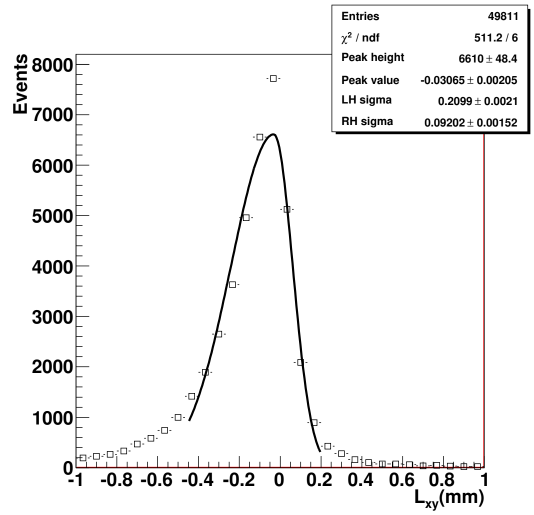

(b) Cowboys :$\sin(\phi_+ - \phi_-) < 0$

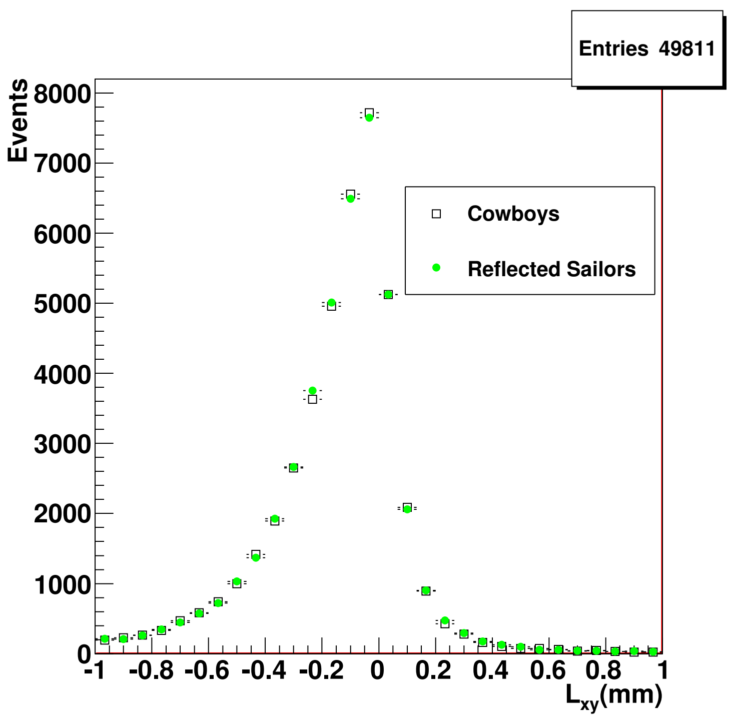

(c) Reflecting the sailor distribution highlights the similarity of the two distributions.

Figure 8.4: *Reconstructed L_{xy} distributions for cowboys and sailors. If one considers the difference in ϕ between the positive and negative electron an asymmetry is apparent. Electron tracks having positive difference in ϕ have a tendency of increasing reconstructed L_{xy}. Electron tracks having negative difference in ϕ have a tendency of reducing L_{xy}.*

positive L_{xy} (L_{xy}=0.533 mm). The tracks can be seen to be convergent as they progress, in the shape of cowboy legs and hence the name.

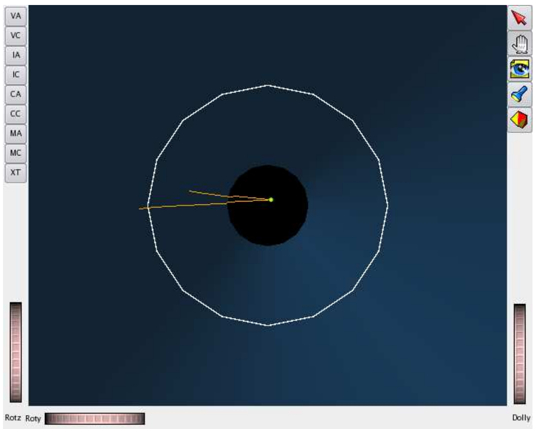

(a) Sailor: $L_{xy} = -0.525$ mm

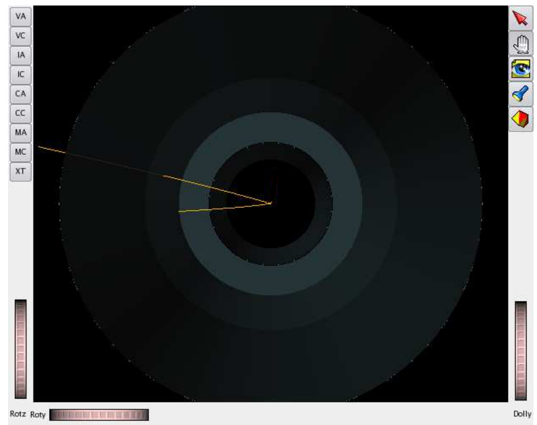

(b) Cowboy: L_{xy}=0.533 mm

Figure 8.5: *Two $J/\psi \to ee$ events displayed using ATLAS 'virtual point 1'(vp1) event display software. The event shown on the left is known as a sailor due to positive difference in ϕ between the positive and negative electron and is reconstructed with negative L_{xy}. The tracks can be seen to be divergent as they progress. The event shown on the right is known as a cowboy due to negative difference in ϕ between the positive and negative electron and is reconstructed with positive L_{xy}. The tracks can be seen to be convergent as they progress, in the shape of cowboy legs.*

Monte Carlo truth is consulted to confirm that bremsstrahlung causes the tails in the L_{xy} distributions for cowboys and sailors. The left hand distributions in Figure **??** show L_{xy} when bremsstrahlung has had a large effect on both electrons. The right hand distributions in Figure **??**, show L_{xy} when bremsstrahlung has had a small effect on both electrons. Not surprisingly, when there has been little bremsstrahlung the distributions look more Gaussian and more symmetric.

Reconstructed L_{xy} distributions for two track fitters, GXF and Aggressive full fit DNA, are shown in Figure **??**. Both electrons are required to pass Medium quality criteria. The cowboy and sailor effect is certainly seen with both fitters, in both the barrel region and at large $|\eta|$. GXF resolution is 0.17 mm in the barrel. Aggressive DNA improves the resolution to 0.14 mm in

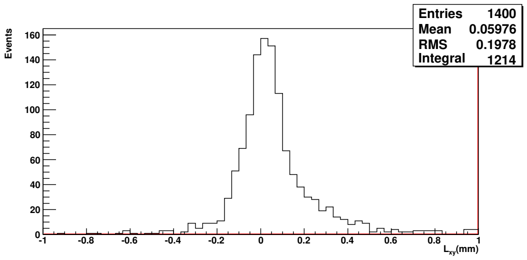

(a) Sailors: $z < 10\%$

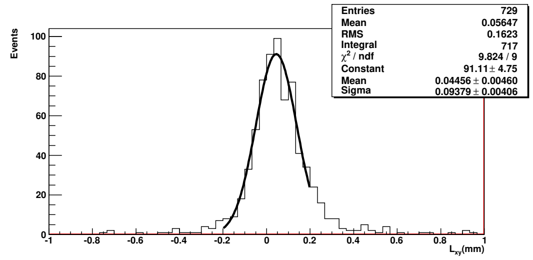

(b) Sailors: $z > 90\%$

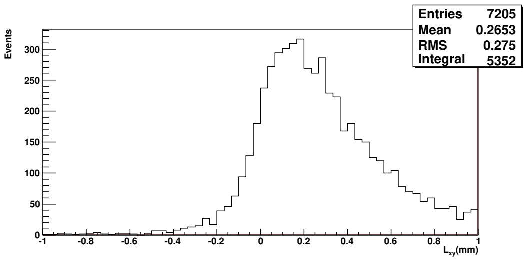

(c) Sailors: maximum Brem $> 25\%$

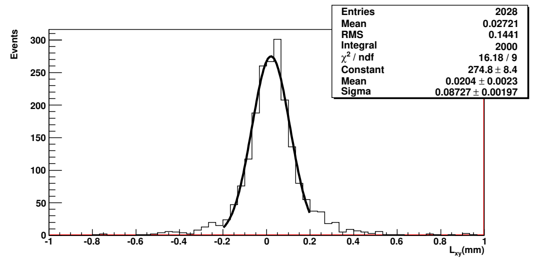

(d) Sailors: maximum Brem $< 10\%$

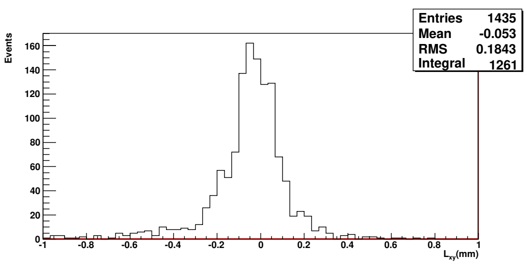

(e) Cowboys: $z < 10\%$

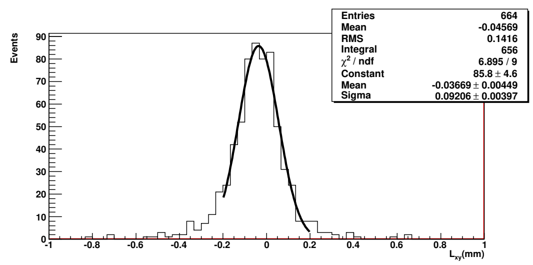

(f) Cowboys: $z > 90\%$

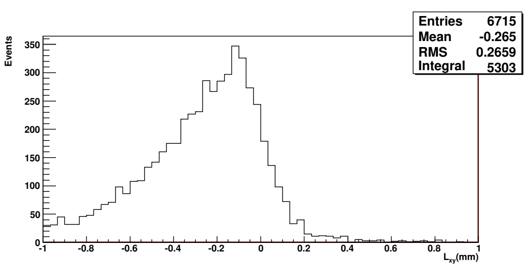

(g) Cowboys: maximum Brem $> 25\%$

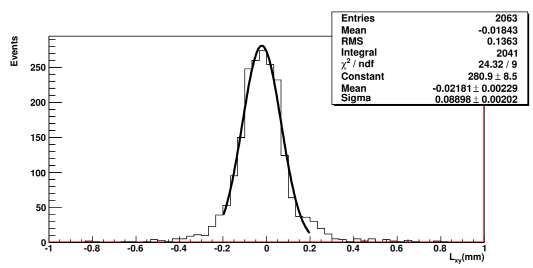

(h) Cowboys: maximum Brem $< 10\%$

Figure 8.6: *L_{xy} distributions for cowboys and sailors. The left hand distributions show L_{xy} when bremsstrahlung has had a large effect on both electrons: a) and e) when truth energy retained by both tracks is less than 10%, c) and g) when the maximum bremsstrahlung on track is greater than 25%. The right hand distributions show L_{xy} when bremsstrahlung has had a small effect on both electrons: b) and f) when truth energy retained by both tracks is greater than 90%, d) and h) when the maximum bremsstrahlung on track is less than 10%. Not surprisingly, when there has been little bremsstrahlung the distributions look more Gaussian.*

the barrel but there are still visible differences between cowboys and sailors. At large $|\eta|$ GXF resolution is 0.29 mm which improves to 0.19 mm using Aggressive DNA.

Reconstructed L_{xy} distributions where both electrons are required to pass Tight quality criteria are shown in Figure **??**. The barrel resolution using the Aggressive DNA fitter is improved further to 0.13 mm. The large $|\eta|$ region suffers from a significant reduction in statistics with such Tight electron quality criteria requirements such that any benefits are outweighed.

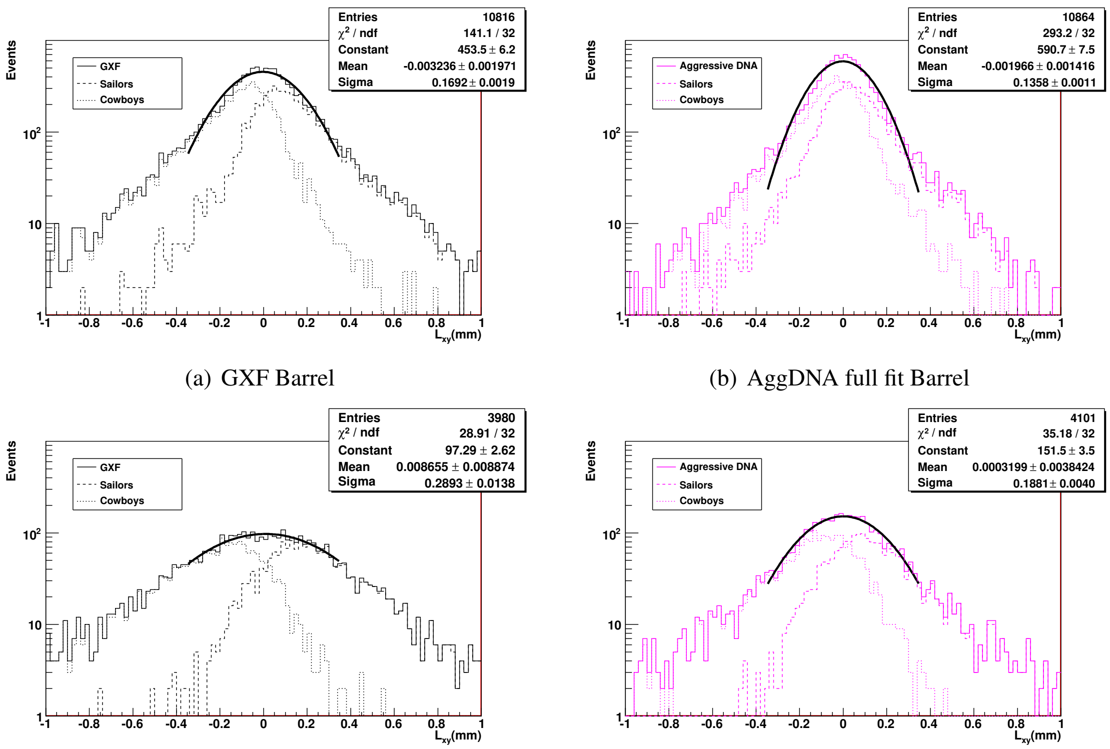

(a) GXF Barrel

(b) AggDNA full fit Barrel

(c) GXF $|\eta| > 1$

(d) AggDNA full fit $|\eta| > 1$

Figure 8.7: *Reconstructed L_{xy} for two track fitters, GXF and Aggressive DNA, where both electrons are required to pass Medium quality criteria. Cowboy and sailor effect is certainly seen. Aggressive DNA improves resolution but there are still visible differences between cowboys and sailors.*

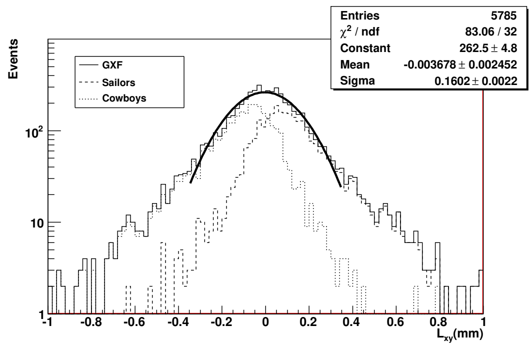

(a) GXF Barrel

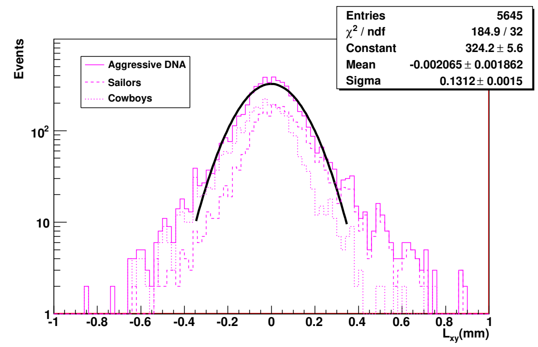

(b) AggDNA full fit Barrel

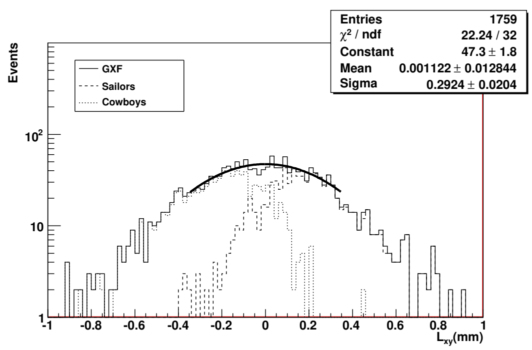

(c) GXF $|\eta| > 1$

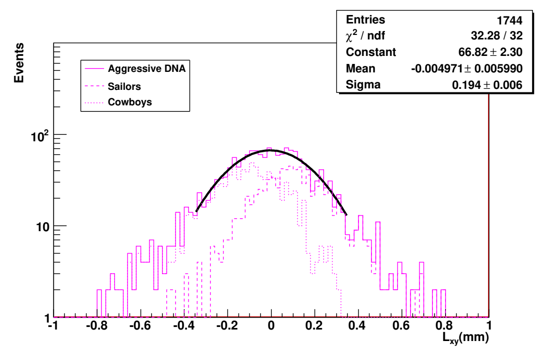

(d) AggDNA full fit $|\eta| > 1$

Figure 8.8: *Reconstructed L_{xy} for two track fitters, GXF and Aggressive DNA, where both electrons required to pass Tight quality criteria. Cowboy and sailor effect is still seen, but is much reduced.*

8.6 Separating prompt and indirect J/ψ

By making a cut on the pseudo-proper time, one can separate most of the prompt J/ψ from the indirect J/ψ sample (or vice-versa).

Pseudo-proper time, t, is defined as

$$t = \frac{L_{xy} \cdot M_{J/\psi}}{p_{T(J/\psi)} \cdot c} \tag{8.3}$$

where $M_{J/\psi}$ and $p_{T(J/\psi)}$ represent the J/ψ invariant mass and transverse momentum respectively, c is the speed of light in vacuum, and L_{xy} is the measured transverse decay length. Transverse L_{xy} is used because of its better resolution compared with the 3D decay length L_{xyz}.

We define purity for prompt J/ψ as the ratio of the total number of prompt J/ψ candidates to the total number of events, retained below a particular pseudo-proper time cut, t_{cut},

$$\text{Purity}(t < t_{cut}) = \frac{N_{J/\psi}(t < t_{cut})}{N_{Events}(t < t_{cut})} \tag{8.4}$$

For purity of the indirect J/ψ candidates, we use the same definition but with a reversal in the direction of the cut, retaining only those *above* a certain value of t_{cut}.

We define efficiency for prompt J/ψ as the ratio of the total number of prompt J/ψ candidates retained below a particular pseudo-proper time cut and the total number of prompt J/ψ candidates.

$$\text{Efficiency}(t < t_{cut}) = \frac{N_{J/\psi}(t < t_{cut})}{N_{J/\psi}} \tag{8.5}$$

Using the default track fitter, GXF, a pseudo-proper time cut of t_{cut} >0.30 ps allows one to retain prompt J/ψ with the purity and efficiency of 91%, illustrated by the crossing point in Figure **??** a). Conversely for separating indirect J/ψ, with a pseudo-proper time cut of t_{cut} <0.30 ps indirect J/ψ are retained with a purity of 70% and efficiency of 69%, illustrated in Figure **??** b).

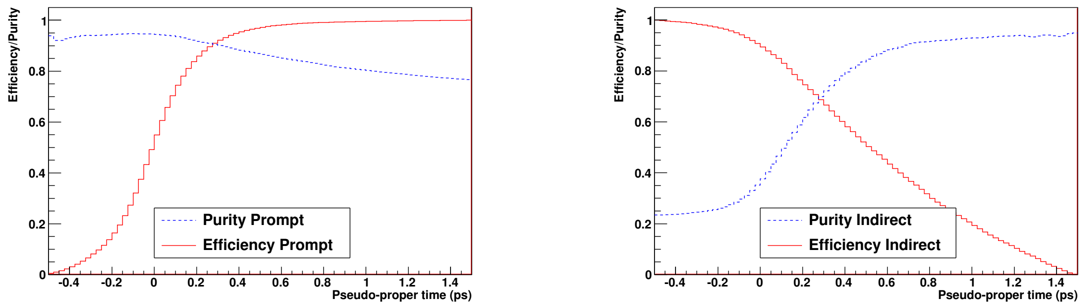

(a) Prompt $J/\psi \to ee$ candidates

(b) Indirect $J/\psi \to ee$ candidates

Figure 8.9: *Efficiency (solid line) and purity (dotted line) for a) prompt $J/\psi(ee)$ candidates and b) indirect $J/\psi(ee)$ candidates as a function of the pseudo-proper time cut. The default fitter, GXF, was used to reconstruct the events. Both electrons were required to be in barrel and pass Medium quality criteria.*

In comparison, when looking at $J/\psi(\mu\mu)$, shown in Figure **??**, a pseudo-proper time cut of 0.2 ps allows one to retain prompt J/ψ with the efficiency of 93% and the purity of 97% or conversely, indirect J/ψ with efficiency of 75% with 61% purity [**?**].

The prompt and indirect samples can be separated into cowboys and sailors. Due to the asymmetric resolutions in L_{xy}, this separation may be used to improve the efficiency and/or pruity of the selection of prompt and indirect J/ψ. The efficiency and purity of extracting prompt candidates is shown in Figure **??**. The purity of extracting sailors is improved for all pseudo-proper time cuts. The efficiency of extracting cowboys is improved slightly since advantage is taken of the left hand L_{xy} tail.

A greater improvement is seen in Figure **??**. The purity of extracting indirect cowboys shows a marked improvement compared with no kinematic separation.

The purity vs efficiency distribution in Figure **??** shows that cowboys have an improved purity and efficiency compared to all events considered together. So, a very simple cut on kinematics yields a significant improvement for extracting indirect J/ψ.

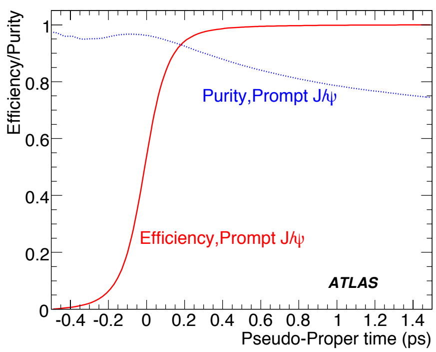

(a) Prompt $J/\psi \rightarrow \mu\mu$ candidates

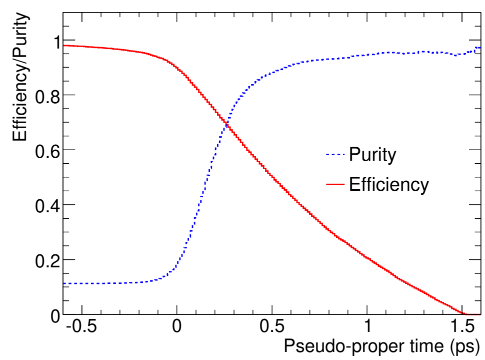

(b) Indirect $J/\psi \rightarrow \mu\mu$ candidates

Figure 8.10: *Efficiency (solid line) and purity (dotted line) for a) prompt $J/\psi(\mu\mu)$ candidates and b) indirect $J/\psi(\mu\mu)$ candidates as a function of the pseudo-proper time cut. [**?**]*

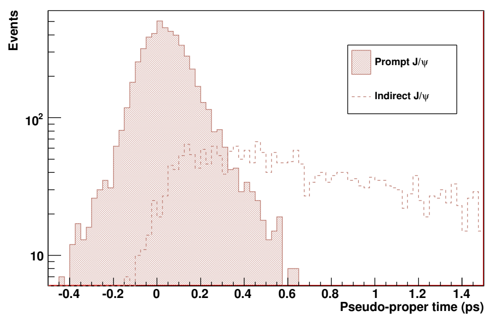

(a) J/ψ(ee) Sailors

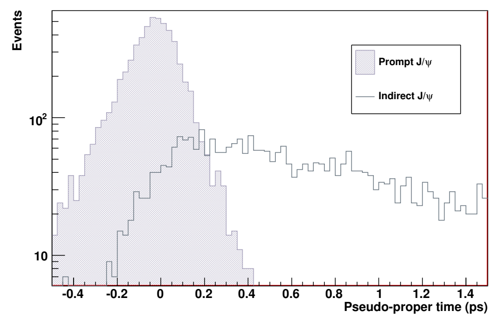

(b) J/ψ(ee) Cowboys

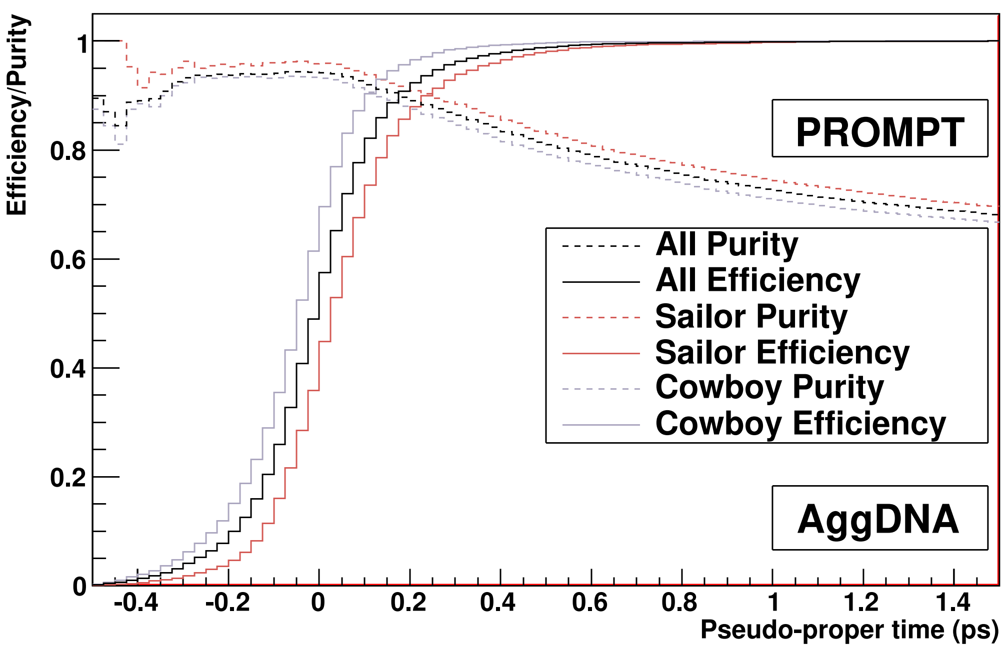

Figure 8.11: *Efficiency (solid line) and purity (dotted line) for prompt $J/\psi(ee)$ candidates in the barrel, with both electrons passing Medium quality criteria. The bremsstrahlung-aware Aggressive DNA fitter was used to reconstruct the events.*

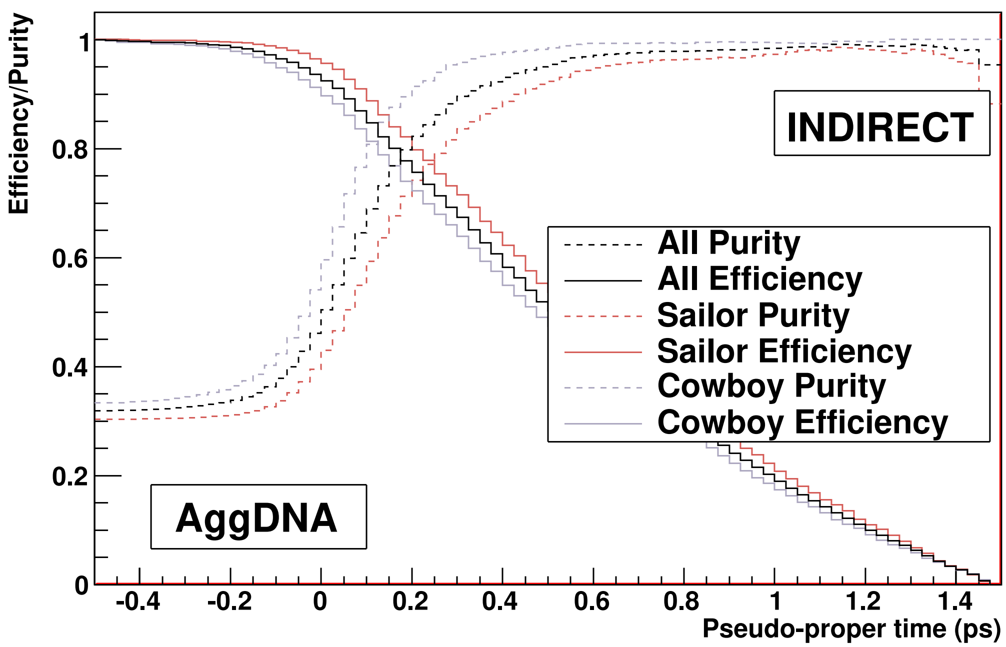

Figure 8.12: *Efficiency (solid line) and purity (dotted line) for indirect $J/\psi(ee)$ candidates in the barrel, with both electrons passing Medium quality criteria. The bremsstrahlung-aware Aggressive DNA fitter was used to reconstruct the events.*

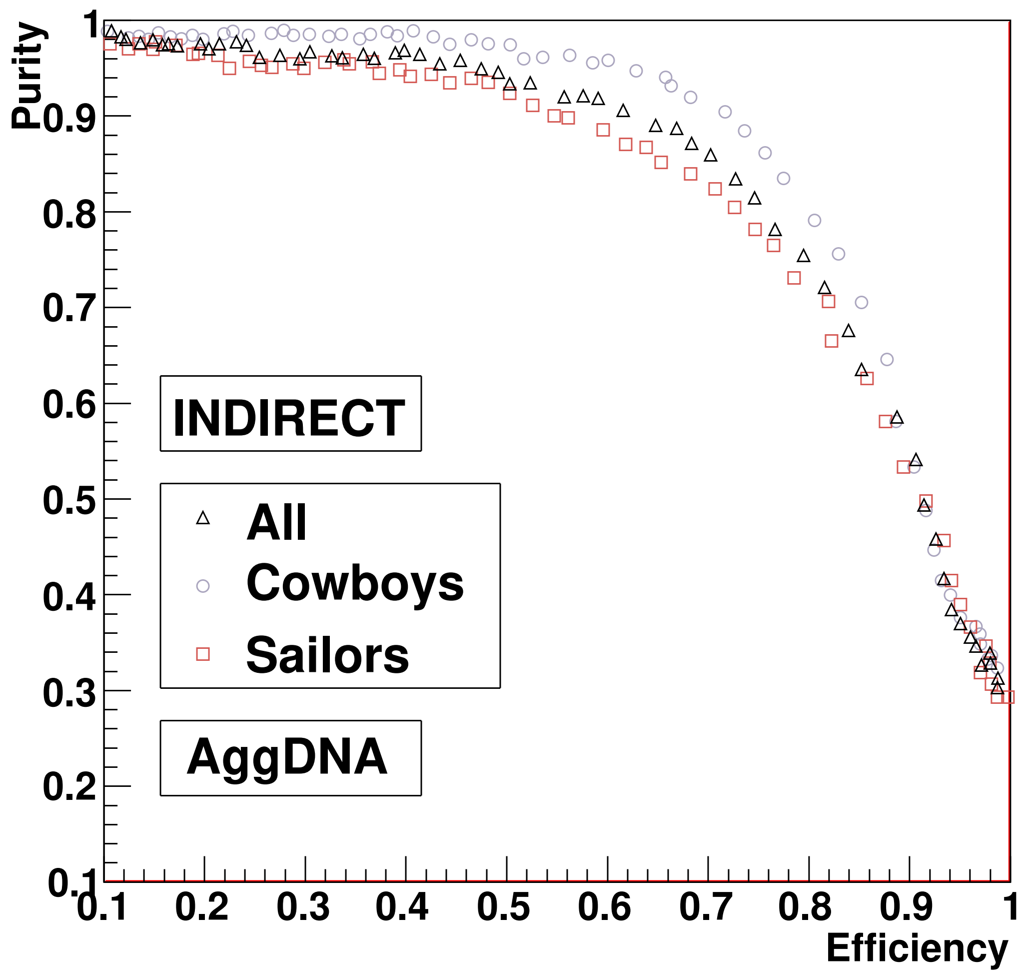

Figure 8.13: *Purity vs Efficiency for Indirect J/ψ candidates, using Aggressive DNA fitter and separated into cowboys and sailors. A marked improvement is available for extracting indirect J/ψ if cowboys are selected.*

8.7 Feasibility study for the measurement of the ratio of indirect to prompt J/ψ.

Various Tevatron measurements over the last few years have unveiled many interesting features of heavy quark production in high energy hadronic collisions. However, many questions still remain unanswered, and data obtained by the LHC collaborations should be able to shed new light on these processes in the new energy regime. Measurement of the ratio of indirect to prompt J/ψ should be possible with very early ATLAS data.

The feasibility of measuring the ratio

$$\mathscr{R} = \frac{d\sigma(bb \to J/\psi)}{d\sigma(pp \to J/\psi)} \tag{8.6}$$

in the electron decay channel is described in this section. Measurement of the ratio should be possible with early ATLAS data. Understanding of the trigger and reconstruction efficiencies and determination of cross-sections may take more time.

A function representing the true proper time distribution for J/ψ must include a delta-function to describe the prompt contribution and a (normalised) exponential term to describe the indirect contribution. The sum of these two terms is then smeared with a resolution function $r(t)$.

Such a function is

$$f(t) = C_1 \cdot r(t) \otimes [\delta(t) + \mathscr{R} \cdot \Gamma \cdot \exp(-\Gamma t)] \tag{8.7}$$

where C_1 is the normalisation coefficient common to both terms and Γ the slope of the exponential. The ratio of indirect to prompt J/ψ is thus given by $\mathscr{R}$.

For muons, the resolution function can successfully be treated as a single symmetric Gaussian [**?**],

$$r(t) = \frac{1}{\sqrt{2\pi}\sigma} \cdot \exp\left(\frac{-t^2}{2\sigma^2}\right) \tag{8.8}$$

resulting in the pseudo-proper time distribution to be fitted by the function

$$\begin{aligned} f(t) &= \frac{C_1}{\sqrt{2\pi}\sigma}\cdot\exp\Big(-\frac{t^2}{2\sigma^2}\Big) \\ &+ \mathscr{R}\cdot C_1\cdot\Gamma\cdot\exp\Big(\frac{\Gamma^2\sigma^2}{2}-\Gamma t\Big)\frac{1}{2}\Big[1+\mathrm{erf}\Big(\frac{t-\Gamma\sigma^2}{\sqrt{2}\sigma}\Big)\Big] \end{aligned} \tag{8.9}$$

where erf is the error function and σ the resolution of the Gaussian.

However for electrons this resolution function is insufficient. The resolution function for electrons is considered to be a normalised sum of two Gaussians, with resolutions σ_1 and σ_2. The second Gaussian, defined as the broader of the two, is weighted by a factor C_2. The resolution term is then

$$r(t) = \frac{1}{\sqrt{2\pi}(1+C_2)}\left[\frac{1}{\sigma_1}\cdot\exp\left(\frac{-t^2}{2\sigma_1^2}\right)+\frac{C_2}{\sigma_2}\cdot\exp\left(\frac{-t^2}{2\sigma_2^2}\right)\right] \tag{8.10}$$

The pseudo-proper time distribution for J/ψ (ee) candidates is plotted, where both electrons are in the barrel ($\eta < 1$) and pass Medium electron quality criteria, to reduce background. The distribution is fitted with function (**??**) using resolution function (**??**) and is shown in Figure **??**. The value $\mathscr{R}$, of the ratio of indirect to prompt J/ψ, obtained from the fit, 0.640 ± 0.015, is close to the input value of 0.600 ± 0.010 (as described in Section **??**). The value of the normalisation coefficient, C_1, which is the integral of the prompt contribution, returns a fit value of 11910 ± 147 which is in reasonable agreement with the input value of 12380 ± 111. The slope of the exponential, Γ, obtained from the fit is larger than Γ_{B0}=0.65 ps^{-1} [**?**]. This can be explained by the fact that L_{xy} is pseudo-proper time rather than proper time [1)].

To check the quality of the fit purely on the prompt contribution, function (**??**) using resolution function (**??**) is shown in Figure **??**. Value C_1, the estimated integral of the prompt contribution, is improved. Γ, the slope of the exponential, is reduced as expected. The resolutions of the double

[1)] The difference is due to the approximation in pseudo-proper time of using the J/ψ mass and momentum rather than the b quark values required for proper time calculations. A correction can be made to convert the measurement, but this is not the parameter of interest in this study.

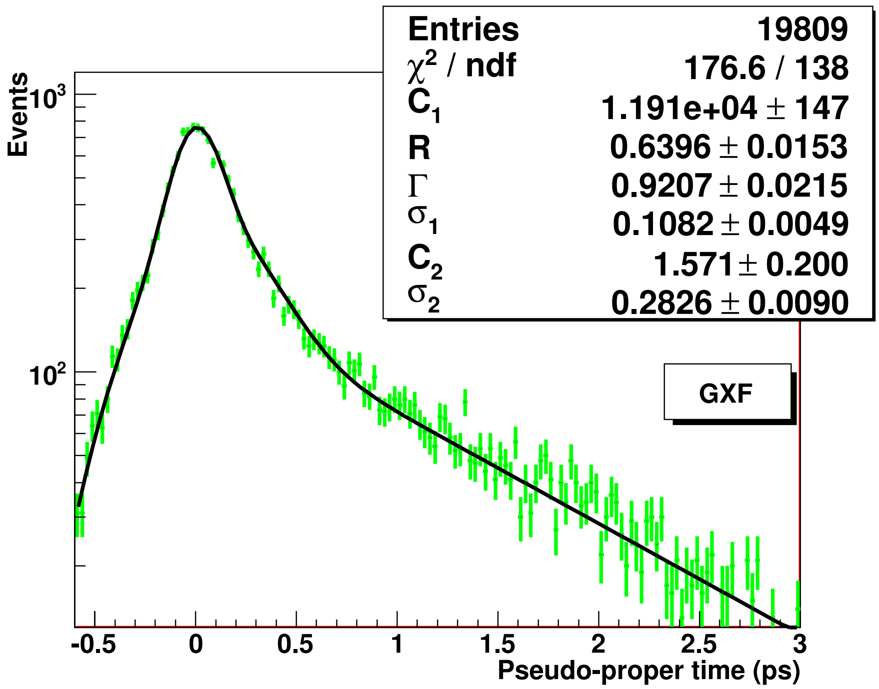

Figure 8.14: *Pseudo-proper time distribution for all events in the barrel, fitted with function (**??**) and resolution function (**??**). GXF fitter used. The resolution function used is a normalised sum of two Gaussians, with resolutions σ_1 and σ_2. The second Gaussian, defined as the broader of the two, is weighted by a factor C_2. The value of the normalisation coefficient, C_1, is the estimated integral of the prompt contribution. Γ is the slope of the exponential and $\mathscr{R}$ the ratio of indirect to prompt J/ψ.*

Gaussian contribution, σ_1 and σ_2, are in reasonable agreement with previous values from combined prompt and indirect sample, despite the reduced value of weight factor C_2. The expected value of the ratio is zero and the fit returns 0.021 ± 0.007, a satisfyingly small value, justifying the choice of the resolution function.

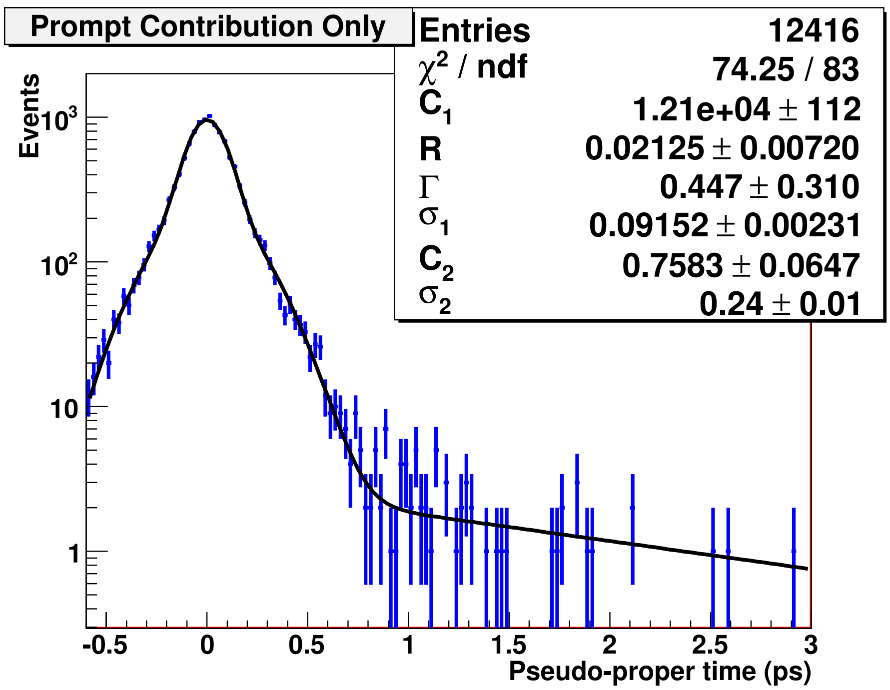

Figure 8.15: *Pseudo-proper time distribution for only prompt events in the barrel, fitted with function (??) and resolution function (??). This fit is performed to check the quality of the fit on just the prompt contribution. GXF fitter used. The resolution function used is a normalised sum of two Gaussians, with resolutions σ_1 and σ_2. The second Gaussian, defined as the broader of the two, is weighted by a factor C_2. The value of the normalisation coefficient, C_1, is the estimated integral of the prompt contribution. Γ is the slope of the exponential and $\mathscr{R}$ the ratio of indirect to prompt J/ψ.*

The main reason for a large second Gaussian in the resolution function is electron bremsstrahlung. In order to demonstrate this link events are selected from truth where both electron candidates retain more than 80 % of their initial energy, to represent events with little bremsstrahlung effects. The pseudo-proper time distribution is shown in Figure **??**. The non-bremsstrahlung-aware Global χ^2 Fitter (GXF) is used since a bremsstrahlung-aware fitter would reduce effects due to bremsstrahlung. The weight of the second Gaussian, C_2, is reduced in the case of events with little bremsstrahlung (C_2=0.343 $\pm$ 0.273) compared with the case when all events are considered (C_2=1.331 $\pm$ 0.187) in Figure **??**. Reassuringly, the value of the two Gaussian resolutions, σ_1 and σ_2, remain consistent, as does the value of Γ.

From previous studies it is expected that the resolution can be improved by using a bremsstrahlung-aware fitter. Figure **??** shows that indeed the resolutions and χ^2 improves, as does the estimation of the number of prompt J/ψ candidates C_1, whilst the ratio $\mathscr{R}$ remains essentially stable.

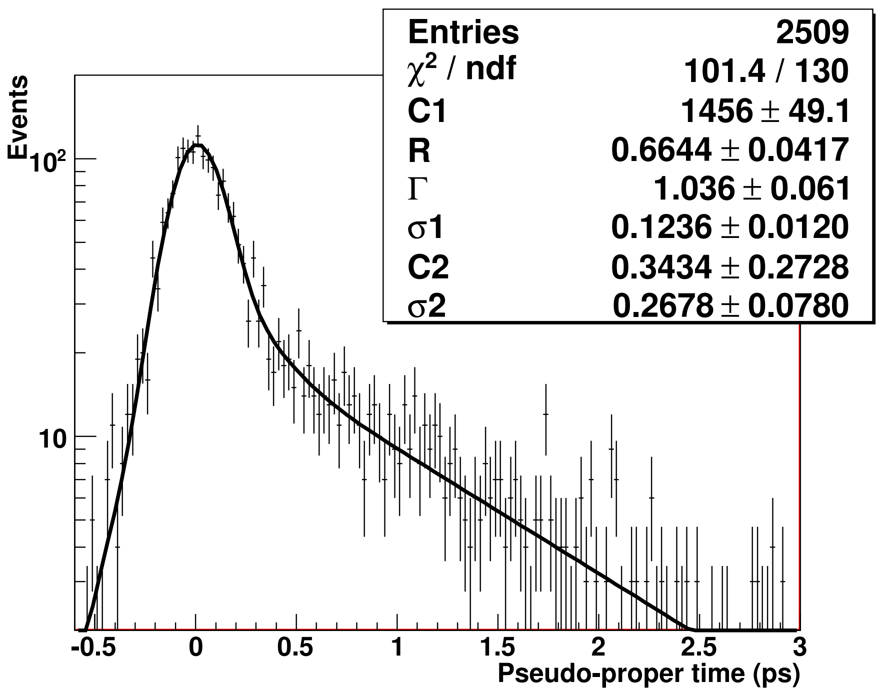

Figure 8.16: *Pseudo-proper time distribution for events with little brem, fitted with function (**??**) and resolution function (**??**). Both truth electrons retain more than 80 % of their initial energy. The default GXF fitter was used to reconstruct the events.*

If the events are separated into cowboy and sailor kinematics, the resolution function needs to

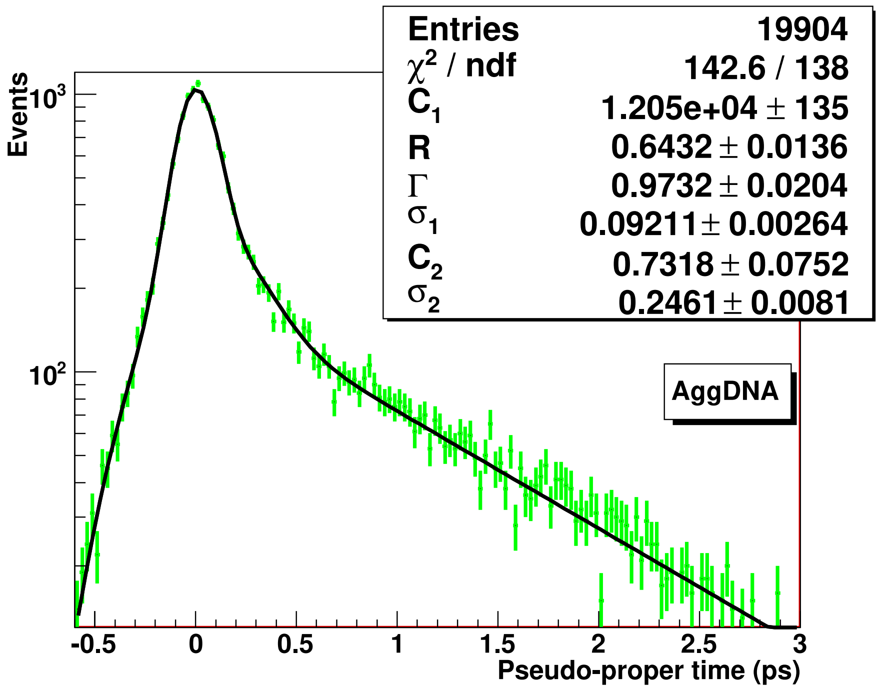

Figure 8.17: *Pseudo-proper time distribution for all events in the barrel, fitted with function (**??**) and resolution function (**??**). Aggressive DNA fitter used. The resolution function used is a normalised sum of two Gaussians, with resolutions σ_1 and σ_2. The second Gaussian, defined as the broader of the two, is weighted by a factor C_2. The value of the normalisation coefficient, C_1, is the estimated integral of the prompt contribution. Γ is the slope of the exponential and $\mathscr{R}$ the ratio of indirect to prompt J/ψ.*

be modified further to account for asymmetric Gaussians (left and right hand resolutions σ_L and σ_R) and peak position shift from zero, m.

The resolution function for a single asymmetric Gaussian with peak position shift is

$$\begin{aligned} r(t) &= \frac{2}{\sqrt{2\pi}\,(\sigma_L+\sigma_R)} \cdot \exp\left(\frac{-\,(t-m)^2}{2\sigma^2}\right) \qquad (8.11)\\ \sigma=\sigma_L &\quad \text{if} \quad t<m \\ \sigma=\sigma_R &\quad \text{if} \quad t>m \end{aligned}$$

The resulting function with two asymmetric Gaussians has ten parameters:$\sigma_{L1}, \sigma_{R1}, m_1, \sigma_{L2}, \sigma_{R2}$, m_2, C_1, C_2, Γ, R. Separate fits for sailor and cowboy pseudo-proper time distributions, with events reconstructed using GXF, are shown in Figure **??** a) and b). The pseudo-proper time distributions shown in Figure **??** c) and d) are reconstructed using Aggressive DNA.

A noticeable feature when comparing these distributions by eye is that the left-hand tail for GXF cowboys is much reduced by the Aggressive DNA fitter, in Figure **??** b) and d). Also, the GXF sailor distribution in Figure **??** a) does not fit a reasonable exponential to the tail, and returns far too large a value for Γ. Likewise the value of the ratio is way too high indicating that the whole model breaks down. Separate fits to these distributions are therefore unsatisfactory and should be improved by a simultaneous fit of both cowboys and sailors.

A simultaneous fit of cowboy and sailor pseudo-proper time distributions permits six parameters to be cross-fed, such that both asymmetric Gaussian contributions are treated as equal but reflected due to the kinematics. The left hand cowboy resolutions are set to be equal to the right hand sailor resolutions ($\sigma_{L1} = \sigma_{L1S} = \sigma_{R1C}$ and $\sigma_{L2} = \sigma_{L2S} = \sigma_{R2C}$) and vice-versa ($\sigma_{R1} = \sigma_{R1S} = \sigma_{L1C}$ and $\sigma_{R2} = \sigma_{R2S} = \sigma_{L2C}$). The peak positions of the asymmetric Gaussians are also treated as equal but opposite with $m_1 = m_{1S} = -m_{1C}$ and $m_2 = m_{2S} = -m_{2C}$.

The sailor and cowboy fits both share the same parameter for the slope of the exponential Γ and

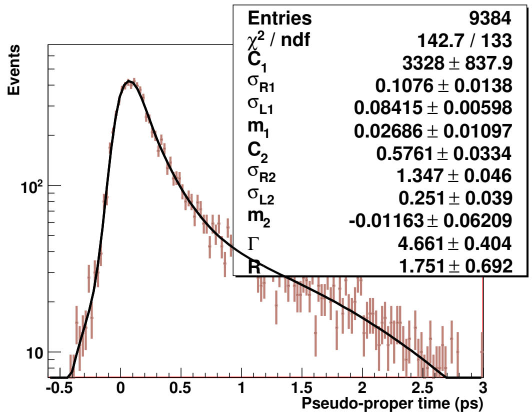

(a) Sailors reconstructed with GXF

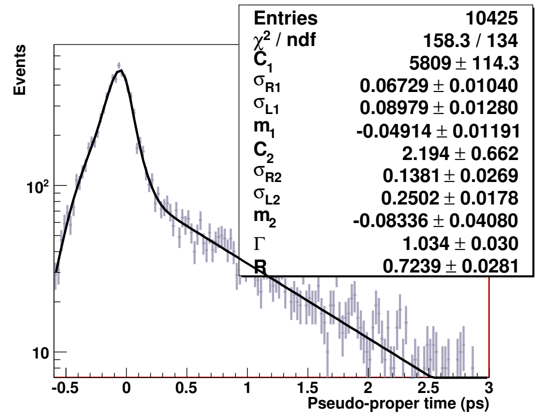

(b) Cowboys reconstructed with GXF

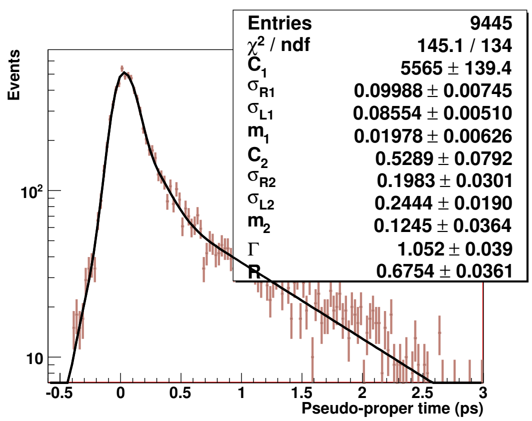

(c) Sailors reconstructed with Aggressive DNA

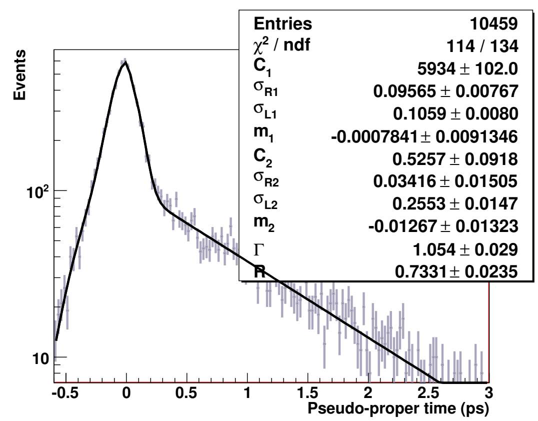

(d) Cowboys reconstructed with Aggressive DNA

Figure 8.18: *Pseudo-proper time distributions for cowboys and sailors fitted separately. GXF and Aggressive DNA fitters were used to reconstruct the events. The resolution function used is the sum of two asymmetric Gaussians, with resolutions σ_{R1}, σ_{L1} and σ_{R2}, σ_{L2} and peak position shifts m_1 and m_2. The second Gaussian, defined as the broader of the two, is weighted by a factor C_2. The value of the normalisation coefficient, C_1, is the estimated integral of the prompt contribution. Γ is the slope of the exponential and $\mathscr{R}$ the ratio of indirect to prompt J/ψ.*

the weight of the second Gaussian term C_2. The overall normalisation coefficients are kept separate for cowboys and sailors, C_{1S} and C_{1C}, since the number of events is different for each kinematic situation. Likewise the ratios of indirect to prompt J/ψ, R_S and R_C are kept separate. The resulting simultaneous fit function thus has 12 parameters.

Pseudo-proper time distributions for cowboys and sailors fitted simultaneously, with resulting fit parameters, are shown in Figure **??** for events reconstructed with GXF and in Figure **??** for events reconstructed with DNA. The resolutions are improved when using AggDNA.

The value of the overall normalisation coefficient, C_1, estimates the number of prompt J/ψ candidates. The results from all fits are shown in Table **??** along with input values. The input values stated are slightly different for the two fitters, since the Aggressive DNA reconstructs slightly more high-quality electron candidates compared with the default non-bremsstrahlung-aware track fitter. The value obtained from the fit is an underestimate in all cases, however using Aggressive DNA as the track fitter results in a closer estimate to the input value.

The ratio $\mathscr{R} = d\sigma(bb \to J/\psi)/d\sigma(pp \to J/\psi)$ extracted from all the fits is shown in Table **??** along with input values. The improvements due to AggDNA fitter are clearly noticeable in the case of sailors. Figure **??** is a much more consistent picture than Figure **??**, with sailors and cowboys displaying closer peaks and a matching exponential tail.

	All	Cowboys	Sailors
GXF	11910 ± 147	6042 ± 95	5574 ± 96
GXF input	12380 ± 111	6414 ± 80	5966 ± 77
AggDNA	12050 ± 135	6184 ± 93	5734 ± 92
AggDNA input	12416 ± 111	6437 ± 80	5979 ± 77

Table 8.4: *Normalisation coefficient, C_1, estimates the number of prompt J/ψ. Results are shown from fitting all J/ψ candidates with GXF (Figure **??**) and Aggressive DNA (Figure **??**) and then simultaneously fitting cowboy and sailor J/ψ candidates with GXF (Figure **??**) and Aggressive DNA (Figure **??**), in comparison with input values.*

The correlation coefficients of the AggDNA fit are shown in Table **??**. The greatest correlations

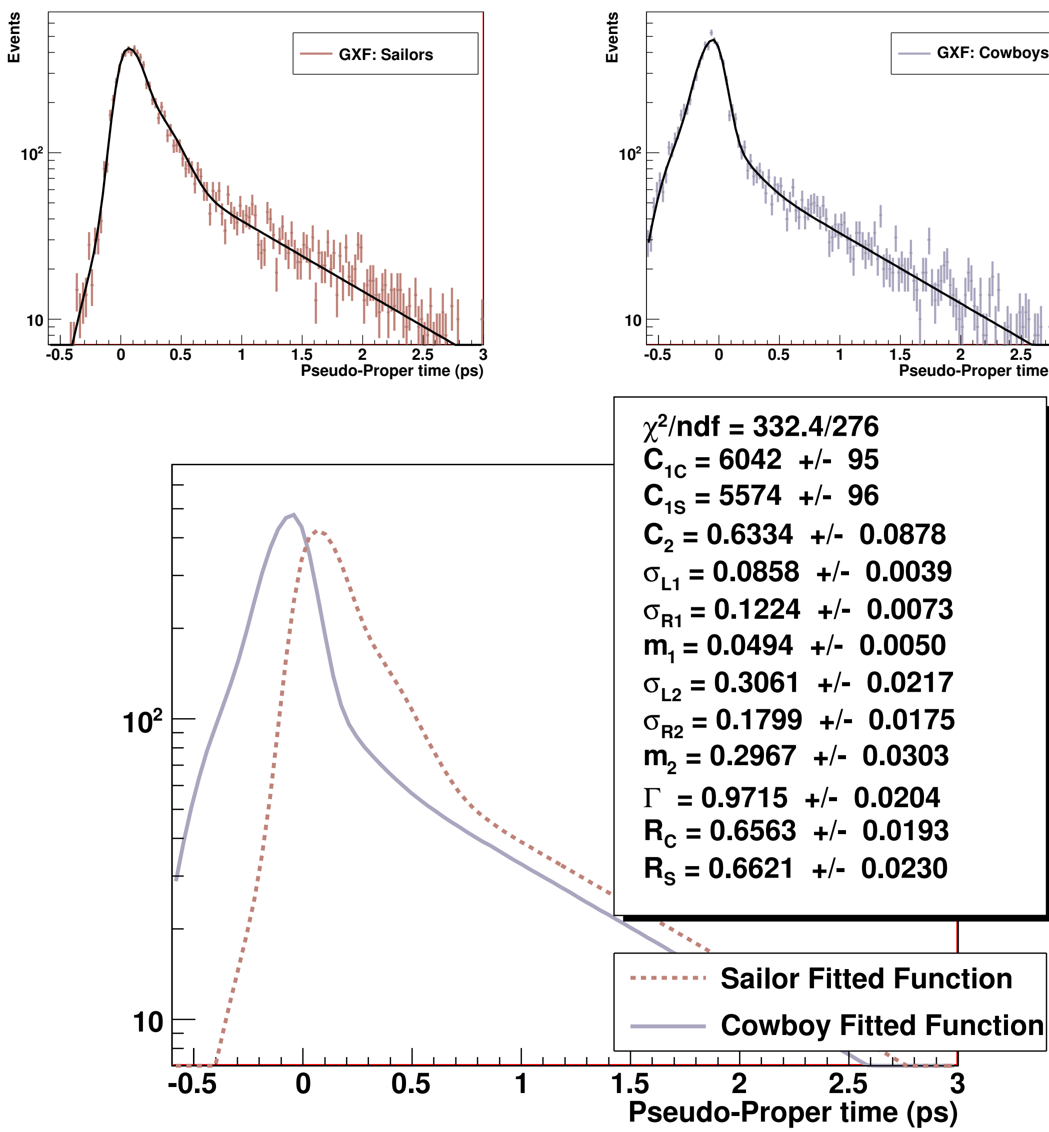

Figure 8.19: *Pseudo-proper time distributions for cowboys (solid line) and sailors (dotted line) fitted simultaneously. GXF fitter was used to reconstruct the events. The fit function represents the sum of a delta-function and an exponential, smeared with two normalised asymmetric Gaussians. The ratio of indirect to prompt J/ψ for cowboy and sailor kinematics are given by $\mathscr{R}_C$ and $\mathscr{R}_S$. The overall normalisation coefficients for cowboys and sailors are C_{1C} and C_{1S}. The slope of the exponential is Γ. The two asymmetric Gaussians have resolution and peak shift from zero, which I have defined as positive for sailors and negative for cowboys, such that $\sigma_{L1} = \sigma_{L1S} = -\sigma_{R1C}$, $\sigma_{R1} = \sigma_{R1S} = -\sigma_{L1C}$, $m_1 = m_{1S} = -m_{1C}$ and $\sigma_{L2} = \sigma_{L2S} = -\sigma_{R2C}$, $\sigma_{R2} = \sigma_{R2S} = -\sigma_{L2C}$, $m_2 = m_{2S} = -m_{2C}$. The weight of the second Gaussian term is given by C_2.*

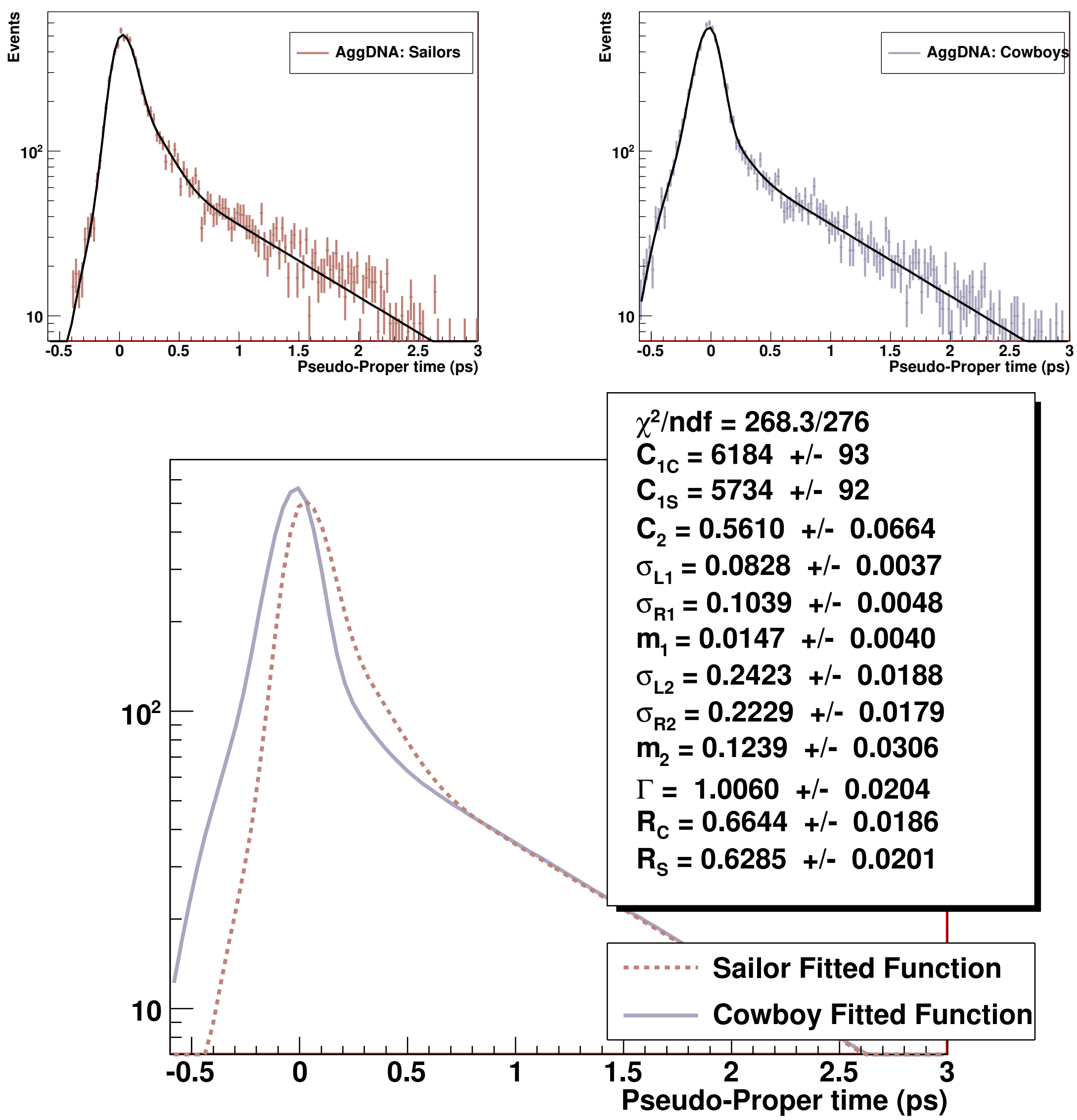

Figure 8.20: *Pseudo-proper time distributions for cowboys (solid line) and sailors (dotted line) fitted simultaneously. Aggressive DNA fitter was used to reconstruct the events. The fit function represents the sum of a delta-function and an exponential, smeared with two normalised asymmetric Gaussians. The ratio of indirect to prompt* J/ψ *for cowboy and sailor kinematics are given by* $\mathscr{R}_C$ *and* $\mathscr{R}_S$*. The overall normalisation coefficients for cowboys and sailors are* C_{1C} *and* C_{1S}*. The slope of the exponential is* Γ*. The two asymmetric Gaussians have resolution and peak shift from zero, which I have defined as positive for sailors and negative for cowboys, such that* $\sigma_{L1} = \sigma_{L1S} = -\sigma_{R1C}$, $\sigma_{R1} = \sigma_{R1S} = -\sigma_{L1C}$, $m_1 = m_{1S} = -m_{1C}$ *and* $\sigma_{L2} = \sigma_{L2S} = -\sigma_{R2C}$, $\sigma_{R2} = \sigma_{R2S} = -\sigma_{L2C}$, $m_2 = m_{2S} = -m_{2C}$*. The weight of the second Gaussian term is given by* C_2*.*

	All	Cowboys	Sailors
GXF	0.640 ± 0.015	0.656 ± 0.019	0.662 ± 0.023
GXF Input	0.600 ± 0.009	0.625 ±0.013	0.573 ±0.012
AggDNA	0.643 ± 0.014	0.664 ± 0.019	0.629 ± 0.020
AggDNA Input	0.603 ± 0.009	0.625 ± 0.013	0.580 ± 0.012

Table 8.5: *Ratio of indirect to prompt J/ψ, $\mathscr{R}$. Results are shown from fitting all J/ψ candidates with GXF (Figure* **??***) and Aggressive DNA (Figure* **??***) and then simultaneously fitting cowboy and sailor J/ψ candidates with GXF (Figure* **??***) and Aggressive DNA (Figure* **??***), in comparison with input values.*

are between the peak position shift of the wider Gaussian, m_2, and its resolutions σ_{L2} and σ_{R2}. This is not surprising or worrying, since there is clearly a lot of flexibility in that Gaussian definition.

Par	C_{1C}	σ_{L1}	σ_{R1}	m_1	C_2	σ_{L2}	σ_{R2}	m_2	C_{1S}	Γ	$\mathscr{R}_C$	$\mathscr{R}_S$	Global
C_{1C}	1.000	-0.007	0.015	-0.037	0.048	-0.005	0.053	-0.062	0.018	-0.220	-0.738	-0.001	0.7430
σ_{L1}	-0.007	1.000	-0.399	0.792	-0.507	0.568	-0.404	0.606	-0.007	0.004	-0.008	0.021	0.9248
σ_{R1}	0.015	-0.399	1.000	-0.697	-0.371	-0.080	0.531	-0.308	0.073	-0.016	0.010	-0.094	0.9239
m_1	-0.037	0.792	-0.697	1.000	-0.107	0.253	-0.297	0.333	0.003	0.011	0.030	0.004	0.9350
C_2	0.048	-0.507	-0.371	-0.107	1.000	-0.718	0.093	-0.542	0.008	-0.074	-0.061	-0.019	0.9323
σ_{L2}	-0.005	0.568	-0.080	0.253	-0.718	1.000	-0.630	0.921	-0.015	0.024	-0.016	0.035	0.9687
σ_{R2}	0.053	-0.404	0.531	-0.297	0.093	-0.630	1.000	-0.836	0.101	-0.037	-0.018	-0.137	0.9527
m_2	-0.062	0.606	-0.308	0.333	-0.542	0.921	-0.836	1.000	-0.020	0.036	0.050	0.034	0.9868
C_{1S}	0.018	-0.007	0.073	0.003	0.008	-0.015	0.101	-0.020	1.000	-0.224	0.009	-0.746	0.7495
Γ	-0.220	0.004	-0.016	0.011	-0.074	0.024	-0.037	0.036	-0.224	1.000	0.193	0.202	0.3408
$\mathscr{R}_C$	-0.738	-0.008	0.010	0.030	-0.061	-0.016	-0.018	0.050	0.009	0.193	1.000	-0.033	0.7575
$\mathscr{R}_S$	-0.001	0.021	-0.094	0.004	-0.019	0.035	-0.137	0.034	-0.746	0.202	-0.033	1.000	0.7692

Table 8.6: *Parameter Correlation Coefficients for 12 parameter fit. The fit function represents the sum of a delta-function and an exponential, smeared with two normalised asymmetric Gaussians. The ratio of indirect to prompt J/ψ for cowboy and sailor kinematics are given by $\mathscr{R}_C$ and $\mathscr{R}_S$. The overall normalisation coefficients for cowboys and sailors are C_{1C} and C_{1S}. The slope of the exponential is Γ. The two asymmetric Gaussians have resolution and peak shift from zero, which I have defined as positive for sailors and negative for cowboys, such that $\sigma_{L1} = \sigma_{L1S} = -\sigma_{R1C}$, $\sigma_{R1} = \sigma_{R1S} = -\sigma_{L1C}$, $m_1 = m_{1S} = -m_{1C}$ and $\sigma_{L2} = \sigma_{L2S} = -\sigma_{R2C}$, $\sigma_{R2} = \sigma_{R2S} = -\sigma_{L2C}$, $m_2 = m_{2S} = -m_{2C}$. The weight of the second Gaussian term is given by C_2.*

8.8 Systematic Errors

The various sources of possible systematic uncertainties have not been studied since this is a feasibility study and not a full analysis. However the key systematics are expected to come from the background.

8.8.1 Background subtraction

The signal:background in the barrel is expected to be $\sim$ 20:1 and in the endcaps only $\sim$ 2:1. Simpson's rule could be used to estimate the background contribution, which combines the trapeze rule and the midpoint rule. Or a sideband method used, which estimates the background from the region either side of the signal.

8.8.2 η range variation

If this analysis is carried out in the barrel region ($|\eta| < 1$). The η range could then be divided into $|\eta| < 0.5$ and $|\eta| > 0.5$ The difference in the result of the two η ranges noted and seen whether it is consistent with statistical errors. Or the range could be divided into $|\eta| < 0.9$ and $|\eta| > 1.0$ and again noted if the difference in result is consistent with statistical errors.

8.9 Summary

L_{xy} is the distance of the secondary vertex from the primary vertex in the transverse plane projected onto the J/ψ momentum direction. As described above, electron tracks having positive difference in ϕ between the positive and negative electron, are known as sailors and have a tendency of increasing reconstructed L_{xy} due to bremsstrahlung. Electron tracks having negative difference in ϕ between the positive and negative electron, are known as cowboys and have a tendency of decreasing reconstructed L_{xy}.

When cowboy and sailor L_{xy} distributions for prompt J/ψ are plotted separately, the distributions are almost mirror images; cowboys have a tail towards negative L_{xy} with a negative peak shift from zero, and sailors show the same effects but in the opposite direction. This effect is due to bremsstrahlung. The bremsstrahlung-aware fitter, Aggressive DNA, reduces this effect and improves the resolutions but visible differences between cowboys and sailors still remain.

Various analyses require samples of pure prompt or pure indirect J/ψ mesons. By making a cut on the pseudo-proper time of the J/ψ, one can separate most of the prompt J/ψ from the indirect J/ψ sample (or vice-versa). By selecting cowboys, a significant improvement in the purity of extracting indirect J/ψ can be achieved. This could be useful for future B-Physics studies.

Measurement of the ratio $d\sigma(bb \rightarrow J/\psi)/d\sigma(pp \rightarrow J/\psi)$ in the electron decay channel is shown to be possible using a resolution function with two Gaussians. Once events are divided into cowboys and sailors, the fitting function needs to be modified to take into account the asymmetry of the Gaussians and their peak shift from zero. This results in some improvement in determination of the ratio and an important improvement in understanding some electron-specific systematic effects.

An ATLAS Communication on this study is in preparation.

'The important thing is not to stop questioning.'

Albert Einstein

9

Conclusions and outlook

This thesis is essentially a collection of tools and methods related to the electron track reconstruction in ATLAS. The Dynamic Noise Adjustment (DNA) track fitter algorithm employs a method based on the underlying physical process. It can be used either on initial track reconstruction or for re-reconstruction of already identified electrons. In Chapter **??** I showed the improvement in electron reconstruction that can be expected when using this bremsstrahlung-aware track fitter.

Before any precision physics studies can begin, the various sub-detectors of ATLAS must be well-aligned, and the presence of distortions or any additional material must be identified and understood. I have shown in Chapter **??** that it should be possible to use the DNA track fitter as a tool for mapping the Inner Detector material and gaining an understanding of the distribution of the material budget. DNA finds points on a trajectory where the momentum is changing. Whether this is electron bremsstrahlung or pion scattering, it occurs due to the presence of material. So the more material there is, the more DNA activity will be seen. DNA hits can therefore be used as an indicator of the presence of material. Modulation in the SCT material was observed through DNA hits, which agreed well with the true modulation seen through geantino scans. With huge statistics soon available with data and a priori symmetries of the detector, this tool could be made quite successful.

In Chapter **??** I have shown that purity and efficiency of separating indirect J/ψ from prompt ones can be improved by separate consideration of the two kinematical configurations, cowboys and sailors. This could be useful for future B-Physics studies.

I have also shown in Chapter **??** that the measurement of the ratio $d\sigma(bb \rightarrow J/\psi)/d\sigma(pp \rightarrow J/\psi)$ is possible using a resolution function with two Gaussians. Once events are divided into cowboys and sailors, the fitting function needs to be modified to take into account the asymmetry of the Gaussians and their peak shift from zero. This results in some improvement in determination of the ratio and an important improvement in understanding some electron-specific systematic effects. During the future 'initial' run of the LHC with the luminosity of 10^{31} cm^{-2} s^{-1}, one day of running roughly corresponds to the integrated luminosity of 1 pb^{-1}. With the EF_MU4_Je5e3_FS trigger and this integrated luminosity, one would then expect about 100 $J/\psi \rightarrow ee$ recorded events. During future high luminosity running, the need to keep event rates manageable will cause the increase of thresholds of relevant muon triggers, and the prescaling of lower threshold triggers.

At the end of 2009, ATLAS enjoyed a series of stable LHC runs at a centre-of-mass energy of 900 GeV, successfully recording and analysing the many collisions which took place. A significant number of low p_T electron and photon candidates were reconstructed in these events, the majority being ascribed to photons from π^0 decays, electrons from photon conversions, and hadrons faking electrons or photons. Whilst the transverse energies of the candidates observed in these data are well below those for which the reconstruction and identification algorithms have been optimised, the measurements provide a quantitative test of both the algorithms themselves and the reliability of the performance predictions in the transverse energy range from the reconstruction threshold of 2.5 GeV to almost 10 GeV. The collision events analysed by ATLAS correspond to a total integrated luminosity of approximately 9 μb^{-1}, with a yield of 879 electron candidates reconstructed with transverse energy $>$2.5 GeV before identification cuts.

References

[1] ATLAS Event Displays.
http://atlas.web.cern.ch/Atlas/public/EVTDISPLAY/events.html

[2] C. Amsler *et al.* [Particle Data Group], Phys. Lett. B **667** (2008) 1.

[3] D. Griffiths. *'Introduction to Elementary Particles'* ISBN 3-527-40601-8

[4] S.L. Glashow: Nucl. Phys. 22 (1961) 279.
A. Salam: Phys. Rev. 127 (1962) 331.
S. Weinberg: Phys. Rev. Lett. 19 (1967) 1264.

[5] N. Cabibbo (1963). 'Unitary Symmetry and Leptonic Decays.' Phys. Rev. 10 (12): 531533.
M. Kobayashi, T. Maskawa (1973). 'CP-Violation in the Renormalizable Theory of Weak Interaction'. Progress of Theoretical Physics 49 (2): 652657.

[6] http://nobelprize.org/nobel_prizes/physics/laureates/2008/

[7] C. S. Wu; E. Ambler, R. W. Hayward, D. D. Hoppes, R. P. Hudson. 'Experimental Test of Parity Conservation in Beta Decay' Phys. Rev. 105, 14131415 (1957).

[8] 'Invariante Variations probleme', Nachr. v. d. Ges. d. Wiss. zu Gttingen, Math-phys. Klasse, 235257 (1918). English translation, M. A. Tavel, 'Invariant variation problem', Transport Theory Stat. Mech.1 (3), 183207 (1971).

[9] J. J. Aubert *et al.* [E598 Collaboration], Phys. Rev. Lett. **33** (1974) 1404.

[10] J. E. Augustin *et al.* [SLAC-SP-017 Collaboration], Phys. Rev. Lett. **33** (1974) 1406.

[11] S. Okubo, Phys. Lett. **5**, 165 (1963); G. Zweig, CERN Reports TH 401 and TH412 (1964); J. Iizuka, Progr. Ther. Phys. Suppl. **37**, 21 (1966).

[12] ATLAS photos.
`http://atlas.ch/photos/lhc.html`

[13] ATLAS Collaboration, G. Aad et al., *'The ATLAS Experiment at the CERN Large Hadron Collider,'* JINST **3** (2008) S08003.

[14] ATLAS Collaboration, *'ATLAS inner detector: Technical design report, Vol. I,'* CERN-LHCC-97-016, ATLAS-TDR-004, (1997).

[15] A. Abdesselam, T. Akimoto et al., *'The Barrel Modules of the ATLAS SemiConductor Tracker'*. ATL-COM-INDET-2006-009.

[16] S. Mehlhase, T.C. Petersen. *'A probability based approach to PID in the TRT detector of ATLAS'* ATL-COM-INDET-2006-017

[17] ATLAS Collaboration, *'ATLAS: Detector and physics performance technical design report, Vol. I,'* CERN-LHCC-99-014, ATLAS-TDR-14, (1999).

[18] ATLAS Collaboration, G. Duckeck et al., *'ATLAS computing: Technical design report,'* CERN-LHCC-2005-022 (2005).

[19] *ATLAS Metadata Interface*
`http://ami.in2p3.fr/opencms/opencms/AMI/www/`

[20] T. Sjostrand, S. Mrenna and P. Skands, 'PYTHIA *6.4: Physics and manual',* JHEP **0605** (2006) 026 [arXiv:hep-ph/0603175].

[21] M. Smizanska, *'PythiaB: An interface to Pythia6 dedicated to simulation of beauty events,'* [ATL-COM-PHYS-2003-038] (2003).

[22] ‘PYTHIA *update notes,* http://www.hepforge.org/archive/pythia6/update_notes-6.4.23.txt, retrieved July 2010.

[23] J. Pumplin, D. R. Stump, J. Huston, H. L. Lai, P. M. Nadolsky and W. K. Tung, *‘New generation of parton distributions with uncertainties from global QCD analysis’,* JHEP **0207** (2002) 012 [arXiv:hep-ph/0201195].

[24] ATLAS Collaboration *‘ATLAS MOnte Carlo Tunes for MC09’* ATL-PHYS-PUB-2010-002

[25] GEANT4 Collaboration, S. Agostinelli et al. *‘GEANT4: A simulation toolkit,’* Nucl. Instrum. Meth. A **506** (2003) 250. http://geant4.web.cern.ch/geant4/

[26] Gaudi/Athena and Grid Alliance (Ganga), http://cern.ch/ganga/ retrieved September 2008.

[27] *‘The Panda Production And Distributed Analysis System (Panda)’* https://twiki.cern.ch/twiki/bin/view/Atlas/Panda

[28] *‘Reconstruction and Identification of Electrons’* ATL-PHYS-PUB-2009-004

[29] *‘Expected Performance of the ATLAS Experiment – Detector, Trigger and Physics,’* CERN-OPEN-2008-020, Geneva (2008).

[30] *‘Electron and photon reconstruction and identification in ATLAS: expected performance at high energy and results at 900 GeV.’* ATLAS-CONF-2010-005

[31] http://en.wikipedia.org

[32] D.H.Perkins. *‘Introduction to High Energy Physics’* Addison-Wesley 2000.

[33] https://twiki.cern.ch/twiki/bin/view/Atlas/PixelPublicResults

[34] M. Marucho, H. Fanchiotti and C. Garcia Canal. *'The Landau Distribution'*, Int. J. Mod. Phys. C17(2006) 1461.

[35] *'The ATLAS Track Extrapolation Package'* A. Salzburger. ATL-SOFT-PUB-2007-005

[36] W.R. Leo, *'Techniques for Nuclear and Particle Physics Experiments',* ISBN-0-387-57280-5.

[37] H. Bethe and W. Heitler, *'On the Stopping of fast particles and on the creation of positive electrons,'* Proc. Roy. Soc. Lond. A **146** (1934) 83.

[38] V. Kartvelishvili [ATLAS Collaboration], *'Electron Bremsstrahlung Recovery In Atlas,'* Nucl. Phys. Proc. Suppl. **172**, 208 (2007).

[39] ATLAS Detector Paper Back-up Note: *Electrons and Photons* ATL-COM-INDET-2008-010.

[40] *'Reconstruction of Photon Conversions'* ATL-PHYS-PUB-2009-006 ; ATL-COM-PHYS-2009-172

[41] *'Calibration and Performance of the Electromagnetic Calorimeter'* ATL-PHYS-PUB-2009-003 ; ATL-COM-PHYS-2009-169

[42] `http://atlas-computing.web.cern.ch/atlas-computing/links/nightlyDevDirectory/AtlasOffli latest_doxygen/InstallArea/doc//TrkParameters/html//classTrk_1_1Perigee.html`

[43] A. Salzberger et al., *'The new ATLAS Track Reconstruction (NEWT)'*, ATLAS public note, ATL-SOFT-PUB-2007-007, 2007.

[44] ATLAS Collaboration, Thijs Cornelissen. *'CTBT Tracking: track reconstruction for the test-beam and cosmics.'*, ATLAS Internal Note ATL-INDET-INT-2006-001.

[45] T.G. Cornelissen et al., *'The global χ^2 track fitter in ATLAS'*, Journal of Physics: Conference Series 119 (2008) 032013.

[46] R. Fruhwirth, *'Application of Kalman Filtering to Track and Vertex Fitting'*, Nucl. Instr. Meth. A262(1987) 444.

[47] https://twiki.cern.ch/twiki/bin/view/Atlas/TrkKalmanFitter

[48] R. Fruhwirth, *'Gaussian-mixture approximation of the Bethe-Heitler model of electron energy loss by bremsstrahlung,'* Comput. Phys. Commun. **154** (2003) 131.

[49] *'Distorted Material in CSC Simulation'* https://twiki.cern.ch/twiki/bin/view/Atlas/DistortedMater

[50] *'Simulation Options' in the Geant4 Simulation Atlas Applications User Manual (Dec. 2006)* http://atlas-computing.web.cern.ch/atlas-computing/packages/simulation/geant4.

[51] *'The SCT Material Budget'*. ATL-COM-INDET-2008-020.

[52] http://root.cern.ch/drupal/content/architectural-overview

[53] ATLAS Collaboration, G Aad et al *'Heavy quarkonium physics with early ATLAS data,'* [ATL-PHYS-INT-2008-017] and in *'Expected Performance of the ATLAS Experiment – Detector, Trigger and Physics,'* CERN-OPEN-2008-020, Geneva (2008).

[54] ATLAS Virtual Point 1 (vp1) Event Display, http://atlas-vp1.web.cern.ch/atlas-vp1

[55] D. Price *'Studies of quarkonium production and polarisation with early data at ATLAS'* CERN-THESIS-2008-098

[56] *'Measurement of the ratio $d\sigma(bb \to J/\psi)/d\sigma(pp \to J/\psi)$ with early ATLAS data'* ATL-COM-PHYS-2009-664